Charge density wave ground state in the intercalated graphite CaC6

Grozić, Petra

University of Zagreb
Faculty of Science
Department of Physics

Petra Grozić

Charge density wave ground state in the intercalated graphite CaC_6

DOCTORAL THESIS

Zagreb, 2024

University of Zagreb
Faculty of Science
Department of Physics

Petra Grozić

Charge density wave ground state in the intercalated graphite CaC_6

DOCTORAL THESIS

Supervisor:
Prof. Dr. Sc. Danko Radić

Zagreb, 2024

Sveučilište u Zagrebu
Prirodoslovno-matematički fakultet
Fizički odsjek

Petra Grozić

Osnovno stanje vala gustoće naboja u interkaliranom grafitu CaC_6

DOKTORSKI RAD

Mentor:
prof. dr. sc. Danko Radić

Zagreb, 2024

Acknowledgements

After finishing this dissertation, I believe that every physicist exists in a state of superposition between passionately loving and passionately hating physics, and apparently, this is how it has to be. I would like to thank all the people that surrounded me on this mad journey of pursuing a PhD in theoretical physics, even though most of you couldn't see the appeal in this field. I could never have done it if it weren't for your support.

Firstly, I would like to thank my supervisor, Prof. Radić, for his endless patience with me as his student. I came to realise that the PhD experience one has depends more on your mentor than the field of science you pursue, and I was immensely lucky to have you guide me and teach me. I would also like to thank Dr. Anatoly Kadigrobov for his never ending patience with my silly questions and for telling me to stop a bit less often than he does with Prof. Radić. Finally, I need to thank Assistant Professor Rukelj. Thank you for being a friend.

This thesis would never have been finished if it weren't for all my colleagues at the Department of Physics who supported me both professionally and as friends. I also need to thank all the people at the weightlifting club "DK Metalac" for their friendship and for providing me with a safe haven to go to when I needed to run away from physics.

Finally, I need to thank my family and my future husband for always believing in me, even though I never really believed in myself that much. You encouraged me to go on and persist in this crazy path of mine.

Aida, Romano, Bojan, Melita, Clelia, Đano, Mira, Marina, Brle, Mateo V., Jurjue, Sara, Marina, Petra, Mateo S., Miha, Zoran, Barbara, Mateo T., DK Metalac

"You're entirely bonkers. But I'll tell you a secret: All the best people are."

-Lewis Carroll, *Alice in Wonderland*

Abstract

The physics of graphite intercalated compounds (GIC), in spite of the fact that these materials were synthesised quite long ago, is still the focus of modern theoretical and experimental research. The interest of the scientific community is focused on GIC, mostly due to the possibility of forming unusual superconducting (SC) and charge density wave (CDW) ground states. We focus on one of these materials, CaC_6, in which experiments clearly demonstrate the existence of CDWs. The very existence of the CDW is quite unusual due to the fact that the graphene Fermi surface, chemically doped by calcium intercalates, shows no so-called "nesting property," i.e., no Peierls mechanism, which has been the paradigmatic mechanism behind the CDW instability since the 1950s and was experimentally realised during the 1980s in highly anisotropic materials with open Fermi surfaces. We show that the CaC_6 Fermi surface undergoes a different CDW stabilisation mechanism based on the topological reconstruction (of the Fermi Surface) and critical strength of the electron-phonon interaction. Such topological reconstruction, which transforms the set of closed Fermi pockets into open Fermi sheets, has profound effects on transport and magnetotransport properties. In this thesis, we show how the Fermi surface reconstruction stabilises the CDW ground state. Furthermore, we present the magnetotransport properties, taking into account magnetic breakdown.

Keywords:
Charge density wave (CDW), Fermi surface reconstruction, intercalated graphite, magnetoconductivity, magnetic breakdown

Prošireni sažetak

Ključne riječi:
Val gustoće naboja, topološka rekonstrukcija Fermijeve površine, interkalirani grafit, magnetovodljivost, magnetski proboj

Uvod

Valovi gustoće naboja statička su modulacija elektronske gustoće koja uobičajeno dolazi u paru s periodičkom distorzijom kristalne rešetke materijala. U ovom poglavlju daje se povijesni pregled od prvih spomena valova gustoće naboja davnih pedesetih godina prošlog stoljeća, njihovog opisa pomoću Peierlsove nestabilnosti, pa do početnih eksperimentalnih otkrića. Dan je bitan uvid u to kako je objašnjavanje pojave vala gustoće naboja strogo vezana uz pojam *gniježđenja Fermijeve površine* do te razine da je takvo objašnjenje postalo praktički paradigma.

Interkalirani grafiti - materijali razmatrani u ovom radu

Grafen je materijal koji već godinama fascinira znanstvenu zajednicu. Prvi put je sintetiziran i karakteriziran 2004. godine, što je rezultiralo Nobelovom nagradom iz fizike 2010. Taj dvodimenzionalni materijal pokazuje fascinantne karakteristike i on je temelj za materijal kojime se ovaj rad bavi. U prvom dijelu ovog poglavlja opisana su mu sinteza, svojstva i struktura.

Ugljik poprima mnoštvo alotropskih modifikacija, a interkalirani grafit CaC_6 sazdan je od dvodimenzionalnih slojeva grafena između kojih su smješteni kalcijevi atomi. U drugom dijelu poglavlja daje se uvid u sintezu interkaliranog grafita CaC_6, te njegova svojstva i strukturu.

Motivacija za ovaj rad

U ovom poglavlju prolazimo kroz opažanja iz dva eksperimentalna rada koji opisuju pojavu valova gustoće naboja u interkaliranom grafitu CaC_6, te u dvoslojnom spoju C_6CaC_6, popraćenu

pojavom pseudo-procijepa u elektronskom spektru . Radovi predstavljeni u ovom poglavlju:

- K.C. Rahnejat, C.A. Howard, N.E. Shuttleworth, S.R. Schofield, K. Iwaya, C.F. Hirjibehedin, Ch. Renner, G. Aeppli & M. Ellerby, Charge density waves in the graphene sheets of the superconductor CaC_6. *Nat. Communication* **2**, 558 (2011).
- R. Shimizu, K. Sugawara, K. Kanetani, K. Iwaya, T. Sato, T. Takahashi & T. Hitosugi, Charge-density wave in Ca-intercalated bilayer graphene induced by commensurate lattice matching. *Phys. Rev. Lett.* **114** 146103 (2015).

Naša glavna motivacija proizlazi iz činjenice da interkalirani grafit ne posjeduje Fermijevu površinu s mogućnosti gniježđenja, stoga, moramo pronaći novo teorijsko objašnjenje za eksperimentalno opažene pojave.

Minimalni model

Cilj ovog rada je opisati i objasniti pojavu nastanka valova gustoće naboja u interkaliranom grafitu CaC_6 tzv. minimalnim modelom, koji sadrži samo fizikalne odlike nužne za samu egzistenciju pojave vala gustoće naboja.

Inicijalni problem sustava vezanih elektrona i fonona opisujemo dvodimenzionalnim Fröhlichovim hamiltonijanom. Njega tretiramo u aproksimaciji srednjeg polja i uvodimo kompleksni parametar uređenja. Nakon tretmana aproksimacijom srednjeg polja dobivamo izraz za elektronske vrpce.

Kako bismo dobili oblik rekonstruiranih elektronskih vrpci, posežemo za posebno razvijenim metodama razvoja podintegralnih funkcija kako bismo dobili analitički rezultat za kondenzacijsku energiju sustava. Da bi novonastalo stanje s valom gustoće naboja bilo stabilno, kondenzacijska energija mora biti pozitivna, a njezina maksimizacija vrši se optimizacijom izraza po samosuglasnom valnom vektoru vala gustoće i po njegovom parametru uređenja.

Nadalje, određujemo koji je fononski mod kristalne rešetke u CaC_6 strukturi zaslužan za pojavu vala gustoće. Pokazuje se da je to TA mod titranja kalcijeve superrešetke u njezinoj ravnini. Ovaj mod je "najmekši", odnosno ima najmanju energiju, ali i najjače vezan je vezan na grafenske elektrone čime su eliminirani svi grafenski vibracijski modovi, kao i kalcijevi fleksuralni modovi titranja.

Diskusija

Ovaj teorijski rad inspiriran je eksperimentalnim opažanjima. Ovo poglavlje bavi se usporedbom predstavljenih teorijskih rezultata s eksperimentalnim opažanja iz gore navedenih članaka. Predstavljena teorijska objašnjenja pokazuju iznimno dobro slaganje s ključnim eksperimentalno opaženim činjenicama: (1) pojava, period i orijentacija vala gustoće s obzirom na grafensku rešetku; (2) pojava pseudo-procijepa u elektronskom spektru; (3) statička deformacija kalcijeve superrešetke koja odgovara teorijski predviđenom fononskom TA modu.

Magnetovodljivost u uvjetima koherentnog magnetskog proboja

U ovom poglavlju računamo tenzor magnetovodljivosti za interkalirani grafit CaC_6 u kojem se pojavljuje val gustoće naboja, u uvjetima magnetskog proboja. Magnetski proboj je pojava gdje dolazi do tuneliranja između različitih elektronskih vrpci vodljivih elektrona nekog metala.

Dan je opis pojave koherentnog magnetskog proboja, u okviru koje će se računati tenzor magnetovodljivosti. Potom, opisuje se ponašanje elektrona u sustavu Fermijevih površina koje se međusobno malo preklapaju, opisanih u semiklasičnoj aproksimaciji, dok je tretman regija gdje dolazi do magnetskog proboja potpuno kvantnomehanički.

Uvodi se osnovni model sustava CaC_6 u homogenom vanjskom magnetskom polju, okomitom na ravninu uzorka. Za takav sustav nalazimo semiklasične valne funkcije, te elektronski spektar.

Tenzor magnetovodljivosti za dvodimenzionalni sustav izračunat je u okviru formalizma kvantne matrice gustoće. Taj tenzor je anizotropan, te sadrži komponentu duž hrbata vala gustoće naboja koja je okomita na otvorene elektronske trajektorije u recipročnom prostoru, komponentu duž smjera periodičnosti vala gustoće naboja koja je duž otvorenih elektronskih trajektorija u recipročnom prostoru, te Hallove komponente magnetovodljivosti. Komponenta magnetovodljivosti okomita na otvorene trajektorije u recipročnom prostoru, te Hallove komponente ponašaju se kao za klasične sustave u odsustvu magnetskog proboja, dok komponenta duž otvorenih elektronskih trajektorija pokazuje vrlo snažne kvantne oscilacije koje nisu korekcija klasičnoj komponenti, već njezin inherentni dio.

Zaključak

U ovoj tezi predloženo je teorijsko objašnjenje za pojavu vala gustoće naboja u interkaliranom grafitu CaC_6, alternativno paradigmatskom pristupu temeljenom na gniježđenju Fermijeve površine koji u ovom sustavu nije primijenjiv. Predloženi mehanizam temelji se na

topološkoj rekonstrukciji Fermijeve površine elektrona vezanih na TA fononski mod kalcijeve superrešetke. Pojava vala gustoće ostvaruje se kao kvantni fazni prijelaz pri elektron-fonon vezanju jačem od kritičnog.

Magnetovodljivost ovog sustava u uvjetima koherentnog magnetskog proboja karakterizirana je komponentama tenzora: (1) komponenta okomita na otvorene elektronske trajektorije u recipročnom prostoru pokazuje standardnu klasičnu ovisnost proporcionalnu $1/B^2$; (2) Hallove komponente također pokazuju klasičnu ovisnost proporcionalnu $1/B$; (3) komponenta duž otvorenih trajektorija u recipročnom prostoru pokazuje snažne kvantne oscilacije u jakom magnetskom polju B. Ove oscilacije, periodične s $1/B$, inherentne su glavnom doprinosu, a ne tek njegova korekcija, koji se svodi na konstantni klasični rezultat u granici odsustva magnetskog proboja.

Contents

Chapter 1

Introduction

The exploration of charge density waves (CDW) in CaC_6 has been both challenging and rewarding. This thesis delves into the intricate mechanisms underlying the formation of these phenomena, aiming to contribute to the understanding of CDWs in quasi-two-dimensional materials.

The thesis unfolds with an introduction to CDWs, offering a comprehensive overview of their historical development and initial research to provide context for the subsequent chapters. Following this, a detailed exploration of the materials under investigation, graphene and the intercalated graphite CaC_6, sets the stage for the subsequent analysis.

A review of relevant experimental work is then presented, examining studies that inspired and guided the research, providing a foundation for the theoretical and computational aspects discussed in later chapters. The theoretical framework is explained, highlighting the modelling approach adopted and emphasizing the topological reconstruction of the Fermi surface, provided the electron-phonon coupling is larger than critical, as key factors in understanding the emergence of CDWs in CaC_6.

The thesis concludes with a comprehensive examination of the magnetoconductivity tensor under magnetic breakdown conditions, offering insights into the behavior of the system in this specific regime. Through this systematic exploration, the thesis aims to contribute to the specific understanding of CDWs in two-dimensional materials.

1.1 Charge density waves

A charge density wave (CDW) is a static modulation of conduction electrons and is a Fermi surface-driven phenomenon usually accompanied by a periodic distortion of the crystal lattice [1]. It was initially described by Rudolf Peierls in 1955 [2] and by Herbert Fröhlich in 1954 [3].

The significance of highly anisotropic band structures in the emergence of these ground states was acknowledged at an early stage [4]. It is not surprising that experimental evidence for these ground states was discovered at a later time, coinciding with the discovery and examination of materials possessing a highly anisotropic, quasi-one-dimensional linear chained structure and metallic characteristics. Various groups of organic and inorganic materials have become established as typical instances of density wave ground states [4].

1.2 CDWs - a historical overview

It has been over six decades since the basic concepts of the phenomenon under our consideration first emerged. Peierls (1955) initially predicted that a one-dimensional metal, with electrons coupled to the underlying lattice, lacks stability at low temperatures [2]. The ground state of the coupled electron-phonon system exhibits a gap in the spectrum of single-particle excitations exactly at the Fermi energy. Additionally, there exists a collective mode consisting of electron-hole pairs with a wave vector $q = 2k_F$, k_F being the Fermi wave vector [5]. The charge density associated with the collective mode along coordinate $\mathbf{r}$ is given as

$$\rho(\mathbf{r}) = \rho_0 + \rho_1 \cos(2\mathbf{k}_F \cdot \mathbf{r} + \phi), \tag{1.1}$$

where ρ_0 is the unperturbed electron density of the system, while ρ_1 is an amplitude periodic density deformation, and this condensate is called the charge density wave [5]. Similarly to superconductors, the order parameter is complex and the phase ϕ of the condensate is of great importance; its time and spatial derivatives are related to the electric current and to the condensate density [5].

The reemergence of these merely theoretical initial concepts occurred when the first materials possessing highly anisotropic crystal and electronic structures were accessible [5]. The occurrence of charge density wave ground states has been extensively documented in a wide spectrum of low-dimensional materials.

Although certain organic materials and the pseudo-organic compound potassium platinocyanide (KCP) have shown evidence of collective dynamical effects through optical and dielectric measurements [6], transport phenomena clearly associated with the dynamics of the collective mode

have been found to date mainly in various inorganic linear-chain compounds [5]. The phenomenon of moving charge density waves (CDWs) was probably first documented by Fogle and Perlstein in 1972 [7]. They observed non-linear electrical conduction at low electric fields in a compound known as $K_{0.3}MoO_3$, commonly referred to as the blue bronze. These observations were made at temperatures below a metal-insulator transition [7]. Despite receiving limited attention, previous studies on the material $NbSe_3$ have shown that nonlinear conduction and the anomalous microwave conductivity provide clear evidence of the collective nature of electrical conduction [5, 8]. This is evident because the energy scale associated with the applied direct current (DC) field or alternating current (AC) frequency is significantly smaller compared to the energy scales required for energy- and frequency-dependent single-particle conduction. The rapid advancement in the field and the emergence of numerous experimental observations, which were only partially explained by theories of the time, were triggered by the discovery of additional inorganic and organic linear-chain compounds exhibiting a charge density wave ground state and displaying an unusual reaction to combinations of DC and AC excitations [5].

Although the charge density waves were later observed in materials that have two- or three-dimensional band structures, they were primarily considered as a one-dimensional phenomenon. Consequently, most of the discussions concerning the ground state and the phase transition were based on idealised, one-dimensional models [5].

1.2.1 The Peierls transition

The aforementioned idealised model is a one-dimensional metallic system at zero temperature. In the absence of electron-electron or electron-phonon interaction, the ground state is represented by the configuration shown in Fig. 1.1 (a). The electron states are occupied up to the Fermi level, denoted as ε_F. The lattice is a periodic array of atoms with a lattice constant a [5]. When an electron-phonon interaction is present, an emerging periodic lattice distortion with a period Λ is energetically favourable. This period Λ is related to the Fermi wave vector k_F by

$$\Lambda = \frac{\pi}{k_F}. \tag{1.2}$$

The presence of this distortion results in the creation of a gap at the Fermi level, as shown in Fig. 1.1 (b), where the situation for a half-filled band is illustrated. Since the occupation of states is limited to a maximum of $\pm k_F$, the presence of a gap in the system results in a decrease in electronic energy. In one dimension, the magnitude of the single-particle gap Δ is proportional to the amplitude of the periodic lattice distortion, denoted as u, and the decrease of the electronic energy is proportional to $u^2\ln(u)$ for small displacements. The distortion also leads to

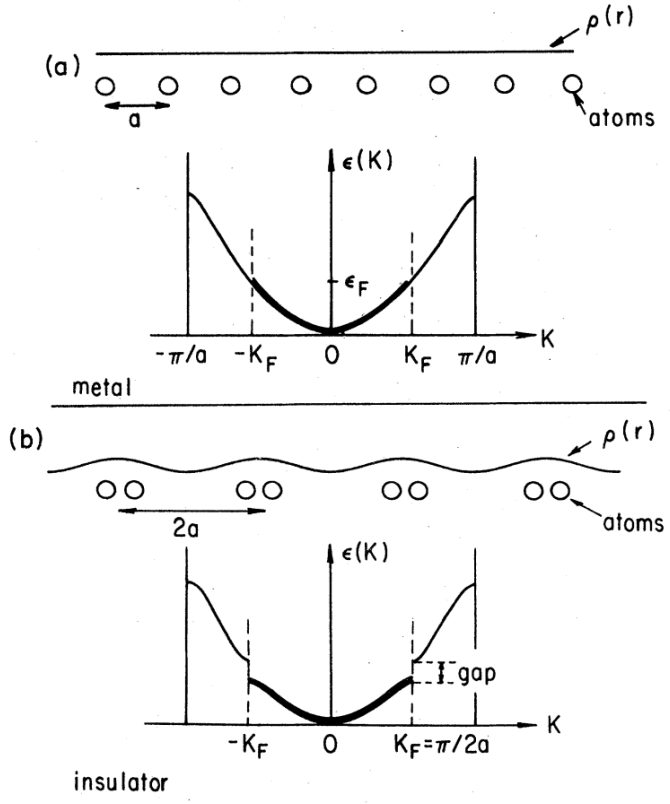

Figure 1.1: Peierls distortion in a one-dimensional metal with a half-filled band, shown in the first Brillouin zone where k is an electron wave vector, a is the initial lattice constant, k_F is the Fermi wave vector: (a) undistorted metal; (b) Peierls insulator with dimerised lattice (periodicity $\Lambda = 2a$) and periodic distribution of electron density. Image from [5].

a corresponding increase in elastic energy proportional to u^2 [9]. As a result, for a small but optimal distortion, the overall energy of the electron-phonon system, that is coupled, is lower than that of the undistorted metal [5]. The determination of the gap size and distortion magnitude can be achieved by examining the condition that leads to the maximum of condensation energy. The modification of the dispersion relation results in a spatially varying electron density, similar to the nearly-free-electron theory of metals [5]. The density will be a periodic function of the position with the period given by Λ.

The electron-phonon interaction is screened at finite temperatures by normal electrons excited across the single-particle gap. This, in turn, reduces the gap [10] and the degree of the lattice distortion, finally leading to a second-order transition at the so-called Peierls temperature T_c. Above the transition, the material is a metal, whereas below T_c, it is a semiconductor with a temperature-dependent gap $\Delta(T)$. The mean-field treatment of the 1D electron-phonon

Hamiltonian can be used to define the key characteristics of this so-called Peierls transition and collective mode [5]

$$H = \sum_{k,s} \varepsilon_k c^+_{k,s} c_{k,s} + \sum_{k,s} \hbar\omega_q b^+_q b_q + \sum_{k,q,s} g_q c^+_{k+q,s} c_{k,s} \left(b_q + b^+_{-q}\right), \tag{1.3}$$

where $c^+_k(c_k)$, $b^+_k(b_k)$ are the electron and phonon creation (annihilation) operators with momenta k and q, s denotes the spin, ε_k and ω_k are the electron and phonon dispersions, and g_k is the electron-phonon coupling constant [5].
Defining a complex order parameter

$$\Delta e^{i\phi} = g_{2k_F} \langle b_{2k_F} + b^+_{-2k_F} \rangle, \tag{1.4}$$

where Δ and ϕ are real, while $\langle ... \rangle$ denotes an average, the displacement field of the ions is given by

$$\langle b_{2k_F} + b^+_{-2k_F} \rangle e^{2ik_F x} + c.c. = \frac{2\Delta}{g_{2k_F}} \cos(2k_F x + \phi). \tag{1.5}$$

The electronic part of the Hamiltonian can be diagonalized by setting up a self-consistent equation in the mean-field (MF) approximation by replacing b_{2k_F} with $\langle b_{2k_F} \rangle$ and using a linear dispersion relation to describe the electron band near the Fermi energy ε_F,

$$\varepsilon_k = v_F \left(|k| - k_F\right), \tag{1.6}$$

where v_F is the Fermi velocity. The thermodynamic properties of the charge density wave state have strong similarities to those of a superconducting ground state [10, 11]. The gap, denoted as Δ, in terms of the dimensionless electron-phonon coupling constant $\lambda = g^2_{2k_F}(\omega_{2k_F}\varepsilon_F)^{-1}$, is determined by the BCS gap equation at $T = 0$,

$$\Delta = 2De^{-1/\lambda}, \tag{1.7}$$

where the cutoff energy D is the one-dimensional band-width, ε_F is the Fermi energy, ω_{2k_F} is the phonon mode frequency at $2k_F$. The temperature dependence of Δ is also BCS-like and vanishes at the transition temperature $T_c = \Delta(T = 0)/1.76k_B$ [5]. The spatial dependence of the electron density can be evaluated, and at $T = 0$,

$$\rho(x) = \rho_0 + \rho_0 \frac{\Delta}{\lambda v_F k_F} \cos(2k_F x + \phi) \tag{1.8}$$

where ρ_0 is the electron density with no electron-phonon interaction, and in one-dimension is given by $\rho_0 = \pi/k_F$. Superconductivity-like characteristics include the emergence of a gap in the single-particle excitation spectrum and the collective mode, which is characterised by a complex order parameter [5]. On the other hand, the collective mode here is formed by electron-hole pairs, involving the wave vector $2k_F$, as electrons and holes on the opposite side of the Fermi surface are combined to form the CDW and the accompanying lattice distortion [5]. Moreover, in contrast to the characteristic phonon frequency that enters the superconducting gap, the transition temperatures are significantly higher than those of superconductors due to the large cutoff frequency D that appears in the gap equation. The fact that in 1D the CDW state is stable at $T = 0$ for whatever small electron-phonon coupling constant λ is due to the logarithmically divergent response function in the static $(\omega = 0)$ limit. Subsequently, materials exhibiting a pronounced anisotropic band structure have an increased propensity for CDW formation; this is typically the result of a crystal structure in which chains are formed along one direction [5].

In the following part, we will explore more about how this divergent response function influences the formation of a CDW ground state for an electron gas in one dimension.

1.2.2 A 1D electron gas

The Fermi surface of a one-dimensional electron gas is very simple. It consists of two points, one at $+k_F$, and the other at $-k_F$. In the case of a very anisotropic metal, the Fermi surface consists of two sheets separated by a mean distance of $2k_F$. The dispersion relation of a 1D free electron gas is $\varepsilon(k) = \hbar^2 k^2/2m$, and the Fermi energy can be written as:

$$\varepsilon_F = \frac{\hbar^2}{2m}\left(\frac{N_0\pi}{2L}\right)^2 = \frac{\hbar^2 k_F^2}{2m} \tag{1.9}$$

where N_0 is the number of electrons, L is the length od the 1D chain, and m is the free electron mass [4]. Then, we can write the Fermi wave vector as $k_F = \frac{N_0\pi}{2L}$, where N_0 is the number of electrons per unit length. The density of states is

$$n(\varepsilon) = \frac{L}{\pi\hbar}\left(\frac{m}{2\varepsilon}\right)^{1/2}. \tag{1.10}$$

The distinct configuration of the Fermi surface gives rise to a distinct reaction to an external disturbance that is significantly different to the response observed in higher dimensions. The response of an electron gas to a time independent potential in d dimensions $(d = 1,2,3)$ is,

within the linear response theory, described by the Lindhard function:

$$\chi(\mathbf{q}) = \int \frac{d\mathbf{k}}{(2\pi)^d} \frac{f_{\mathbf{k}} - f_{\mathbf{k}+\mathbf{q}}}{\varepsilon_{\mathbf{k}} - \varepsilon_{\mathbf{k}+\mathbf{q}}} \tag{1.11}$$

where $f_{\mathbf{k}} = f(\varepsilon_{\mathbf{k}})$ is the Fermi function. For a three-dimensional spherical Fermi surface a simple calculation gives

$$\chi(\mathbf{q}) = -e^2 n_F \left[1 + \frac{1-x^2}{2x} \ln\left|\frac{1+x}{1-x}\right|\right] \tag{1.12}$$

where n_F is the density of states at the Fermi level, and $x = q/2k_F$. Susceptibility $\chi(\mathbf{q})$, given by (1.12), decreases with increasing q and the derivative has a logarithmic singularity at the point $q = 2k_F$ [4]. For a one-dimensional electron gas, the situation becomes different. For

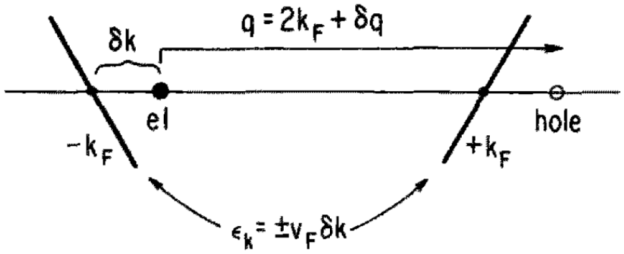

Figure 1.2: The dispersion relation for a free electron gas. The linearised dispersion $\varepsilon - \varepsilon_F = \pm v_F(k - k_F)$ is used to evaluate the response function in (1.14). The image shows schematically electron - hole pairing by the $2k_F$ perturbation around the Fermi surface. Image from [4].

wave vectors around $2k_F$, we can evaluate $\chi(q)$ assuming a linear dispersion relation around the Fermi energy ε_F, as shown in Fig. 1.2,

$$\varepsilon - \varepsilon_F = \hbar v_F(k - k_F). \tag{1.13}$$

Evaluating the integral in (1.11) near $2k_F$, we obtain:

$$\chi(q) = -e^2 n_F \ln\left|\frac{q+2k_F}{q-2k_F}\right|. \tag{1.14}$$

In comparison to a 3D electron gas, it is seen that the response function in a one-dimensional system exhibits a divergence at the wave vector $q = 2k_F$. For small values of q, $\chi(q)$ is given by the Thomas-Fermi approximation, $\chi(q) = -e^2 n_F$. The response function, evaluated for

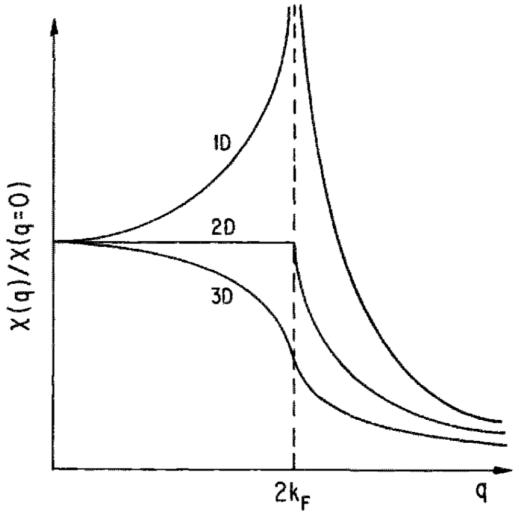

Figure 1.3: Wave vector-dependent Lindhard response function for a 1D, 2D, and 3D free electron gas at zero temperature. Image from [4].

arbitrary values of q is shown in Fig. 1.3, where $\chi(q)$ for a two- and three- dimensional electron gas is also shown for the sake of completeness. The fact that $\chi(q)$ diverges for $q = 2k_F$ in the 1D case has several important consequences [4].

Equation (1.14) indicates a divergent response. This suggests through self-consistency, that at $T = 0$ the electron gas itself is unstable with respect to the formation of a periodically varying electron charge (or electron spin) density [4] with the period Λ related to k_F by the relation (1.2). The reason for the divergence of the response function at $q = 2k_F$ can be attributed to the specific topology of the Fermi surface, which is commonly referred to as *the perfect nesting* [4]. Equation (1.11) shows that, the most significant contributions to the integral come from pairs of states - one full, one empty - related by the single wave vector $q = 2k_F$ and have the same energy, so they give a divergent contribution to $\chi(q)$. However, in higher dimensions, the quantity of these states is noticeably diminished, as shown in Fig. 1.3, resulting in the removal of the singularity at $2k_F$. The quasi-1D character of the Fermi surface can be modeled within the tight binding approximation (TBA) by including a dispersion corresponding to the directions perpendicular to the chains. The dispersion relation

$$\varepsilon(k_x, k_y) = \varepsilon_0 + 2t_a \cos(k_x a) + 2t_b \cos(k_y b) \tag{1.15}$$

where a and b are the lattice constants in the x and y directions, ε_0 is the unperturbed atomic energy, leads to the first neighbour TBA 2D band structure. For $t_a \gg t_b$, and again using a

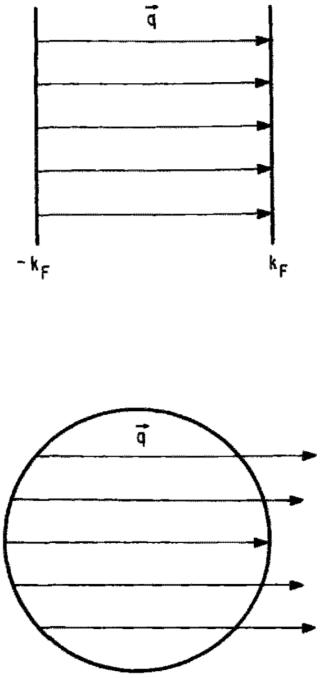

Figure 1.4: Fermi surface topology of a 1D and 2D free electron gas. The arrows indicate pairs of states, one full and one empty, differing by the wave vector $|\mathbf{q}| = 2k_F$. Image from [4].

linearised dispersion in the x direction, this dispersion, close to the Fermi energy, reduces to

$$\varepsilon(k) = \varepsilon_0 + v_F \delta k - 2t_b \cos(k_y b) \tag{1.16}$$

where $\delta k = k - k_F$. The Fermi surface is determined by the condition

$$k_x = k_F + \frac{2t_b}{v_F} \cos(k_y b) + O(t_b^2 \cos^2(k_y b)) + ... \tag{1.17}$$

Taking into account only the first-order approximation in t_b (with the omission of the third term in (1.17)) [4], the approximation yields a sinusoidal Fermi surface in the $k_x - k_y$ plane, as shown in Fig. 1.5. As for one dimension, a significant quantity of electron-hole pairs with similar energies can be observed. The condition for this is now given by the wave vector $\mathbf{Q} = (2k_F, \pi/b)$, as shown in Fig. 1.5. The response function $\chi(\mathbf{q})$ exhibits a singularity at $\mathbf{q} = \mathbf{Q}$ which leads to a periodic modulation characterised by a wave vector $q_{\parallel} = 2k_F$ in the x direction and $q_{\perp} = \pi/b$ in the y direction.

The achievement of perfect nesting, as illustrated in Fig. 1.5, occurs only in the limit when the ratio $t_b/t_a \to 0$ and is expected to be appropriate for materials with a substantial anisotropy.

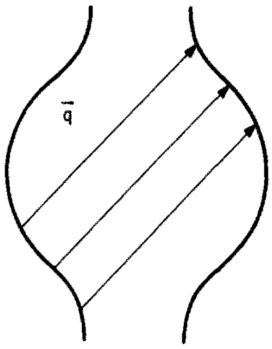

Figure 1.5: Fermi surface of a quasi-1D electron gas. The arrows indicate perfect nesting for small dispersion in one direction as discussed in the text. With increased dispersion, perfect nesting is no longer possible. Image from [4].

With increasing t_b/t_a the last term in (1.17) becomes progressively more important and the nesting condition applies for a smaller number of electron-hole pairs. This leads to the gradual removal of the singularity of the response function [4].

The results shown in this section work for explaining the emergence of a CDW ground state in quasi-1D materials, based on the FS nesting, being the paradigmatic mechanism for explanation of the CDW instability.

1.2.3 Early experimental discoveries

The early studies of quasi-1D conductors were driven by a proposition put forth in 1964 by W. A. Little, suggesting that some polymer chain compounds may potentially demonstrate superconductivity at a notably elevated critical temperature [12].

Monceau *et al.* provided the first experimental observations of the CDW transport in linear chain compounds composed of transition metal trichalcogenides. This discovery, published in 1976, marked the first documented proof of CDW transport in inorganic materials of this nature [8]. They reported the suppression of longitudinal resistivity anomalies by electric fields at temperatures of 145 and 59K. They attributed the observed suppression to Zener breakdown [13] across extremely small gaps introduced by the presence of charge density waves.

Chapter 2

The intercalated graphite compounds - materials considered in this work

2.1 Graphene

Graphene is a substance that holds considerable scientific significance. The monolayer, consisting of a solitary arrangement of carbon atoms, was first introduced to the scientific community in 2004 through the groundbreaking study conducted by Sir Andre Geim and Sir Konstantin Novoselov, esteemed scholars affiliated with the University of Manchester [14]. By utilising a straightforward yet innovative methodology involving the use of adhesive tape, the researchers effectively achieved the isolation and characterisation of this remarkable substance. This accomplishment then initiated a novel phase of scientific investigation, ultimately leading to the recognition of their endeavours through the prestigious Nobel Prize in Physics in the year 2010.

Graphene exhibits extraordinary characteristics. The material in question demonstrates remarkable mechanical strength, despite its thickness of only one atom [15]. This characteristic establishes novel benchmarks for the field of materials. The electronic properties of this material are of considerable interest due to its distinctive band structure, which exhibits a resemblance to the electronic dispersion of a Dirac cone. This characteristic has sparked significant attention from both theoretical and practical perspectives.

Furthermore, it should be noted that graphene exhibits exceptional thermal conductivity [16] and impermeability [17], rendering it highly advantageous for various applications spanning from nanoelectronics to composite materials. The relevance of this finding extends beyond its initial identification, exerting influence on various industries such as electronics, energy storage, and materials science.

2.1.1 Basics of graphene structure

Carbon, the sixth element in the periodic table, possesses a ground-state electrical structure of $1s^2 2s^2 2p_x^1 2p_y^1 2p_z^0$, as shown in Fig. 2.1 under (b) [18]. For convenience, the energy level of the $2p_z$ orbital is maintained in an unoccupied state, despite its equivalence to the energy levels of the $2p_x$ and $2p_y$ orbitals. As depicted in Fig. 2.1 (a), the nucleus of a carbon atom is surrounded by six electrons, with four of them being valence electrons. The valence shell of a carbon atom has the ability to undergo three distinct types of hybridisation, specifically sp, sp^2, and sp^3. The development of sp^2 hybrids is depicted in Fig. 2.1 (c). Monolayer graphene is formed when carbon atoms share sp^2 electrons with their three adjacent carbon atoms, resulting in a honeycomb lattice [18]. The graphene crystal unit cell, as indicated by a purple parallelogram in Fig.2.1 (d), consists of two carbon atoms. The unit-cell vectors $\mathbf{a_1}$ and $\mathbf{a_2}$ determine an identical lattice constant of 2.46 Å. The stability of the planar ring is attributed to the resonance and delocalisation of the electrons [18]. In the context of a standard sp^2 hybridization process between adjacent

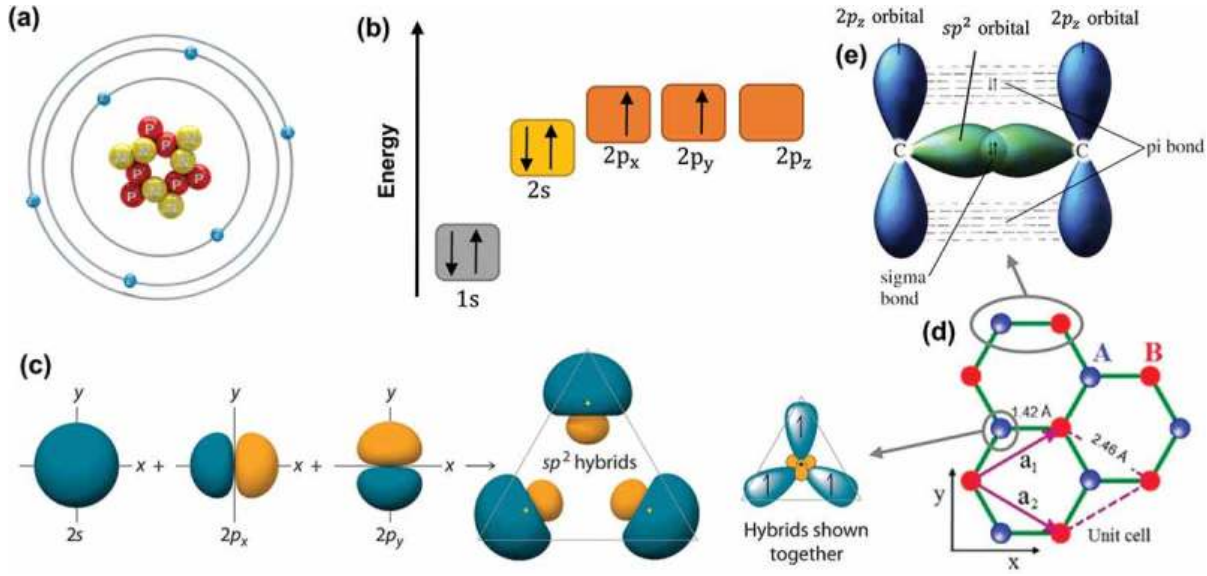

Figure 2.1: (a) Atomic structure of a carbon atom. (b) Energy levels of outer electrons in carbon atoms. (c) The formation of sp^2 hybrids. (d) The crystal lattice of graphene, where A and B are carbon atoms belonging to different sub-lattices, $\mathbf{a_1}$ and $\mathbf{a_2}$ are unit-cell vectors. (e) σ-bond, π-bond formed by sp^2 hybridisation. Image from [18].

carbon atoms inside a graphene layer (as shown in Fig. 2.1 (e)), a perpendicular out-of-plane π-bond is established through the utilisation of $2p_z$ orbitals. These orbitals are perpendicular to the planar structure. Simultaneously, an in-plane σ-bond is formed by the sp^2 ($2s$, $2p_x$ and $2p_y$) hybridized orbitals [18]. The covalent σ-bond that forms as a result has a relatively small interatomic length of approximately 1.42 Å. This characteristic makes it stronger than the sp^3

hybridised carbon-carbon bonds found in diamonds. Consequently, monolayer graphene exhibits exceptional mechanical properties, such as a Young's modulus of 1 TPa and an intrinsic tensile strength of 130.5 GPa [15, 18]. The formation of the conduction band and valence band with a zero band gap in monolayer graphene can be attributed to the presence of a half-filled π-band, which allows for the unrestricted movement of electrons. Moreover, the π-bonds facilitate a relatively weak van der Waals interaction between adjacent layers of graphene in bilayer and multi-layer graphenes [18].

2.1.2 Electronic band structure of graphene

In the hexagonal lattice of monolayer graphene, as seen in Fig. 2.2 (a), the two primitive lattice vectors are:

$$\mathbf{a_1} = \frac{a}{2}(1, \sqrt{3}) \tag{2.1}$$

$$\mathbf{a_2} = \frac{a}{2}(1, -\sqrt{3}) \tag{2.2}$$

where $a = \sqrt{3}a_0 \approx \sqrt{3} \times 1.42$ Å$= 2.46$ Å is the lattice constant (a_0 is the the interatomic distance). The position vector of atom B_l, $l = 1,2,3$ relative to the atom A_i is denoted by

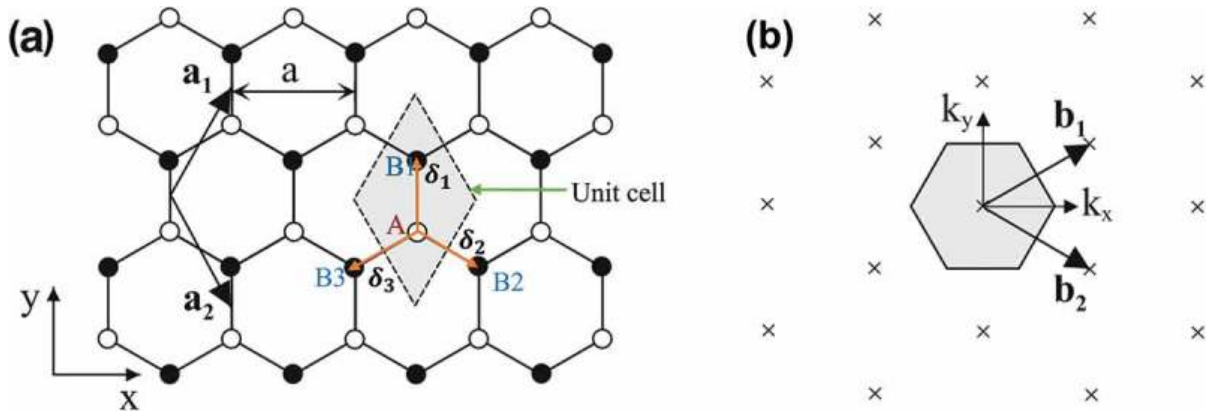

Figure 2.2: (a) Honeycomb lattice of monolayer graphene, where white (black) circles indicate carbon atoms on A (B) sites, and (b) the reciprocal lattice of monolayer graphene, where the shaded hexagon is the corresponding first Brillouin zone [19]. Image from [18, 19].

δ_l, and the vectors for the three closest neighbours of an atom in real space are given by

$$\delta_{\mathbf{1}} = \left(0, \frac{a}{\sqrt{3}}\right) \tag{2.3}$$

$$\delta_{\mathbf{2}} = \left(\frac{a}{2}, -\frac{a}{2\sqrt{3}}\right) \tag{2.4}$$

$$\delta_{\mathbf{3}} = \left(-\frac{a}{2}, -\frac{a}{2\sqrt{3}}\right) \tag{2.5}$$

It is noted that $|\delta_1| = |\delta_2| = |\delta_3| = \frac{a}{\sqrt{3}}$ is the spacing between two nearest-neighbouring carbon atoms. In Fig. 2.2(b) we can see an illustration of the reciprocal lattice of monolayer graphene, where the crosses are reciprocal lattice points, and the first Brillouin zone is represented by the shaded hexagon. The primitive reciprocal lattice vectors $\mathbf{b_1}$ and $\mathbf{b_2}$ satisfy the condition

$$\mathbf{a_i} \cdot \mathbf{b_j} = 2\pi\delta_{i,j} \qquad\qquad i, j \in 1, 2 \tag{2.6}$$

therefore, we get the expressions for the primitive reciprocal lattice vectors as:

$$\mathbf{b_1} = \left(\frac{2\pi}{a}, \frac{2\pi}{\sqrt{3}a}\right) \tag{2.7}$$

$$\mathbf{b_2} = \left(\frac{2\pi}{a}, -\frac{2\pi}{\sqrt{3}a}\right). \tag{2.8}$$

Normally, the electronic band structure of graphene can be calculated using the tight-binding approach (TBA) [20], and after a well known calculation, one gets the electron dispersion [18]:

$$E_j(\mathbf{k})_\lambda = \frac{\varepsilon_{2p} + \lambda\gamma_0 |f(\mathbf{k})|}{1 - \lambda s_0 |f(\mathbf{k})|} \tag{2.9}$$

where ε_{2p} is the energy of the $2p_z$ orbitals of carbon atoms, γ_0 is the value of the transfer integral matrix element between each nearest-neighbouring A and B atom, s_0 is the overlap parameter, the function $\mathfrak{f}(\mathbf{k})$ describes the nearest-neighbour hopping:

$$\mathfrak{f}(\mathbf{k}) = \sum_{l=1}^{3} e^{i\mathbf{k}\cdot\delta_\mathbf{l}} = e^{ik_y a/\sqrt{3}} + 2e^{-ik_y a/2\sqrt{3}} cos(k_x a/2), \tag{2.10}$$

and $\lambda = \pm 1$ represents the conduction and valence bands respectively in (2.9)[18]. The three parameters ε_{2p}, γ_0 and s_0 can be found by comparing this tight-binding model with fitting experiments, or by *ab initio* methods, such as density functional theory (DFT) [21, 18]. According to a review by Saito et al. [22] the values of ε_{2p}, γ_0 and s_0 are suggested to be 0 eV, 3.033 eV

and 0.129 eV. In this context, the notation $\varepsilon_{2p} = 0$ indicates that the energy associated with the $2p_z$ orbital is defined as the energy origin [18]. The band structure of graphene, as depicted in

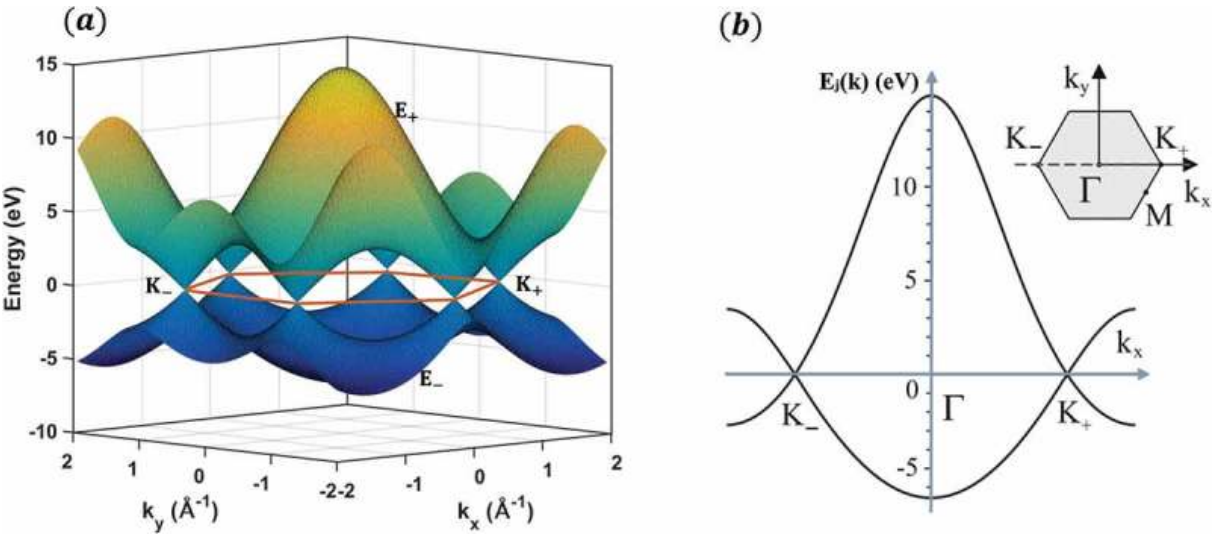

Figure 2.3: (a) Band structure of graphene calculated with a tight-binding method with $\varepsilon_{2p} = 0$ eV, $\gamma_0 = 3.033$ eV and $s_0 = 0.129eV$. (b) Cross-section through the band structure, where the energy bands are plotted as a function of wave vector component k_x along the line $k_y = 0$. Image from [18].

Figure 2.3 (a), is determined by substituting these three values into equation (2.9). Due to considerations of symmetry, the formation of two energy bands, namely the upper conduction band and the lower valence band, occurs in the monolayer graphene crystal structure due to electron hopping between the two equivalent carbon triangular sub-lattices. These energy bands intersect at points where the energy function $E_j(\mathbf{k})$ is identically zero. Furthermore, the Fermi level is located at these points commonly referred to as Dirac points [18]. Figure 2.3 (b) displays a specific line scan of the band structure, depicting the energy bands as a function of the wave vector component k_x along the line $k_y = 0$. In the inserted graph, the centre of the Brillouin zone is labeled Γ, while two opposite corners in which the two opposite Dirac points are located are labeled K_+ and K_- respectively. The dispersion in the vicinity of point $K_+(K_-)$ exhibits a linear behaviour and can be described by a Dirac-like Hamiltonian [18, 23, 24, 25]

$$H = -i\hbar v_F \boldsymbol{\sigma} \cdot \nabla \tag{2.11}$$

where $\hbar$ is the reduced Planck constant, $v_F \approx 10^6$ m/s is the Fermi velocity, $\boldsymbol{\sigma} = (\sigma_x, \sigma_y)$ are the Pauli matrices, and ∇ is the the gradient operator. The non-zero overlap parameter s_0 is responsible for the considerable asymmetry between the conduction band (E_+) and the valence band (E_-), particularly in the neighbourhood of the Γ point [18]. Nevertheless, the manipulation

of the electronic band structure of graphene can be easily achieved through the application of an electric field [14, 18, 26, 27, 28, 29, 30] or the utilisation of substrates [31, 32] and precisely engineered by introducing disorders into the hexagonal lattice [18, 33, 34].

2.1.3 Synthesis

Recently, multiple techniques have emerged for the synthesis of graphene. This synthesis process involves extracting graphene based on factors such as purity and the intended end product [35]. Following the discovery of graphene in 2004, various methods have been devised to generate graphene layers and thin films [36].

There are two primary methods for synthesising graphene, which can be classified as (i) top-down and (ii) bottom-up approaches. Top-down methodologies involve the conversion of bulk materials, such as graphite, into its smallest constituents in order to produce graphene [37, 38]. Several prominent top-down approaches have been identified in the literature [39]. These techniques encompass liquid-phase exfoliation [40], plasma etching [41], electrochemical exfoliation [42], laser ablation [43], ball milling [44], and chemical reduction [45].

On the other hand, under the bottom-up synthesis approach, the production of graphene involves the decomposition of carbon-containing precursors, which can be in the form of gases or liquids. This decomposition process is then followed by the construction of a hexagonal structure consisting of graphene layers [46]. Chemical vapour deposition (CVD) [47], thermal pyrolysis [48], and epitaxial growth [49] are often employed bottom-up methodologies in the fabrication of graphene.

2.2 The intercalated graphite CaC_6

Carbon exhibits various allotropic forms, with diamond, graphite, carbynes, fullerenes, and carbon nanotubes being some notable examples. At standard room conditions, graphite, characterised as a lamellar solid, is the most stable form. It consists of sp^2 hybridized carbon atoms forming two-dimensional graphene layers interconnected by relatively weak van der Waals bonds. The short carbon-carbon distance within the graphene planes (about 1.42 Å) arises from robust covalent bonds linking adjacent carbon atoms. In practice, two types of bonds stack: a σ-bond and a π_z-bond. All the π_z-bonds within the same graphene plane are delocalized on that plane. The weaker van der Waals bonds in the perpendicular direction result in a significantly larger distance of approximately 3.35 Å between the graphene planes [50].

The presence of both strong covalent and weak van der Waals bonds imparts highly anisotropic

properties to graphite. This property allows for soft chemical reactions, where reagents can selectively target areas of weak cohesion, commonly referred to as van der Waals gaps, without disrupting the covalent bonds. These gaps, often termed interplanar galleries, can expand to accommodate the necessary space for the reagent's action [50].

These particular soft reactions are known as intercalation reactions. In most instances, they are reversible, and the pristine graphite structure can often be restored through moderate heating. Carbon, owing to its intermediate electronegativity, exhibits amphoteric behaviour in these intercalation reactions, meaning it can either provide or accept electrons. The transfer of electrons plays a pivotal role in facilitating intercalation reactions [50].

2.2.1 Synthesis

It is well known that vapour phase intercalation of alkaline earth metals into graphite is more difficult than that of alkali metals. Additionally, compared to calcium (Ca), barium (Ba) and strontium (Sr) in the category of alkaline earth metals demonstrate a very simple intercalation process [51]. For instance, only superficial intercalation occurs when attempting to intercalate calcium vapour with a pyrolytic graphite platelet. In order to avoid the creation of calcium acetylide, it is also imperative to maintain a low reaction temperature. As a result, bulk calcium-graphite materials have not been made through a vapour phase reaction, and nothing is known about their crystal structure and other characteristics [50].

Innovative methods were employed in 2004 to successfully synthesise bulk and highly pure CaC_6. The experimental procedure consisted of submerging pyrolytic graphite into a molten Li-Ca alloy with a predetermined composition, as described by Pruvost et al. [52]. The efficacy of this reaction is contingent upon four pivotal factors: temperature, the exact composition of the alloy, the duration of the reaction, and the purity of the reagents. The significance of the reaction temperature lies in its impact on the structural integrity of graphene planes, which undergo degradation above the threshold of 450 °C. Fortunately, the introduction of lithium (Li) into calcium (Ca) has the advantageous effect of reducing the elevated melting point of calcium, which is recorded to be 839 °C according to Emery et al. (2009) in their synthesis study [50].

In order to achieve reproducibility of the reaction, it is crucial to utilise metallic reagents of exceptional purity and exercise meticulous handling techniques within a glove box that is filled with argon of high purity. Lithium (Li) and calcium (Ca) are precisely quantified in order to create an alloy with a Li/Ca ratio that falls within the specified range of 3 to 4. The process of melting occurs within a stainless steel tube, which is positioned in a vertical tubular furnace with the capability of attaining temperatures ranging from 400 to 450°C. In this particular stage, the alloy undergoes extensive agitation in order to attain a homogeneous liquid state [50].

Subsequently, a graphite platelet with dimensions of 5x15x0.2-0.5 mm is submerged into the molten alloy, and the reactor is tightly sealed in a regulated argon atmosphere. Following this, the reaction is carried out for a duration of ten days at a temperature of around 350°C. After the completion of this phase, the sample is extracted from the reactor and subjected to surface cleansing procedures, such as centrifugation within a temperature range of 300 to 350°C or cleavage. The generation of pure first-stage CaC_6 is ensured by a rigorous attention to the experimental conditions [50].

The intercalation mechanisms that result in the formation of CaC_6 were investigated using x-ray diffraction (XRD) techniques [53]. The dual role of lithium (Li) in this process is widely acknowledged. First and foremost, it serves as a flux for calcium (Ca), facilitating the reaction between liquid and solid phases to take place at reduced temperatures. Furthermore, Li facilitates the process of intercalating Ca by initially causing the expansion of the graphitic galleries during the early stages of the reaction. Indeed, throughout the initial hour of the reaction, compounds formed by the combination of lithium and graphite undergo a sequential progression through the fifth, fourth, third, second, and first stages. The utilisation of staging mechanisms is a prevalent phenomenon observed in intercalation reactions that involve pure metals and graphite [50].

2.2.2 Structure

The utilisation of the innovative approach introduced in the previous section significantly expedited the resolution of the CaC_6 crystal structure, enabling the synthesis of bulk CaC_6 [54]. It is well-known that during the initial phase, binary intercalation compounds of graphite and metal exhibit a very specific stoichiometry [50]. It has been experimentally shown that it corresponds to MC_8 for the biggest metals and to MC_6 for the smallest ones [50]. The stoichiometry of MC_8 (where M = K, Rb, and Cs) is observed when the interlayer distance is above 5.30 Å. Conversely, at interlayer distances smaller than this threshold, the composition MC_6 (where M = Li, Sr, Ba, Eu, Yb, and Ca) is observed. The latter stoichiometry corresponds to an AAA... stacking of the successive graphene planes, so that the metal atoms are located in prismatic hexagonal sites, and the adjacent graphene and metal planes are epitaxial [50]. In each graphitic gallery, only one out of three prismatic sites is occupied by a metal atom. Therefore, the metal plane can occupy three different positions in the graphitic interval denoted α, β and γ, so that three different c-axis stacking possibilities can be considered [50, 54], as shown in Fig. 2.5 In the initial scenario, it is evident that the parameter of the unit cell $c = d_i$, for the second stacking $c = 2d_i$, and for the third one $c = 3d_i$. The first stacking option results in hexagonal crystal symmetry, whereas the second stacking option also leads to hexagonal crystal symmetry. On the other hand, the third

$$A\alpha A\alpha A\alpha A\alpha A\alpha...$$
$$A\alpha A\beta A\alpha A\beta A\alpha...$$
$$A\alpha A\beta A\gamma A\alpha A\beta...$$

Figure 2.4: Possible stacking scenarios, image from [50].

stacking option corresponds to rhombohedral symmetry [50]. The initial stacking arrangement was just found in the case of LiC_6, whereas the remaining MC_6 compounds (SrC_6, BaC_6, EuC_6, SmC_6, and YbC_6) exhibit the second stacking configuration. CaC_6 exhibits distinct characteristics, with its rhombohedral symmetry aligning with the third stacking [50]. The X-ray diagram depicting the 001 reflections of CaC_6 reveals an interlayer spacing of 452.4 pm, as illustrated in Figure 2.5 [50]. The unambiguous establishment of the CaC_6 chemical formula is facilitated

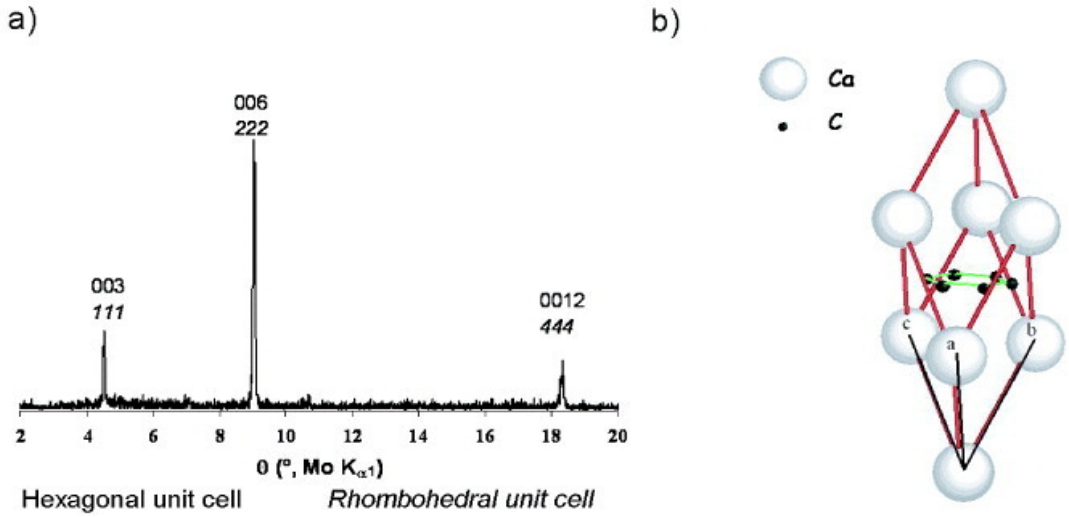

Figure 2.5: (a) [001] x-ray diffraction pattern. Reflexions are indexed in the hexagonal [001] and rhombohedral [hkl] representations (rhombohedral structure can be represented in both systems). (b) Crystal structure of CaC_6 (rhombohedral unit cell) [54] with a, b, c axis marked. Image from [50].

by the depiction of its c-axis electronic density profile. Finally, the stoichiometry was verified with a high level of accuracy using a nuclear microprobe [55, 56].

The lattice parameter of CaC_6 structure, determined by analysing the diffraction pattern acquired by the rotating crystal method, is approximately equal to 4.33 Å. It is very close to $a\sqrt{3}$, where a corresponds to pristine graphite. This result additionally confirms the CaC_6 stoichiometry [50].

Chapter 3

Motivation for this work

Charge density waves were observed experimentally by Rahnejat *et al.* in 2011 [57]. The phenomenon of electronic stripes in the graphitic superconductor CaC_6 has been seen and analysed by researchers through the utilisation of scanning tunnelling microscopy and spectroscopic techniques [57]. The observed stripes are in the form of a uniaxial charge density wave exhibiting a periodicity that is three times larger than that of the Ca superlattice along one of its unit vectors. The Ca intercalants exhibit positional modulation visible on Fig. 3.1, but no deformations of the carbon lattice are seen, suggesting that the graphene sheets can host a charge density wave. The utilisation of graphene, a really simple material, serves as a first foundation for comprehending the correlation between so called charge stripes and superconductivity. The experimental findings propose a methodology for investigating the presence of superconductivity in graphene. The material has also exceptional superconducting properties within its category, including the highest recorded superconducting temperature ($T_c = 11.5$ K) among all intercalated graphite compounds [57]. Atomic resolution STM imaging has been used to determine the structure and electronic local density of states (LDOS) of CaC_6 at 78 K (shown in Fig. 3.2), above the superconducting transition but below the anomalous transition. The technique accesses structural information and the electronic spectrum, including the CDW gap. The principal finding of the experiment is a stripe phase (CDW), with the underlying structure of the expected phase with an extra superposed long-range one-dimensional uniaxial modulation [57]. The Ca atomic resolution for the stripe phase is ~ 0.020 nm, much lower than the X-ray-measured C-Ca distance and the Ca^{2+} ionic radius. High-resolution imaging of the stripe phase requires a high-purity sample and a large flat graphene-terminated surface. The Ca superlattice is less prominent in real-space imaging at 300 mV than at 400 mV, allowing for individual analysis of each lattice. Higher resolution momentum space techniques, such as X-ray or neutron scattering, could be used to detect smaller average modulations [57].

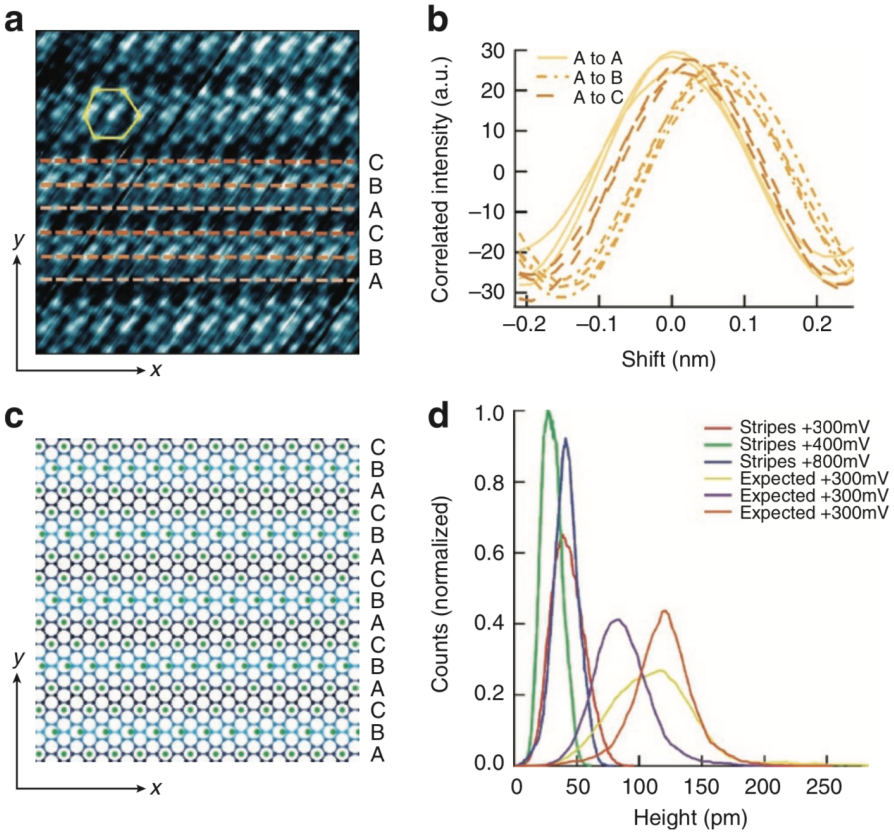

Figure 3.1: Surface structure and the broken symmetry of the Ca superlattice. (a) 5 nm × 5 nm drift-corrected topographic STM image with line profiles in the Ca-parallel-to-stripe symmetry direction marked on B, the stripe apex, and off A, C. (b) Correlation of line profiles shown in (a) demonstrate a 0.06 ± 0.02 nm perturbation of the Ca atoms along the stripe apex. (c) A schematic illustrating the distortion of the Ca lattice (green) and the resultant stripe modulation (blue scale) on the graphene sheet as seen in positive sample bias imaging oriented to match (a). (d) Topographic height distributions for three different striped surface areas at a number of sample biases (as indicated in the legend) and three expected phase surface regions at + 300 mV. Image from [57].

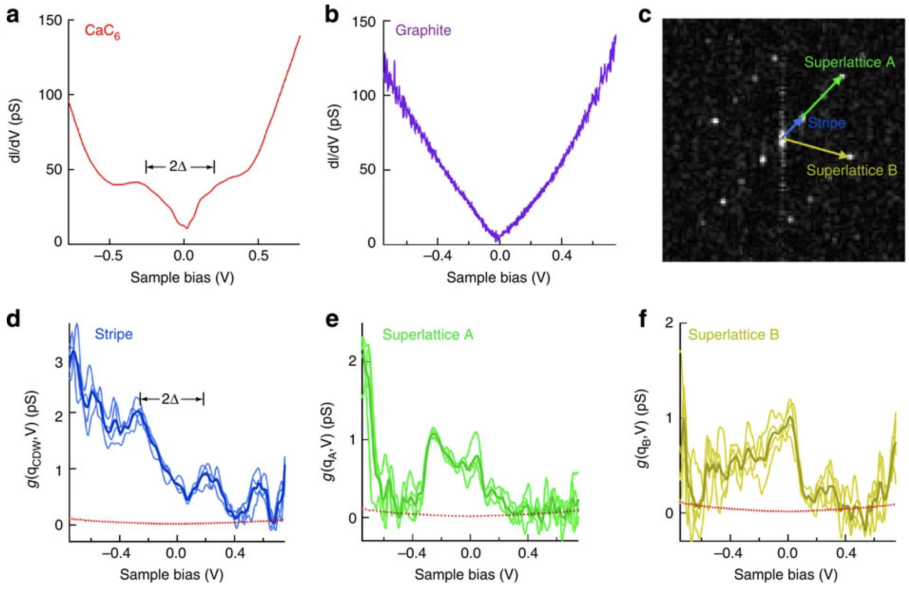

Figure 3.2: (a) Numerically differentiated and averaged (60000 spectra) spectroscopy, spatially averaged conductivity $g(V)$ recorded at +800 mV, 50 pA set point on CaC_6. (b) Numerically differentiated spectra recorded at the same set point on pristine graphite. (c) $g(\mathbf{q},V)$ Fourier transform scanning tunnelling spectroscopic image at 0 mV. (d-f) $g(\mathbf{q},V)$ Fourier intensity plotted as a function of energy for the stripe (**d**, blue) and Superlattices A and B (**e**, green and **f,** yellow) spots marked in (b) respectively. Faint lines represent individual datasets, bold lines represent average. Red dotted line is the background intensity (already subtracted from all lines presented). Image from [57].

The presence of a charge density wave has also been observed by Shimizu *et al.* in Ca-intercalated bilayer graphene C_6CaC_6, which is the lowest possible thickness of the superconducting C_6Ca material [58]. The CDW is induced by the potential modulation due to the commensurate lattice matching between the C_6CaC_6 film and the SiC substrate. The phenomenon of superconductivity was not detected in the epitaxial growth of C_6CaC_6 on a SiC substrate. However, an alternative charge density wave arrangement, distinct from the surface of bulk C_6Ca, was discovered [58].

ARPES measurements were conducted at Tohoku University utilising a VG-Scienta SES2002 electron analyser equipped with a high-intensity helium discharge lamp and a toroidal grating monochromator. The confirmation of the gap structure occurred exclusively at a temperature of 5 K and remained unaffected by the presence of an external magnetic field [58]. The investigation conducted an analysis of the scanning tunnelling spectroscopy (STS) spectrum of C_6CaC_6 in the absence of a magnetic field, which resulted in the identification of a distinct energy gap with a magnitude of around 70 meV at a temperature of 5 K.

The energy-gap value in bulk C_6Ca is 6-7 times larger than that of C_6CaC_6, and the transition

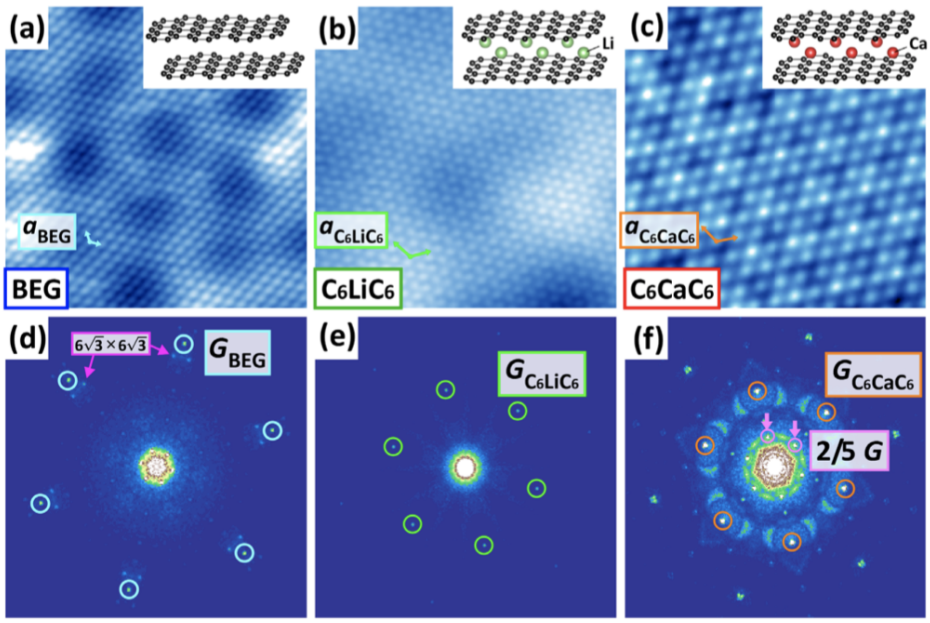

Figure 3.3: Comparison of STM results for bilayer epitaxial graphene (BEG), C_6LiC_6, and C_6CaC_6. (a)-(c) STM images of (a) BEG, obtained with a sample bias voltage (V_s) of -500 mV and a tunnelling current (I_t) of 30 pA. (b) C_6LiC_6 ($V_s = -100$ mV, $I_t = 30$ pA), and (c) C_6CaC_6 (V_s = -100 mV, I_t = 30 pA). All the images were taken at 5 K in 6 nm $\times$ 6 nm. The arrows indicate the unit vectors. The insets show the schematic illustrations of each material. (d)-(f) FFT images of the corresponding STM images (a)–(c). Each FFT image is characterised by **(d)** the reciprocal lattice spot of $\mathbf{G}_{\mathrm{BEG}}$ with the $(6\sqrt{3}\times6\sqrt{3})$ -$R30^\circ$ satellite, (e) the additional spot $(\mathbf{G}_{C_6LiC_6})$ with $(\sqrt{3}\times\sqrt{3})$ $R30^\circ$ periodicity, and (f) the $(\sqrt{3}\times\sqrt{3})$ - $R30^\circ$ spot $(\mathbf{G}_{C_6CaC_6})$ with a distinct spot corresponding to $\frac{2}{5}\mathbf{G}_{C_6CaC_6}$. Image from [58].

temperature is much higher in the bulk crystal than in the thin film [58]. Although theoretical studies have predicted the possibility of superconductivity in C_6CaC_6 [59, 60], no superconducting transition has been observed in epitaxially grown C_6CaC_6 on SiC [58].

The findings in this work that sparked our interest for future theoretical investigation were both the STM results for C_6CaC_6 that show a clear CDW phase shown in Fig. 3.1, 3.2 (a), 3.3 (c), (f). As seen from Fig. 3.3, C_6LiC_6 does not exhibit a striped ground state, contrary to C_6CaC_6, we also aim to provide an explanation for these observed differences.
To summarise, the experiments show:

1. The uniaxial CDW ordering is established below 250 K in the graphene sheets which are chemically doped by electrons from the Ca atoms with 0.2 electrons per carbon atom. Due to the CDW formation, the CaC_6 unit cell gets tripled along one of its primitive vectors inclined by 30 degrees with respect to the direction perpendicular to the charge lines. The charge lines are formed along the graphene armchair direction and are periodically

distributed with a distance equal to 4.5 graphene lattice constants along the graphene zig-zag direction.

2. The pseudo-gap appears around the Fermi energy in the CDW-ordered phase.

3. The Ca-superlattice is distorted in a way that every Ca atom along the CDW apex is shifted by 0.06 ± 0.02 nm in the same direction, with respect to the other two parallel lines of Ca atoms between the CDW peaks.

It is important to note that the pseudo-gap at the Fermi energy does not necessarily need to appear only due to the formation of the CDW state. In doped graphene it can also appear in the STS signal due to phonon-assisted electron tunneling [61]. Therefore, in a quantitative analysis of the CDW, aiming to compare with STS experiments, that contribution should be subtracted.

Among earlier experimental findings of charge ordering in intercalated graphites e.g. [62, 63] we find experimental studies described in this section providing us sufficient information to base our minimal theoretical model on. The next step is to set up the theoretical framework for further analysis and construction of the model.

Chapter 4

The minimal model

4.1 Geometry of the problem and the initial Hamiltonian

The geometry of the problem in real and reciprocal space is presented schematically in Fig. 4.1 and Fig. 4.2 respectively. The graphene crystal lattice is defined by the primitive vectors $\mathbf{a_1}$ and $\mathbf{a_2}$, and the calcium superlattice is defined by the primitive vectors $\mathbf{b_1}$ and $\mathbf{b_2}$.

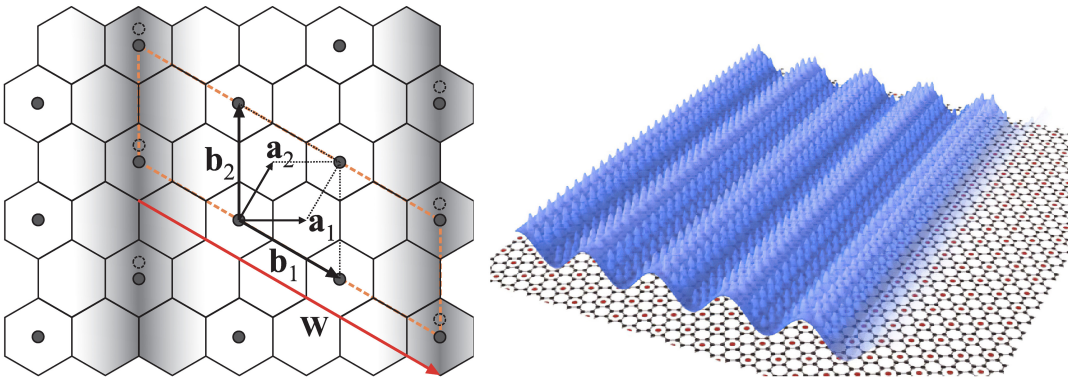

Figure 4.1: Left panel: Carbon atoms form the honeycomb lattice (unit vectors are $\mathbf{a}_{1,2}, a \equiv |\mathbf{a}_{1,2}| = 2.5$Å, the area of the cell is $A_C = 5.41$Å^2. Ca atoms (circles) form the hexagonal superlattice (unit vectors are $\mathbf{b}_{1,2}, b \equiv |\mathbf{b}_{1,2}| = \sqrt{3}a = 4.32$Å , the area of the cell is $A_{CaC_6} = 16.16$Å^2). The CDW charge stripes (shaded) are formed along the armchair direction, characterised by the vector $\mathbf{W} = 3\mathbf{b}_1$ that triples the CaC_6 cell along $\mathbf{b}_1$. The Ca-lattice distortion (shift of the Ca atoms under the CDW peaks by 0.06 ± 0.02 nm) due to CDW formation is depicted by the dashed circles. The unit cell of the CDW-reconstructed system is marked by the dashed orange rhombus. Right panel: The intercalating Ca atoms (red dots) form the hexagonal superlattice upon the honeycomb graphene lattice (grey). The electron CDW (blue) in the π-bonds of graphene (chemically doped) spreads periodically along the graphene zig–zag direction.

We describe a coupled system of electrons and phonons by the 2D Fröhlich Hamiltonian

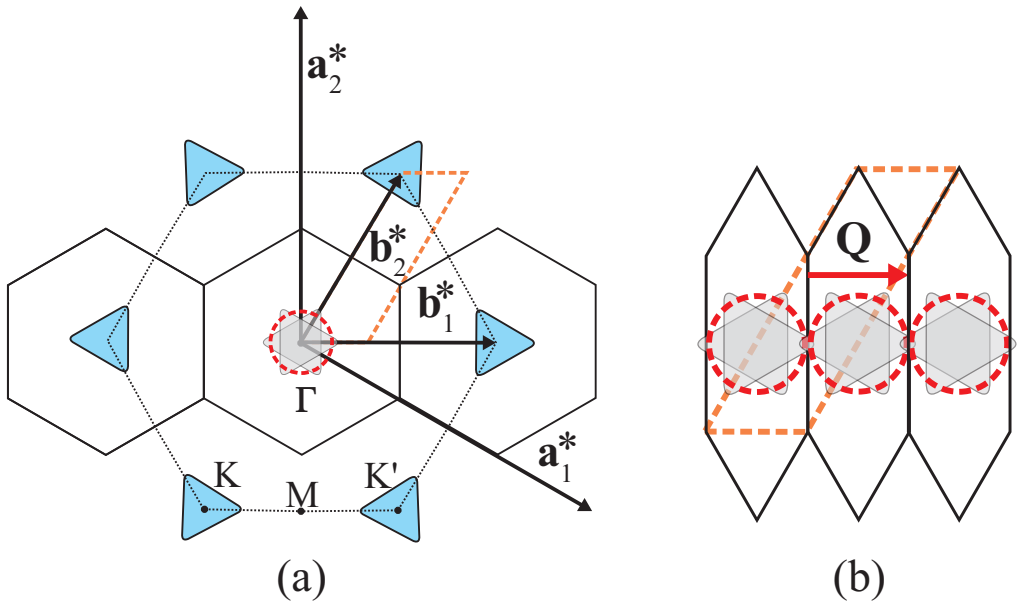

Figure 4.2: A schematic representation of the reciprocal space (a) The carbon Brillouin zone (BZ) is depicted by the dashed hexagon, with standard Γ, K, K', M points (unit vectors are $\mathbf{a}^*_{1,2}, a \equiv |\mathbf{a}_{1,2}| = 2.9\text{Å}^{-1}$). The triangles at the K, K' points represent the Fermi surfaces (FS) of the chemically doped carbon layer [64]. The Ca-superlattice (unit vectors are $\mathbf{b}^*_{1,2}$, $b \equiv |\mathbf{b}_{1,2}| = 1.68\text{Å}^{-1}$) folds the carbon BZ to a three times smaller CaC_6 BZ (solid hexagon). All 6 FSs, from carbon K and K' points, fall into the Γ point (shaded), approximated by a circle of the same area S_{F0} depicted by the dashed red circle. The chemical doping of $\xi \approx 0.2$ electrons per carbon atom is related to the area of the Fermi pocket $S_{F0} = 2\pi^2\xi/A_{CaC_6} = 0.244$ Å^{-2} , which gives an average Fermi wave number $k_{F0} = 0.28\text{Å}^{-1}$. (b) The CDW potential, with the wave vector $\mathbf{Q}||\mathbf{b}^*_1$ of periodicity $Q = b^*/3 = 0.56\text{Å}^{-1}$, folds the CaC_6 BZ, bringing the FSs into touch (or slight overlap). The orange rhombus represents the reciprocal primitive cell of the reconstructed system.

[65, 66, 67]:

$$H = \sum_{\mathbf{k}} \varepsilon(\mathbf{k}) a^\dagger_{\mathbf{k}} a_{\mathbf{k}} + \sum_{\mathbf{q}} \hbar\omega(\mathbf{q}) b^\dagger_{\mathbf{q}} b_{\mathbf{q}} + \frac{1}{\sqrt{A}} \sum_{\mathbf{k},\mathbf{q}} g_{\mathbf{q}} a^\dagger_{\mathbf{k}+\mathbf{q}} a_{\mathbf{k}} \left(b^\dagger_{-\mathbf{q}} + b_{\mathbf{q}} \right), \tag{4.1}$$

where $a_{\mathbf{k}}$ and $b_{\mathbf{q}}$ are the standard electron and phonon field operators with the corresponding 2D wave vectors $\mathbf{k}$ and $\mathbf{q}$ respectively, $\varepsilon(\mathbf{k}) = \hbar v_F |\mathbf{k}|$ is the Dirac-like electron dispersion with the Fermi velocity v_F, $\omega_{\mathbf{q}}$ is the phonon frequency and $g_{\mathbf{q}}$ is the electron-phonon coupling constant at wave vector $\mathbf{q}$, A is the area of the 2D sample. The first term in the Hamiltonian (4.1) describes the noninteracting 2D electrons, the second term represents noninteracting phonons, and the third term describes electron-phonon coupling.

The formation of the CDW with the wave vector $\mathbf{Q}$ implies a static lattice deformation, i.e. the nonvanishing phonon operator expectation value $\langle b_{\mathbf{q}=\mathbf{Q}} \rangle$ with corresponding complex order parameter

$$\Delta e^{i\Phi} = \frac{2g_{\mathbf{Q}} \langle b_{\mathbf{Q}} \rangle}{\sqrt{A}}, \tag{4.2}$$

where Δ and Φ are its amplitude and phase. $\mathbf{Q}$ and Δ are to be determined self-consistently by the maximisation of the total condensation energy of the CDW state, while phase Φ is not important in the model considering only the ground state, i.e. not considering processes involving some aspects of collective dynamics of the CDW. The Hamiltonian (4.1) is treated within the mean-field approximation [68], which appears sufficient to provide a minimal zero-temperature model to reveal the analytical picture explaining the above-counted experimental facts, i.e.

$$H_{MF} = \sum_{\mathbf{k}} \left[\varepsilon(\mathbf{k}) a^{\dagger}_{\mathbf{k}} a_{\mathbf{k}} + \Delta e^{i\Phi} a^{\dagger}_{\mathbf{k}+\mathbf{Q}} a_{\mathbf{k}} + \Delta e^{-i\Phi} a^{\dagger}_{\mathbf{k}-\mathbf{Q}} a_{\mathbf{k}} \right] + \frac{A\hbar\omega_{\mathbf{Q}}}{2g^2_{\mathbf{Q}}} \Delta^2. \tag{4.3}$$

The final term in Eq. (4.3) accounts for the elastic energy of the statically deformed lattice, whereas the first term is simply diagonalised, providing the new electron bands

$$E_{\pm}(\mathbf{k}) = \frac{1}{2} \left[\varepsilon(\mathbf{k} - \tfrac{\mathbf{Q}}{2}) + \varepsilon(\mathbf{k} + \tfrac{\mathbf{Q}}{2}) \pm \sqrt{\left(\varepsilon(\mathbf{k} - \tfrac{\mathbf{Q}}{2}) - \varepsilon(\mathbf{k} + \tfrac{\mathbf{Q}}{2}) \right)^2 + 4\Delta^2} \right], \tag{4.4}$$

where we conveniently choose the origin of the reciprocal space at the edge of the new BZ, i.e. the crossing point of the initial electron bands

$$\varepsilon_{1,2}(\mathbf{k}) \equiv \varepsilon \left(\mathbf{k} \pm \frac{\mathbf{Q}}{2} \right) = \hbar v_F \sqrt{\left(k_x \pm \frac{Q}{2} \right)^2 + k_y^2}, \tag{4.5}$$

in which the wave vector $\mathbf{Q} = (Q, 0)$ is taken along the k_x-axis. The finite Δ lifts the degeneracy in the band crossing area, leading to the reconstruction of the FS.

In Fig. 4.3 (a) we illustrate the CaC_6 Brillouin zone, showing the Fermi surface at energy ε_F after its reconstruction according to Eq. (4.4) and initial FS overlap (see Fig. 4.2), where $k_x \in (-Q/2, Q/2)$ with origin at the initial band-crossing point. We choose the coordinate system in which $\hat{\mathbf{k}}_x \parallel \mathbf{Q}$. The reconstruction region shows two peculiar points in the $E_{\pm}(\mathbf{k})$ spectrum, a hyperbolic point at energy $\varepsilon_H = \varepsilon_0 - \Delta$ in the lower band $E_{-}(\mathbf{k})$, and an elliptic point at energy $\varepsilon_E = \varepsilon_0 + \Delta$ in the upper band $E_{+}(\mathbf{k})$, where $\varepsilon_0 = \hbar v_F Q/2$ is the energy of the initial band-crossing point (see Fig 4.3 (b)). The contours are cross-sections at constant energy,

i.e. $E_{\pm}(\mathbf{k}) = \varepsilon_F$. The upper band FS (dashed yellow in panel (a)) appears for Fermi energy $\varepsilon_F > \varepsilon_E$.

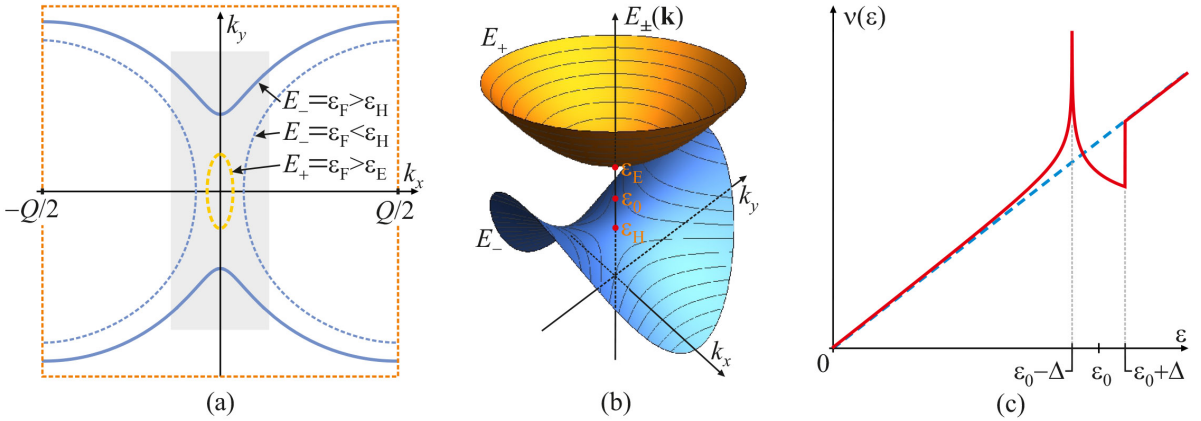

Figure 4.3: (a) The CaC_6 Brillouin zone, showing the Fermi surface at energy ε_F after the reconstruction and initial FS overlap (see Fig. 4.2 (b), (b) The reconstruction region (shaded in (a)) with two peculiar points in the $E_{\pm}(\mathbf{k})$ spectrum, a hyperbolic point at energy ε_H in the lower band $E_-(\mathbf{k})$, and an elliptic point at energy ε_E in the upper band. (c) The density of states (DOS) $\nu(\varepsilon)$ of the reconstructed system (red) exhibiting a pseudo-gap appearing between ε_H and ε_E, with a diverging van Hove singularity at ε_H. The dashed blue line is DOS of the non-reconstructed system, $\nu_0(\varepsilon) = 6\varepsilon/(\pi\hbar^2 v_F^2)$. Image from [67].

The most fundamental requirement in the reconstruction process of the Fermi surface is the conservation of the number of electrons, i.e.

$$N_0(\varepsilon_{F0}) = N(\varepsilon_F), \tag{4.6}$$

where ε_{F0}, ε_F are the Fermi energies, and $N_0(\varepsilon)$, $N(\varepsilon)$ are numbers of electrons of the 2D CaC_6 system before and after the reconstruction, respectively. The number of electrons is determined by the area of the corresponding (reconstructed or non-reconstructed) Fermi surface $S(\varepsilon)$, i.e. $N(\varepsilon) \sim S(\varepsilon)/(2\pi)^2$. Taken per unit area in the real space ($A = 1$) and assuming the 2-fold spin degeneracy as well as 6-fold FS degeneracy in the Γ-point of the CaC_6 BZ (Fig. 4.2 (a)), they are

$$\begin{aligned} N_0(\varepsilon) =& 3\varepsilon^2/(\pi\hbar^2 v_F^2), \\ N(\varepsilon) =& \frac{12}{\pi^2} \sum_{l=\pm} \int_0^{\frac{Q}{2}} k_{y,l}(k_x;\varepsilon,Q,\Delta)\Theta\left[l\left(K_l(\varepsilon,Q,\Delta) - k_x\right)\right] \mathrm{d}k_x. \end{aligned} \tag{4.7}$$

Here, $k_{y\pm}(k_x;\varepsilon,Q,\Delta)$ should be obtained from Eq. (4.4) by setting

$$E_{\pm}(\mathbf{k}) = \varepsilon. \tag{4.8}$$

The Heaviside theta function $\Theta(...)$ in

$$K_l(\varepsilon,Q,\Delta) \equiv \tfrac{1}{v_F}\sqrt{(\varepsilon-\hbar v_F Q/2)^2-\Delta^2}\,\Theta[l(\varepsilon-\hbar v_F Q/2)-\Delta], \tag{4.9}$$

ensures the real domain of integration over k_x of the $l=\pm$ branch of $k_{y,l}$ depending on parameters ε, Q, Δ (see Fig. 4.3 (a)).

The density of states (DOS) $\nu(\varepsilon)$ of the reconstructed system is obtained numerically from Eq. (4.7), simply as $\nu(\varepsilon) = \partial N(\varepsilon)/\partial\varepsilon$, clearly exhibiting a pseudo-gap in the band-crossing region and with a diverging van Hove singularity at ε_H for a fixed Δ (see Fig. 4.3 (c)). The bottom band, $E_-(\mathbf{k})$, is filled for any Q, whereas the upper one, $E_+(\mathbf{k})$, is only filled for

$$Q < Q_E \equiv \frac{2(\varepsilon_F-\Delta)}{\hbar v_F} \tag{4.10}$$

which corresponds to energies $\varepsilon > \varepsilon_E$ (see Fig. 4.3 (b)).

The analytical properties of the dispersion (4.4) make it impossible to obtain $k_{y\pm}(k_x;\varepsilon,Q,\Delta)$ in a closed analytical form. We will employ a specially devised expansion technique to achieve analytical results, which we will describe in the following section 4.2.

4.2 Reconstructed band structure - expansion

We define the dimensionless variables

$$\kappa_{x,y} \equiv \frac{k_{x,y}}{Q/2}, \;\; \xi_{1,2} \equiv \frac{\varepsilon_{1,2}}{\varepsilon_0}, \;\; e_{\pm} \equiv \frac{E_{\pm}}{\varepsilon_0}, \;\; \delta \equiv \frac{\Delta}{\varepsilon_0}, \;\; e_{F0,F} \equiv \frac{\varepsilon_{F0,F}}{\varepsilon_0}, \tag{4.11}$$

where $\varepsilon_0 \equiv \hbar v_F Q/2$ is the energy scale, in which the above expressions read

$$\begin{aligned} \xi_{1,2}(\kappa) &= \sqrt{(\kappa_x \pm 1)^2 + \kappa_y^2}, \\ e_{\pm}(\kappa,\delta) &= \frac{1}{2}\left[\xi_1(\kappa) + \xi_2(\kappa) \pm \sqrt{\left(\xi_1(\kappa) - \xi_2(\kappa)\right)^2 + 4\delta^2}\right]. \end{aligned} \tag{4.12}$$

Since only the lower band $e_-(\kappa,\delta) \equiv e(\kappa,\delta)$ contribution takes part in the final result (will be shown later), for simplicity we present only the corresponding expressions further on. We divide the $\kappa_x \in (0,1)$ domain by an arbitrary κ_0 obeying only the condition $\delta \ll \kappa_0 \ll 1$, for the lower band contribution at the energy close to ε_0, and perform the Taylor expansion within each interval with respect to the small parameter characteristic for that particular interval.

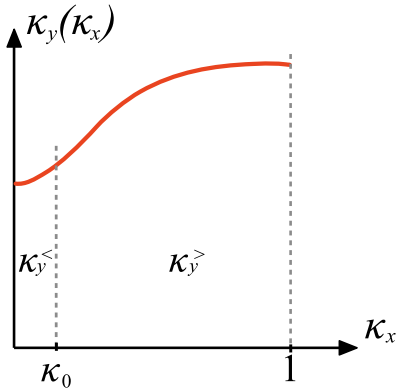

Figure 4.4: Schematic presentation of the division of the $\kappa_x \in (0,1)$ domain by κ_0 for which $\delta \ll \kappa_0 \ll 1$. $\kappa_y(\kappa_x)$ is approximated by $\kappa_y^<(\kappa_x)$ within $\kappa_x \in (0,\kappa_0)$ and by $\kappa_y^>(\kappa_x)$ within $\kappa_x \in (\kappa_0,1)$ subintervals. Image from [67].

4.2.1 $\kappa_y^<$ limit:

In this limit we use expansion in small $(\kappa_x, \kappa_y) \ll 1$, yielding

$$\xi_{1,2}(\kappa_x, \kappa_y) \approx 1 \pm \kappa_x + \frac{1}{2}\kappa_y^2 + \frac{1}{2}\kappa_x|\kappa|^2,$$
$$e_\pm(\vec{\kappa}, \delta) \approx 1 + \frac{1}{2}\kappa_y^2 \pm \sqrt{\kappa_x^2 + \delta^2}, \tag{4.13}$$

from which we finally obtain

$$\kappa_y^<(\kappa_x, e, \delta) \approx \sqrt{2}\sqrt{e - 1 + \sqrt{\kappa_x^2 + \delta^2}}. \tag{4.14}$$

4.2.2 $\kappa_y^>$ limit:

In this limit we use expansion in small $\delta \ll (\kappa_x, \kappa_y)$, yielding

$$\kappa_y^>(\kappa_x; e, \delta) = \sqrt{e^2 - (\kappa_x - 1)^2} + \frac{e^2 + e\sqrt{e^2 + 4\kappa_x}}{4\kappa_x\sqrt{e^2 - (\kappa_x - 1)^2}}\delta^2 + ...,$$

for which, after one more expansion in the additional small parameter of the order of δ, i.e.

$$\Delta e \equiv e - 1 \ll 1, \tag{4.15}$$

we get

$$\kappa_y^>(\kappa_x; e, \delta) = \sqrt{e^2 - (\kappa_x - 1)^2} + \frac{1 + \sqrt{1 + 4\kappa_x}}{4\kappa_x^2\sqrt{2 - \kappa_x}}\delta^2 +$$
$$+ \left(\frac{1 + \frac{1+2\kappa_x}{\sqrt{1+4\kappa_x}}}{2\kappa_x^2\sqrt{2 - \kappa_x^2}} - \frac{1 + \sqrt{1 + 4\kappa_x}}{4\kappa_x(2\kappa_x - \kappa_x^2)^{3/2}} \right) \Delta e\delta^2 + ...,$$

and, keeping accuracy up to $\sim \delta^2$ (which is later shown to be sufficient), we finally obtain

$$\kappa_y^>(\kappa_x; e, \delta) \approx \sqrt{e^2 - (\kappa_x - 1)^2} + \frac{1 + \sqrt{1 + 4\kappa_x}}{4\kappa_x^2\sqrt{2 - \kappa_x}}\delta^2. \tag{4.16}$$

4.3 Area of the reconstructed Fermi surface

We define the integral (area of the reconstructed Fermi surface)

$$I = \int_0^1 \kappa_y(\kappa_x; e, \delta) \mathrm{d}\kappa_x = I^< + I^>, \tag{4.17}$$

where

$$\begin{aligned} I^< &= \int_0^{\kappa_0} \kappa_y^<(\kappa_x; e, \delta) \mathrm{d}\kappa_x, \\ I^> &= \int_{\kappa_0}^1 \kappa_y^>(\kappa_x; e, \delta) \mathrm{d}\kappa_x. \end{aligned} \tag{4.18}$$

a) $I^<$:

$$\begin{aligned} I^< &= \int_0^{\kappa_0} \sqrt{2} \sqrt{\Delta e + \sqrt{\kappa_x^2 + \delta^2}}\, \mathrm{d}\kappa_x \\ &\left\{ \text{supst. } t \equiv \frac{\kappa_x}{\delta},\ a \equiv \frac{\Delta e}{\delta} > 0,\ r \equiv \frac{\kappa_0}{\delta} \gg 1 \right\} \\ &= \sqrt{2}\delta^{3/2} \int_0^r \sqrt{a + \sqrt{t^2+1}} \mathrm{d}t \end{aligned} \tag{4.19}$$

In the Eq. (4.19), the indefinite integral evaluates to

$$\begin{aligned} \tilde{I}^<(t) = \int \sqrt{a + \sqrt{t^2+1}} \mathrm{d}t &= \frac{2}{3} \frac{t(2a + \sqrt{t^2+1})}{\sqrt{a + \sqrt{t^2+1}}} + \\ &+ \frac{2}{3}\sqrt{a+1} \left[a\mathbb{E}\left(\arcsin \frac{\sqrt{a+1}}{\sqrt{a + \sqrt{t^2+1}}}, \frac{a-1}{a+1} \right) \right. \\ &\left. - \mathbb{F}\left(\arcsin \frac{\sqrt{a+1}}{\sqrt{a + \sqrt{t^2+1}}}, \frac{a-1}{a+1} \right) \right], \end{aligned} \tag{4.20}$$

where $\mathbb{F}(\phi, m)$ and $\mathbb{E}(\phi, m)$ are the incomplete elliptic integrals of the first and second kind, respectively. Inserting the limits of integration and performing the asymptotic expansion in

$r \gg 1$, we obtain

$$\begin{aligned}\tilde{I}^{<}(r)|_{r\gg 1} &\approx \frac{2}{3}r^{3/2} + a\sqrt{r} - \left(\frac{1}{2} - \frac{a^2}{4}\right)\frac{1}{\sqrt{r}} + ...,\\ \tilde{I}^{<}(0) &\approx \frac{2}{3}\sqrt{a+1}\left[a\mathbb{E}\left(\frac{\pi}{2}, \frac{a-1}{a+1}\right) - \mathbb{F}\left(\frac{\pi}{2}, \frac{a-1}{a+1}\right)\right]\\ &= \frac{2}{3}\sqrt{a+1}\left[a\mathbb{E}\left(\frac{a-1}{a+1}\right) - \mathbb{K}\left(\frac{a-1}{a+1}\right)\right], \end{aligned} \tag{4.21}$$

where $\mathbb{K}(\eta)$ and $\mathbb{E}(\eta)$ are the complete elliptic integrals of the first and second kind, respectively. Using the fact that $\eta \equiv (a-1)/(a+1) \ll 1$ is small, we expand the complete elliptic integrals

$$\begin{aligned}\mathbb{E}(\eta) &\simeq \frac{\pi}{2} - \frac{\pi}{8}\eta - \frac{3\pi}{128}\eta^2 - ...,\\ \mathbb{K}(\eta) &\simeq \frac{\pi}{2} + \frac{\pi}{8}\eta + \frac{9\pi}{128}\eta^2 + ..., \end{aligned} \tag{4.22}$$

which give

$$\begin{aligned}\tilde{I}^{<}(0) &= \frac{\pi}{4}\sqrt{a+1}\left[1 - \frac{1}{16}\frac{(a-1)(a+3)}{(a+1)^2}\right]\\ &\simeq \frac{\pi}{4}\sqrt{a+1}\,(a-1)\,, \end{aligned} \tag{4.23}$$

where we used $a = \Delta e/\delta$ and $(\Delta e - \delta)/\delta \ll 1$. Using the above, we finally obtain the integral (4.19), up to the leading terms,

$$\begin{aligned}I^{<} &\approx \sqrt{2}\delta^{3/2}\left[\frac{2}{3}r^{3/2} + a\sqrt{r} - \left(\frac{1}{2} - \frac{a^2}{4}\right)\frac{1}{\sqrt{r}} - \frac{\pi}{4}\sqrt{a+1}(a-1) + ...\right]\\ &= \frac{2\sqrt{2}}{3}\kappa_0^{3/2} + \sqrt{2}\Delta e\sqrt{\kappa_0} - \frac{\sqrt{2}}{2}\frac{\delta^2}{\sqrt{\kappa_0}} + \frac{\Delta e^2}{2\sqrt{2}}\frac{1}{\sqrt{\kappa_0}} - \sqrt{2}\frac{\pi}{4}\sqrt{\Delta e + \delta}(\Delta e - \delta) + ... \end{aligned} \tag{4.24}$$

b) $I^{>}$: We express the integral as

$$I^{>} = I_0^{>} + I_2^{>}, \tag{4.25}$$

where

$$I_0^{>} = \int_{\kappa_0}^{1} \sqrt{e^2 + (\kappa_x - 1)^2}\mathrm{d}\kappa_x,$$
$$I_2^{>} = \delta^2 \int_{\kappa_0}^{1} \frac{1 + \sqrt{1 + 4\kappa_x}}{4\kappa_x^2\sqrt{2 - \kappa_x}}\mathrm{d}\kappa_x. \tag{4.26}$$

To evaluate the integrals (4.26), first we take the corresponding indefinite integrals. The first integral is

$$\begin{aligned}\tilde{I_0}^{>}(\kappa_x) &= \int \sqrt{e^2 - (\kappa_x - 1)^2}\mathrm{d}\kappa_x \\ &= \frac{1}{2}(\kappa_x - 1)\sqrt{e^2 - (\kappa_x - 1)^2} + \frac{1}{2}e^2 \arctan\frac{\kappa_x - 1}{\sqrt{e^2 - (\kappa_x - 1)^2}},\end{aligned} \tag{4.27}$$

in which we insert limits of integration and expand in terms of $\kappa_0 \ll 1$,

$$\begin{aligned}\tilde{I_0}^{>}(1) &= 0, \\ \tilde{I_0}^{>}(\kappa_0)|_{\kappa_0 \ll 1} &\approx -\frac{\pi}{4}e^2 + \frac{\Delta e^2}{2\sqrt{2}\sqrt{\kappa_0}} - \sqrt{2}\sqrt{\kappa_0}\Delta e - \\ &\quad - \frac{5}{8\sqrt{2}}\sqrt{\kappa_0}\Delta e^2 + \frac{2\sqrt{2}}{3}\kappa_0^{3/2} + \frac{\sqrt{2}}{12}\Delta e\kappa_0^{3/2} + \ldots\end{aligned} \tag{4.28}$$

which finally yields the value of the first integral (4.26) up to the leading terms

$$\begin{aligned}I_0^{>} &\approx \frac{\pi}{4}e^2 - \frac{\Delta e^2}{2\sqrt{2}\sqrt{\kappa_0}} - \sqrt{2}\sqrt{\kappa_0}\Delta e - \\ &\quad - \frac{5}{8\sqrt{2}}\sqrt{\kappa_0}\Delta e^2 - \frac{2\sqrt{2}}{3}\kappa_0^{3/2} - \frac{1}{6\sqrt{2}}\kappa_0^{3/2}\Delta e + \ldots\end{aligned} \tag{4.29}$$

The second integral is

$$\begin{aligned}\tilde{I_2}^{>}(\kappa_x) &= \int \frac{1 + \sqrt{1 + 4\kappa_x}}{4\kappa_x^2\sqrt{2 - \kappa_x}}\mathrm{d}\kappa_x = \\ &= -\frac{1}{4}\frac{\sqrt{2 - \kappa_x}(1 + \sqrt{1 + 4\kappa_x})}{\sqrt{\kappa_x}} + \\ &+ \frac{3}{4}\left[\mathbb{E}\left(\arcsin\sqrt{1 - \frac{\kappa_x}{2}}, \frac{8}{9}\right) - \mathbb{F}\left(\arcsin\sqrt{1 - \frac{\kappa_x}{2}}, \frac{8}{9}\right)\right],\end{aligned} \tag{4.30}$$

in which we insert limits of integration and expand in terms of $\kappa_0 \ll 1$,

$$\begin{aligned}\tilde{I_2}^{>}(1) &= -\frac{1}{4}\left[1+\sqrt{5}+3\left(\mathbb{F}\left(\frac{\pi}{4},\frac{8}{9}\right)-\mathbb{E}\left(\frac{\pi}{4},\frac{8}{9}\right)\right)\right],\\ \tilde{I_2}^{>}(\kappa_0)|_{\kappa_0\ll 1} &\approx \frac{3}{4}\left(\mathbb{E}\left(\frac{8}{9}\right)-\mathbb{K}\left(\frac{8}{9}\right)\right)-\frac{1}{\sqrt{2}\sqrt{\kappa_0}}+\frac{5}{4\sqrt{2}}\sqrt{\kappa_0}-\\ &\quad-\frac{7}{32\sqrt{2}}\kappa_0^{3/2}+...,\end{aligned} \tag{4.31}$$

which finally yields the value of the second integral (4.26) up to the leading terms

$$\begin{aligned}I_2^{>} = \delta^2\Bigg[&-\frac{1+\sqrt{5}}{4}-\frac{3}{4}\left(\mathbb{F}\left(\frac{\pi}{4},\frac{8}{9}\right)-\mathbb{E}\left(\frac{\pi}{4},\frac{8}{9}\right)+\mathbb{E}\left(\frac{8}{9}\right)-\mathbb{K}\left(\frac{8}{9}\right)\right)+\\ &+\frac{1}{\sqrt{2}\sqrt{\kappa_0}}-\frac{5}{4\sqrt{2}}\sqrt{\kappa_0}+\frac{7}{32\sqrt{2}}\kappa_0^{3/2}+...\Bigg].\end{aligned} \tag{4.32}$$

Collecting all the terms (4.18), we obtain the integral (4.17)

$$\begin{aligned}I &\approx I^{<}+I_0^{>}+I_2^{>}\\ &\approx \frac{\pi}{4}e^2-\sqrt{2}\frac{\pi}{4}\sqrt{\Delta e+\delta}\,(\Delta e-\delta)+\frac{1}{4}\alpha\delta^2,\end{aligned} \tag{4.33}$$

where

$$\begin{aligned}\alpha &= 3\left(\mathbb{E}\left(\frac{\pi}{4},\frac{8}{9}\right)-\mathbb{F}\left(\frac{\pi}{4},\frac{8}{9}\right)-\mathbb{E}\left(\frac{8}{9}\right)+\mathbb{K}\left(\frac{8}{9}\right)\right)-1-\sqrt{5}\\ &\approx 0.5568.\end{aligned} \tag{4.34}$$

It should be noted that the final result does not include contributions with the arbitrary parameter κ_0, which cancel each other. Here we explicitly demonstrate it for the terms of desired accuracy (i.e. $\sim 1/\sqrt{\kappa_0}$, $\sim \Delta e\sqrt{\kappa_0}$, $\sim {\kappa_0}^{3/2}$), neglecting the remaining terms exceeding it (i.e. $\sim \sqrt{\kappa_0}\Delta e^2$, $\sim {\kappa_0}^{3/2}\Delta e$, $\sim \kappa_0\delta^2$, $\sim {\kappa_0}^{3/2}\delta^2$, ...). That also serves as a test of the controlled expansion of the same function across parameter regimes.

4.4 Condensation energy

The condensation energy (per unit area) of the CDW state is the difference between the initial (band) energy

$$E_0 = \int_0^{\varepsilon_{F0}} \nu_0(\varepsilon)\varepsilon d\varepsilon = \frac{2\varepsilon_{F0}^3}{\pi\hbar^2 v_F^2}, \tag{4.35}$$

and the final energy of the system, which includes contributions from the reconstructed band and the elastic deformation energy of the lattice

$$\frac{\nu_0(\varepsilon_{F0})\Delta^2}{2\lambda}, \tag{4.36}$$

where $\nu_0(\varepsilon)$ is the density of states of system before the reconstruction at energy ε. The reconstructed band energy is determined by

$$N(\varepsilon) = \sum_{\mathbf{k},s,Z_{\mathrm{CaC_6}}} 1 = \frac{12}{(2\pi)^2}\int \mathrm{d}^2k = \frac{3}{\pi^2}S(\varepsilon) \tag{4.37}$$

$$E_{band}(\varepsilon) = \int_0^{\varepsilon} \frac{\mathrm{d}N}{\mathrm{d}\varepsilon'}\varepsilon' \mathrm{d}\varepsilon' = \varepsilon N(\varepsilon) - \frac{3}{\pi^2}\int_0^{\varepsilon} S(\varepsilon')\mathrm{d}\varepsilon', \tag{4.38}$$

where $\mathbf{k}$ is the 2D electron momentum (the summation and integration in (4.37) are taken over the states $\mathbf{k}$ up to the energy ε), $s = 2$ and $Z_{\mathrm{CaC_6}} = 6$ are the spin and CaC_6 degeneracies, and $S(\varepsilon)$ is the 2D equienergy surface (i.e. the Fermi surface for $\varepsilon = \varepsilon_F$). The condensation energy normalised to E_0 is

$$\frac{E_{CDW}}{E_0} = 1 - \frac{3}{2}\left(\frac{Q}{2k_{F0}}\right)^3 \sum_{l=\pm} 4\int_0^1 \mathrm{d}\kappa_x \int_0^{\kappa_{y,l}(\kappa_x;e_F,\delta)} e_l(\kappa_x,\kappa_y,\delta)\mathrm{d}\kappa_y - \frac{3}{2\lambda}\left(\frac{\Delta}{\varepsilon_{F0}}\right)^2, \tag{4.39}$$

where

$$\lambda \equiv \frac{\nu_0(\varepsilon_{F0})g^2}{\hbar\omega_{\mathbf{Q}}} \tag{4.40}$$

represents the dimensionless electron-phonon coupling. Maximising the condensation energy with respect to ε_F, Q, and Δ results in an optimal positive condensation energy that stabilises the CDW. The optimisation approach considers the Q-dependence of the coupling constant and order parameter to be slow enough to be neglected. The optimisation with respect to Q involves

only the electron band contribution to the condensation energy, for a fixed Δ that has yet to be determined. Q decreases, causing the occupied parts of the original electron bands $\varepsilon(\mathbf{k}+\mathbf{Q}/2)$ and $\varepsilon(\mathbf{k}-\mathbf{Q}/2)$ to overlap and reconstruct the Fermi surface. The formation of a hyperbolic peculiar point in the lower reconstructed band, at energy ε_H now below the initial Fermi energy $\varepsilon_{F0} > \varepsilon_H$, significantly increases the number of states below ε_{F0} due to the formation of the van Hove singularity at ε_H (also evident as the increase of the FS area - see Fig. 4.3). As a result, the Fermi energy of the reconstructed system should in principle decrease, lowering the total energy of the reconstructed band. The next step in our calculation is to optimise the reconstructed band energy with respect to ε_{F0}, ε_F and Q.

4.5 Optimisation of the reconstructed band energy with respect to ε_{F0}, ε_F and Q

We start with general expressions for the number of particles (electrons) $N(\varepsilon)$ and the band energy $E_{band}(\varepsilon)$ at energy ε,

$$\begin{aligned} N(\varepsilon) &= \int_0^{\varepsilon} \nu(\varepsilon')\mathrm{d}\varepsilon' \\ E_{band}(\varepsilon) &= \int_o^{\varepsilon} \nu(\varepsilon')\varepsilon'\mathrm{d}\varepsilon', \end{aligned} \tag{4.41}$$

in terms of the density of states $\nu(\varepsilon)$. The band contribution to the condensation energy is defined as

$$E_{band}^{(c)} \equiv E_0 - E_{band}, \tag{4.42}$$

where E_0 is the initial band energy, and E_{band} is the reconstructed band energy, defined by the expressions (4.35) (4.38). Using the expressions above it reads

$$E_{band}^{(c)} = \varepsilon_{F0}N_0(\varepsilon_{F0}) - \varepsilon_F N_r(\varepsilon_F) + \frac{3}{\pi^2}\left[\int_0^{\varepsilon_F} S_r(\varepsilon)\mathrm{d}\varepsilon - \int_0^{\varepsilon_{F0}} S_0(\varepsilon)\mathrm{d}\varepsilon,\right], \tag{4.43}$$

where S_0 and S_r are the initial and reconstructed Fermi surfaces, N_0 and N_r are the numbers of electrons in the initial and reconstructed system, and ε_{F0} and ε_F are the Fermi energies of the initial and reconstructed system. S_r and ε_F are dependent on Q and Δ, but we keep Δ fixed in this case (it is optimised later in the total condensation energy). $E_{band}^{(c)}$ must be optimised (maximised) with respect to ε_F and Q, while preserving the number of particles in the reconstruction process. In that regard, we define the Lagrange function

$$\mathcal{L} = E_{band}^{(c)} - \mu\Delta N, \tag{4.44}$$

where μ is the Lagrange multiplier and $\Delta N = N_r(\varepsilon_F) - N_0(\varepsilon_{F0})$. Using the standard optimisation process, we get the three following conditions:

$$\begin{aligned} 1.) \quad & 0 = \frac{\partial \mathcal{L}}{\partial \varepsilon_{F0}} = \nu_0(\varepsilon_{F0})(\varepsilon_{F0} - \mu) \\ 2.) \quad & 0 = \frac{\partial \mathcal{L}}{\partial \varepsilon_F} = \nu(\varepsilon_F)(\varepsilon_{F0} - \varepsilon_F) \\ 3.) \quad & 0 = \frac{\partial \mathcal{L}}{\partial Q} = \int_0^{\varepsilon_F} \frac{\partial S_r(\varepsilon, Q)}{\partial Q} \mathrm{d}\varepsilon. \end{aligned} \tag{4.45}$$

The system (4.45) shows that the optimal value of the Fermi energy of the reconstructed system is equal to the initial one, i.e. $\varepsilon_F = \varepsilon_{F0}$ as long as there is $Q = Q_{opt}$ for which

$$\left. \frac{\partial S_r(Q)}{\partial Q} \right|_{Q=Q_{opt}} = 0 \tag{4.46}$$

i.e. $S_r(Q)$ has a maximum (which is checked by taking the second derivative). This occurs only when the maximum is attained in the lower band *before* reaching the upper band. Fig. 4.5 depicts the Fermi surface reconstruction process as Q varies. For clarity, the process is illustrated schematically before calculation. Taking only the lower band (red contour) into account, it is clear that as Q is reduced, the enclosed area $S(Q)$ first remains constant, then begins to increase due to the finite gap parameter, and finally begins to decrease due to the fact that the size of the Brillouin zone $(-Q/2, Q/2)$ is reduced by the reduction of Q. This competition provides a maximum of area S_r^{max} at $Q = Q_{opt}$, as shown schematically in Fig. 4.6.

The scenario given above is appropriate as long as the maximum $S_r^{max}(Q_{opt})$ appears, by reducing Q, *before* the formation of the second (upper) band. If the second band is formed before reaching Q_{opt}, i.e. when $Q > Q_{opt}$, then $E_{band}^{(c)}$ instantly begins to decrease, establishing a maximum at that value of Q. The reconstruction process continues by reducing Q until $\varepsilon_F = \varepsilon_{F0}$, where $S_r(\varepsilon_F)$ is maximum, *unless* the upper band is achieved first. In this scenario, the reconstruction ends at $Q = Q_{opt}$, when the upper band is formed and $\varepsilon_F < \varepsilon_{F0}$.
Using the conservation of the number of particles

$$N_0(\varepsilon_{F0}) = N_r(\varepsilon_F), \tag{4.47}$$

i.e. the surface $S_0(\varepsilon_{F0}) = S_r(\varepsilon_F)$ in dimensionless variables (4.11), and integral (4.33), we get

$$\pi e_{F0}^2 = 4I, \tag{4.48}$$

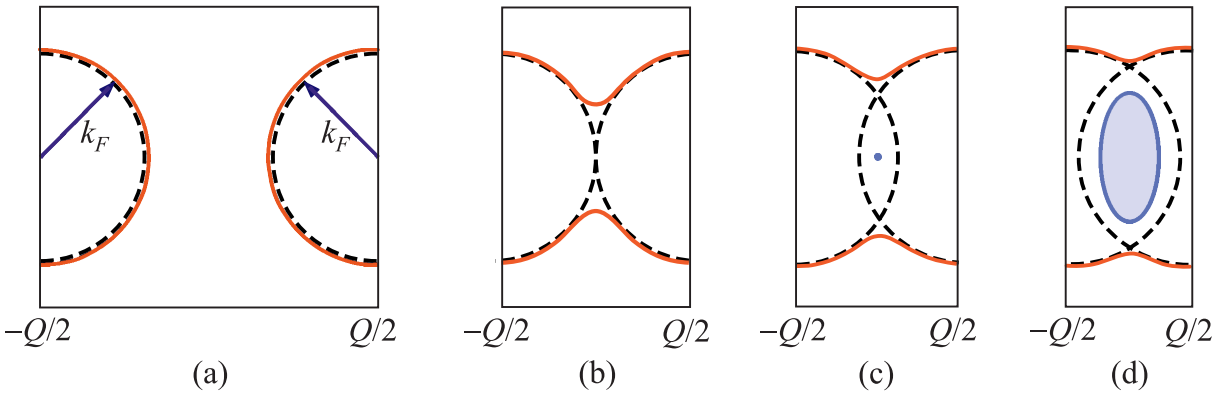

Figure 4.5: Schematic presentation of the 2D Fermi surface reconstruction process at the same Fermi energy (characterised by the Fermi wave number k_F) while Q is varied. Reduction of Q controls the overlap of the initial Fermi surfaces (dashed curve) and size of the new Brillouin zone. The full red curve represents the contour of the reconstructed Fermi surface as Q is reduced, i.e. (a) $Q > 2k_F$, (b) $Q = 2k_F$, (c) $Q < 2k_F$, (d) $Q < 2k_F$ and the second (upper) band is formed (blue).

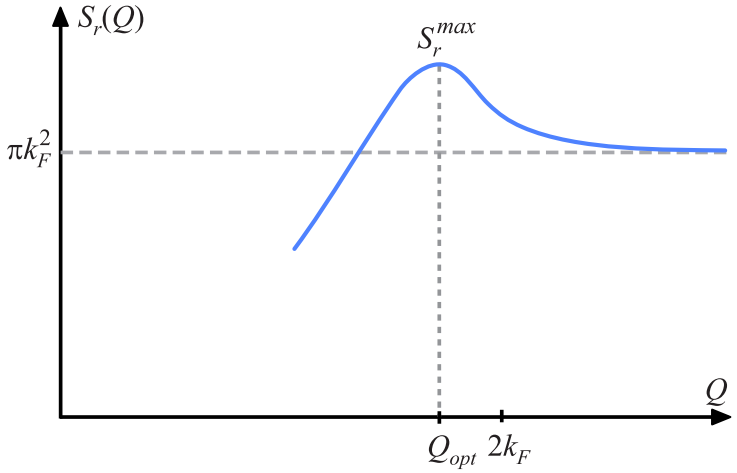

Figure 4.6: Schematic presentation of the change of area of the reconstructed Fermi surface $S_r(Q)$, as Q is varied, of the lower band (only) - see also Fig. 4.5. For Q significantly larger than $2k_F$, gap parameter has no contribution, yielding the $S_r(Q)$ being equal to πk_F^2. As Q is reduced to $Q \sim 2k_F$, lifting of degeneracy takes place by the (pseudo)gap opening and $S_r(Q)$ increases. By further reduction of Q, $S_r(Q)$ finally starts to decrease because size of the Brillouin zone $(-Q/2, Q/2)$ is decreased by reduction of Q. Therefore, $S_r(Q)$ has a maximum S_r^{max} at $Q = Q_{opt}$.

i.e.

$$\pi e_{F0}^2 = \pi e_F^2 - \sqrt{2}\pi\sqrt{\Delta e_F + \delta}\,(\Delta e_F - \delta) + \alpha\delta^2, \tag{4.49}$$

where $\Delta e_F = e_F - 1$, which, in the original (non-scaled) variables, reads

$$\varepsilon_F^2 - \varepsilon_{F0}^2 = \sqrt{2}\sqrt{\hbar v_F \frac{Q_{opt}}{2}}\sqrt{\varepsilon_F - \hbar v_F \frac{Q_{opt}}{2} + \Delta}\left(\varepsilon_F - \hbar v_F \frac{Q_{opt}}{2} - \Delta\right) - \frac{\alpha}{\pi}\Delta^2. \tag{4.50}$$

The constraint (4.50) illustrates that at $\varepsilon_F = \varepsilon_{F0}$, it provides $Q < Q_E$, indicating that the top band would be filled. To carry out the proper optimisation we apply the new, natural scaling that normalizes to the initial Fermi energy

$$\varepsilon_{F0} = \hbar v_F k_{F0} \tag{4.51}$$

i.e.

$$\begin{aligned} \tilde{e} &= \frac{\varepsilon_F}{\varepsilon_{F0}} \\ q_{opt} &= \frac{Q_{opt}}{2k_{F0}} \\ \tilde{\delta} &= \frac{\Delta}{\varepsilon_{F0}}, \end{aligned} \tag{4.52}$$

$\tilde{e}_{F0} \equiv 1$, and write the expression (4.50) in the form

$$\tilde{e}_F^2 - \tilde{e}_{F0}^2 = \sqrt{2}\sqrt{q_{opt}}\sqrt{\tilde{e}_F - q_{opt} + \tilde{\delta}}\left(\tilde{e}_F - q_{opt} - \tilde{\delta}\right) - \frac{\alpha}{\pi}\tilde{\delta}^2. \tag{4.53}$$

Using Eq. (4.53), we determine whether $\tilde{e}_F = \tilde{e}_{F0}$ occurs before the upper band is reached. Using perturbation theory for $q_{opt} = q_{opt}^{(0)} + q_{opt}^{(1)}$, $q_{opt}^{(1)} \ll 1$, we get $q_{opt} \approx 1 - \tilde{\delta} - \frac{\alpha}{2\pi}\tilde{\delta}^{3/2}$, which means that the overlap of the initial FS is larger than the critical $q_{opt} = 1 - \tilde{\delta}$ for which the upper band is reached. This implies that the reduction of q ends at $q_{opt} = 1 - \tilde{\delta}$. For that value, using perturbation theory in $\tilde{e}_F = \tilde{e}_F^{(0)} + \tilde{e}_F^{(1)}$, $\tilde{e}_F^{(1)} \ll 1$, we find $\tilde{e}_F \approx 1 - \frac{\alpha}{2\pi}\tilde{\delta}^2$. This yields the optimal wave vector of the CDW and the Fermi energy of the reconstructed system for a fixed Δ, i.e.

$$\begin{aligned} Q_{opt} &= 2k_{F0}\left[1 - \left(\frac{\Delta}{\varepsilon_{F0}}\right)\right], \\ \varepsilon_F &= \varepsilon_{F0}\left[1 - \frac{\alpha}{2\pi}\left(\frac{\Delta}{\varepsilon_{F0}}\right)^2\right]. \end{aligned} \tag{4.54}$$

This value of the reconstruction vector is preferably commensurate with the reciprocal lattice constant of the CaC_6 structure in the corresponding direction (see Fig. 4.2), that is, $b^* = mQ_{opt}$, where $m \in \mathbb{N}$. The incommensurability implications will be discussed in Chapter 5.

4.6 Optimisation of the total condensation energy with respect to Δ

4.6.1 The reconstructed band energy

We calculate the band energy of the reconstructed system, first for an arbitrary Q and Δ, as

$$E_{band}^{(r)} = sZ_{\mathrm{CaC_6}} \frac{4}{(2\pi)^2} \int_0^{Q/2} dk_x \int_0^{k_y^{(F)}(k_x,\varepsilon_F,Q,\Delta)} \mathrm{d}k_y \varepsilon(k_x,k_y,Q,\Delta), \tag{4.55}$$

where $s = 2$ and $Z_{\mathrm{CaC_6}} = 6$ are the spin and $\mathrm{CaC_6}$ degeneracy respectively, $k_y^{(F)}(k_x,\varepsilon_F,Q,\Delta) = k_{y-}(k_x,\varepsilon,Q,\Delta)|_{\varepsilon=\varepsilon_F}$ and $\varepsilon(k_x,k_y,Q,\Delta) = \varepsilon_-(k_x,k_y,Q,\Delta)$ from the Eq. (4.4). The scaling (4.11) yields

$$E_{band}^{(r)} = \frac{3}{\pi^2}\hbar v_F \left(\frac{Q}{2}\right)^3 4 \int_0^1 d\kappa_x \int_0^{\kappa_y^{(F)}(\kappa_x,e_F,\delta)} \mathrm{d}\kappa_y e(\kappa_x,\kappa_y,\delta) \tag{4.56}$$

where $e(\kappa_x,\kappa_y,\delta) = e_-(\kappa_x,\kappa_y,\delta)$ from Eq. (4.12). Using the ideal value of the wave vector determined in the previous section, $Q = Q_{opt} = 2k_{F0}(1-\tilde{\delta})$, where $\tilde{\delta} \equiv \Delta/\varepsilon_{F0}$, we get

$$E_{band}^{(r)} = \frac{3}{\pi^2}\hbar v_F k_{F0}^3 q_{opt}^3 J, \tag{4.57}$$

where $q_{opt} \equiv 1-\tilde{\delta}$ and

$$J \equiv 4 \int_0^1 \mathrm{d}\kappa_x \int_0^{\kappa_y^{(F)}(\kappa_x,e_F,\delta)} e(\kappa_x,\kappa_y,\delta)\mathrm{d}\kappa_y. \tag{4.58}$$

To calculate the integral J as a function of δ, we develop the following procedure:

$$\frac{\mathrm{d}J}{\mathrm{d}\delta} = \frac{\partial J}{\partial e_F}\frac{\partial e_F}{\partial \delta} + \frac{\partial J}{\partial \delta}. \tag{4.59}$$

Previously, Eq. (4.54) we found that $\varepsilon_F = \varepsilon_{F0}\left(1-\frac{\alpha}{2\pi}\tilde{\delta}^2\right)$, i.e. $e_F = e_{F0}\left(1-\frac{\alpha}{2\pi}\tilde{\delta}^2\right)$, from where we can write $\partial/\partial e_F = \left(1-\frac{\alpha}{2\pi}\tilde{\delta}^2\right)^{-1}\partial/\partial e_{F0}$, i.e. we can change the derivative for a

more convenient one. The terms of the expression (4.59) are computed below. First, we find

$$\begin{aligned}\frac{\partial J}{\partial e_{F0}} &= 4\int_0^1 \mathrm{d}\kappa_x \left(\frac{\partial \kappa_y^{(F)}}{\partial e_{F0}}\right) e(\kappa_x, \kappa_y^{(F)}, \delta) \\ &= e_F \frac{\partial}{\partial e_{F0}} 4\int_0^1 \mathrm{d}\kappa_x, \kappa_y^{(F)}(\kappa_x, e_F, \delta) \\ &= e_F \frac{\partial}{\partial e_{F0}} S_r(e_F, \delta),\end{aligned} \tag{4.60}$$

for which, using the conservation of the number of particles $S_r(e_F,\delta) = S_0(e_{F0})$, where $S_0(e_{F0}) = \pi e_{F0}^2$, after taking the derivative, we finally get

$$\frac{\partial J}{\partial e_{F0}} = 2\pi e_F e_{F0}. \tag{4.61}$$

Using this result (after modifying derivatives), we calculate the first term in Eq. (4.59)

$$\begin{aligned}\frac{\partial J}{\partial e_F}\frac{\partial e_F}{\partial \delta} &= 2\pi e_F e_{F0}\frac{\partial e_{F0}}{\partial \delta} \\ &= 2\pi\left(1-\frac{\alpha}{2\pi}\tilde{\delta}^2\right) e_{F0}^2 \frac{\partial e_{F0}}{\partial \delta} \\ &= \frac{2\pi}{3}\left(1-\frac{\alpha}{2\pi}\tilde{\delta}^2\right)\frac{\partial e_{F0}^3}{\partial \delta}.\end{aligned} \tag{4.62}$$

The second term in Eq. (4.59) is

$$\begin{aligned}\frac{\partial J}{\partial \delta} &= 4\int_0^1 \mathrm{d}\kappa_x \left(\frac{\partial \kappa_y^{(F)}}{\partial \delta}\right) e(\kappa_x, \kappa_y^{(F)}, \delta) + 4\int_0^1 \mathrm{d}\kappa_x \int_0^{\kappa_y^{(F)}(\kappa_x, e_F, \delta)} \mathrm{d}\kappa_y \frac{\partial}{\partial \delta} e(\kappa_x, \kappa_y, \delta) \\ &= e_F \frac{\partial}{\partial \delta} S_r(e_F, \delta) + 4\int_0^1 \mathrm{d}\kappa_x \int_0^{\kappa_y^{(F)}(\kappa_x, e_F, \delta)} \mathrm{d}\kappa_y \frac{-2\delta}{\sqrt{\left(\xi_1(\vec{\kappa}) - \xi_2(\vec{\kappa})\right)^2 + 4\delta^2}}.\end{aligned} \tag{4.63}$$

Using the conservation of particle number, $S_r(e_F,\delta) = S_0(e_{F0}) = const$, we evaluate the first term of the expression above to zero. The second term expands in powers of δ, and a linear term $\sim \delta$ appears from δ in the numerator of the formula (setting it to zero elsewhere). The additional contributions (from the denominator and the boundaries of the integral) are of higher

order, $\sim \delta^3$. The linear term is satisfactory for the final result, therefore we take

$$\begin{aligned}\frac{\partial J}{\partial \delta} &\approx \lim_{\delta\to 0}\left[4\int_0^1 d\kappa_x \int_0^{\kappa_y^{(F)}(\kappa_x,e_F,\delta)} \frac{1}{\sqrt{\left(\xi_1(\vec{\kappa})-\xi_2(\vec{\kappa})\right)^2+4\delta^2}}\right](-2\delta)\\ &= -2\beta\delta \end{aligned} \tag{4.64}$$

where

$$\begin{aligned}\beta &= 4\int_0^1 d\kappa_x \int_0^{\sqrt{2\kappa_x-\kappa_x^2}} d\kappa_y \frac{1}{\sqrt{(\kappa_x+1)^2+\kappa_y^2}-\sqrt{(\kappa_x-1)^2+\kappa_y^2}}\\ &= \frac{1}{2}\int_0^1 \frac{d\kappa_x}{\kappa_x}\left[\sqrt{2\kappa_x-\kappa_x^2}\left(1+\sqrt{1+4\kappa_x}\right)+\right.\\ &\left.+(1+\kappa_x)^2\,\mathrm{arcsinh}\,\frac{\sqrt{2\kappa_x-\kappa_x^2}}{1+\kappa_x}+(1-\kappa_x)^2\,\mathrm{arcsinh}\,\frac{\sqrt{2\kappa_x-\kappa_x^2}}{1-\kappa_x}\right]\\ &= 5.57802. \end{aligned} \tag{4.65}$$

Collecting the terms above, we assemble Eq. (4.59)

$$\frac{dJ}{d\delta} \approx \frac{2\pi}{3}\left(1-\frac{\alpha}{2\pi}\tilde{\delta}^2\right)\frac{de_{F0}^3}{d\delta} - 2\beta\delta \tag{4.66}$$

from which we calculate J from Eq. (4.58) simply by integrating with respect to δ, i.e.

$$J(\delta) \approx \frac{2\pi}{3}\left(1-\frac{\alpha}{2\pi}\tilde{\delta}^2\right)e_{F0}^3 - \beta\delta^2. \tag{4.67}$$

The energy of the reconstructed band (4.57) may now be determined using $e_{F0} = \varepsilon_{F0}/\left(\hbar v_F Q_{opt}/2\right) = q_{opt}^{-1}$,

$$\begin{aligned}E_{band}^{(r)} &= \frac{3}{\pi^2}\hbar v_F k_{F0}^3 q_{opt}^3\left[\frac{2\pi}{3}\left(1-\frac{\alpha}{2\pi}\tilde{\delta}^2\right)q_{opt}^{-3} - \beta\frac{\tilde{\delta}^2}{q_{opt}^2}\right]\\ &= E_0 - \frac{3}{2\pi}E_0\left[\left(\frac{\alpha}{3}+\beta\right)\left(\frac{\Delta}{\varepsilon_{F0}}\right)^2 - \beta\left(\frac{\Delta}{\varepsilon_{F0}}\right)^3\right], \end{aligned} \tag{4.68}$$

where $E_0 = 2\hbar v_F k_{F0}^3/\pi = 2\varepsilon_{F0}^3/(\pi\hbar^2 v_F^2)$ is the energy of the initial, unreconstructed band as shown in Eq. (4.35), and the constants α and β are defined in the expressions (4.34) and (4.65), respectively.

4.6.2 "Elastic" energy of the deformed Ca lattice

The last term in the mean-field Hamiltonian (taken per unit area), usually called "the elastic energy", describes the gain in the energy of the mechanically deformed crystal lattice due to the established CDW ground state coupled to the phonon mode with wave vector $\mathbf{Q}$ and frequency $\omega_{\mathbf{Q}}$. It reads

$$E_{latt} = \frac{\hbar\omega_{\mathbf{Q}}}{2g^2}\Delta^2 = \nu_0\frac{\Delta^2}{2\lambda} = \frac{3}{2}E_0\frac{1}{\lambda}\left(\frac{\Delta}{\varepsilon_{F0}}\right)^2, \tag{4.69}$$

where $\lambda \equiv \nu_0 g^2/(\hbar\omega_{\mathbf{Q}})$ is the dimensionless electron-phonon coupling constant for the phonon mode $\omega_{\mathbf{Q}}$ and ν_0 is the initial DOS at the Fermi energy. Here we used $\nu_0 = 2\varepsilon_{F0}/(\pi\hbar^2 v_F^2)$ and $E_0 = 2\varepsilon_{F0}^3/(\pi\hbar^2 v_F^2)$ to relate the last two expressions in Eq. (4.69).

4.6.3 The condensation energy of the CDW state

The condensation energy of the CDW ground state is defined as the difference of the initial and final energy of the system

$$E_{CDW} = E_0 - \left(E_{band}^{(r)} + E_{latt}\right).$$

Using expressions (4.68) and (4.69), we get

$$\frac{E_{CDW}}{E_0} = \frac{3}{2}\left[\frac{1}{\lambda_c} - \frac{1}{\lambda}\right]\left(\frac{\Delta}{\varepsilon_{F0}}\right)^2 - \frac{3\beta}{2\pi}\left(\frac{\Delta}{\varepsilon_{F0}}\right)^3, \tag{4.70}$$

where

$$\lambda_c \equiv \pi\left[\frac{\alpha}{3} + \beta\right]^{-1} \simeq 0.54, \tag{4.71}$$

and $\alpha \approx 0.5568$ and $\beta \approx 5.578$ are defined in expressions (4.34) and (4.65), respectively. λ_c appears to be the critical value of the electron-phonon coupling constant, determined by the reconstructed electron band. Above this value, the maximisation of condensation energy (4.70) with respect to the order parameter Δ, yields its positive maximum. Thus, for electron-phonon coupling $\lambda > \lambda_c$, the zero-temperature CDW is stabilised by the order parameter

$$\Delta = \frac{2\pi}{3\beta}\left[\frac{1}{\lambda_c} - \frac{1}{\lambda}\right]\varepsilon_{F0}, \tag{4.72}$$

obtained by maximisation $\partial E_{CDW}/\partial\Delta = 0$ for a given electron-phonon coupling λ.

4.7 The phonon mode responsible for the CDW stabilisation

The phonon mode coupled to the electron system and responsible for the CDW stabilisation is to be found among the in-plane vibrations of the Ca lattice placed between the graphene sheets, being the softest "at hand to nature" to maximise the electron-phonon coupling

$$\lambda \sim \frac{g^2}{\omega_{\mathbf{Q}}}, \tag{4.73}$$

consequently increasing the CDW condensation energy. All graphene vibration modes, as well as flexural Ca modes, have significantly higher frequencies and so are excluded as such from this consideration. The coupling constant g will be discussed subsequently. Figure 4.7 (a) illustrates the geometry of the problem. Vibrational modes (phonons) of the 2D Ca lattice are

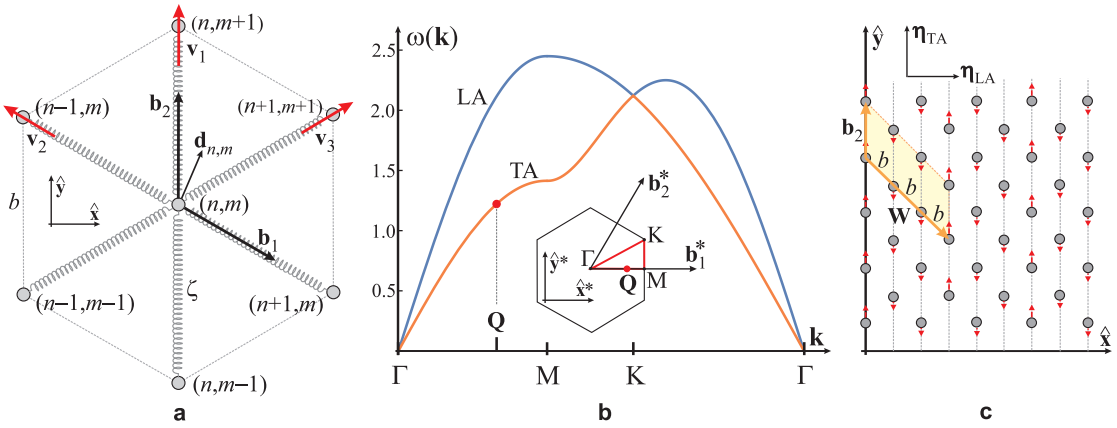

Figure 4.7: Phonon modes in the 2D hexagonal Ca-lattice (see Fig. 4.1(a)). (a) Ca atoms of mass M in the real space hexagonal structure where (n,m) are atomic positions $\mathbf{R}_{nm} = n\mathbf{b}_1 + m\mathbf{b}_2$, n, m are integers, where $\mathbf{b}_1 = \frac{1}{2}b(\sqrt{3},-1)$ and $\mathbf{b}_2 = b(0,1)$ are the unit vectors of the structure in the Cartesian basis $(\hat{\mathbf{x}},\hat{\mathbf{y}})$. Vibrations of the Ca atoms are described by the first-neighbour harmonic forces, with elastic constant ζ, along three characteristic directions determined by the symmetry, described by unit vectors $\mathbf{v}_1 = (0,1)$, $\mathbf{v}_{2,3} = \frac{1}{2}(\mp\sqrt{3},1)$. Displacement of the atom from the equilibrium position $\mathbf{R}_{nm}$ is $\mathbf{d}_{nm}$. (b) Phonon LA and TA in-plane modes $\omega(\mathbf{k})$ for the 2D hexagonal lattice in units $\sqrt{\zeta/M}$. The wave vector $\mathbf{k}$ is taken along direction between characteristic points in the Brillouin zone (inset) $\Gamma - M - K - \Gamma$. The Ca BZ (see also Fig. 4.2) is spanned by reciprocal vectors $\mathbf{b}_1^* = \frac{4\pi}{\sqrt{3}b}(1,0)$ and $\mathbf{b}_2^* = \frac{2\pi}{\sqrt{3}b}(1,\sqrt{3})$ in Cartesian reciprocal space $(\hat{\mathbf{x}}^*,\hat{\mathbf{y}}^*)$. $\mathbf{Q}$ is the wave vector of the phonon mode (red dot) related to the CDW. (c) Displacements of the Ca atoms (red arrows) $\mathbf{d}(\mathbf{Q})$ determined by the $\omega_{TA}(\mathbf{Q})$ phonon mode: atoms along the CDW peaks are displaced by $\mathbf{d}$, while the others are displaced by $-\mathbf{d}/2$ along the $\hat{\mathbf{y}}$-direction (η_{LA} and η_{TA} are directions of LA and TA polarisation, respectively).

represented using the harmonic first-neighbour approximation. The displacement of the atom from equilibrium at $\mathbf{R}_{nm}$ is:

$$\mathbf{R}_{nm} = n\mathbf{b}_1 + m\mathbf{b}_2, \tag{4.74}$$

where n and m are integers, and

$$\begin{aligned} \mathbf{b}_1 &= \frac{1}{2}b\begin{pmatrix} \sqrt{3} \\ -1 \end{pmatrix} \\ \mathbf{b}_2 &= b\begin{pmatrix} 0 \\ 1 \end{pmatrix} \end{aligned} \tag{4.75}$$

are the unit vectors of the structure in the Cartesian basis $(\hat{\mathbf{x}}, \hat{\mathbf{y}})$. Ca atom vibrations are characterised by the first-neighbor harmonic forces, with elastic constant ζ, along three distinctive directions determined by the symmetry of the problem, expressed by unit vectors

$$\begin{aligned} \mathbf{v}_1 &= (0,1) \\ \mathbf{v}_{2,3} &= \tfrac{1}{2}(\mp\sqrt{3},1). \end{aligned} \tag{4.76}$$

The displacement of a Ca atom, denoted by $\mathbf{d}_{nm}$, is described by the equation

$$M\frac{\mathrm{d}^2}{\mathrm{d}t^2}\mathbf{d}_{nm} = -\zeta\sum_{i=1}^{3}\left[(2\mathbf{d}(\mathbf{R}_{nm}) - \mathbf{d}(\mathbf{R}_{nm} + b\mathbf{v}_i) - \mathbf{d}(\mathbf{R}_{nm} - b\mathbf{v}_i))\cdot\mathbf{v}_i\right]\mathbf{v}_i, \tag{4.77}$$

where M is the mass of the atom, ζ is the linear elasticity constant, b is the lattice constant, while $\mathbf{v}_i$, $i = 1,2,3$, are the unit vectors along three characteristic directions of motion for the hexagonal symmetry (see Fig. 4.7 (a)). Assuming a solution of Eq. (4.77) in the standard form, i.e.

$$\mathbf{d}_{nm} = \eta\exp\{\mathrm{i}[\mathbf{k}\cdot\mathbf{R}_{nm} - \omega t]\}, \tag{4.78}$$

where $\mathbf{k}$ is the wave vector, ω is the frequency and $\eta = (\eta_x, \eta_y)$ is the polarisation vector of the phonon mode, Eq. (4.77) reduces to the secular equation

$$\begin{bmatrix} 3\frac{\zeta}{M}(1 - h_1(\mathbf{k})) - \omega^2 & -\sqrt{3}\frac{\zeta}{M}h_2(\mathbf{k}) \\ -\sqrt{3}\frac{\zeta}{M}h_2(\mathbf{k}) & \frac{\zeta}{M}(3 - h_1(\mathbf{k}) - 2h_3(\mathbf{k})) - \omega^2 \end{bmatrix}\begin{bmatrix} \eta_x \\ \eta_y \end{bmatrix} = 0, \tag{4.79}$$

where

$$\begin{aligned} h_1(\mathbf{k}) &\equiv \cos\left(\tfrac{\sqrt{3}}{2}k_x b\right)\cos\left(\tfrac{1}{2}k_y b\right) \\ h_2(\mathbf{k}) &\equiv \sin\left(\tfrac{\sqrt{3}}{2}k_x b\right)\sin\left(\tfrac{1}{2}k_y b\right) \\ h_3(\mathbf{k}) &\equiv \cos\left(k_y b\right). \end{aligned} \tag{4.80}$$

It yields the dispersion relation of phonon modes

$$\omega_{\pm}(\mathbf{k}) = \sqrt{\tfrac{\zeta}{M}}\left[3 - 2h_1(\mathbf{k}) - h_3(\mathbf{k}) \pm \sqrt{(h_1(\mathbf{k}) - h_3(\mathbf{k}))^2 + 3h_2(\mathbf{k})^2}\right]^{\frac{1}{2}} \tag{4.81}$$

(see Fig. 4.7 (b)). The phonon mode related to the CDW has a wave vector:

$$\mathbf{Q} = \frac{1}{3}\mathbf{b}_1^* = \frac{4\pi}{3\sqrt{3}b}\begin{pmatrix} 1 \\ 0 \end{pmatrix}, \tag{4.82}$$

which inserted into Eq. (4.81) yields two frequencies:

$$\begin{aligned} \omega_- &= \sqrt{3\zeta/2M} \\ \omega_+ &= \sqrt{9\zeta/2M}, \end{aligned} \tag{4.83}$$

and by virtue of Eq. (4.79), the corresponding polarisation unit vectors:

$$\begin{aligned} \eta_- &= (0,1) \\ \eta_+ &= (1,0) \end{aligned} \tag{4.84}$$

for TA and LA modes respectively. To maximise $\lambda \sim g^2/\omega_Q$, we compare g in both the TA and LA directions. The coupling g is created by the ionic shift of the phonon, which changes the electron-ion potential. In the spirit of tight binding approximation (TBA) [69, 70, 71, 72],

$$g \sim \nabla_{\mathbf{R}-\mathbf{R}'}\, t(\mathbf{R}-\mathbf{R}')\cdot\eta, \tag{4.85}$$

where $t(\mathbf{R}-\mathbf{R}')$ is the TBA transfer integral of electron hopping between sites at positions $\mathbf{R}$ (Ca) and $\mathbf{R}'$ (C) within the first neighbour approximation. Fig. 4.8 shows that Ca is centred below the carbon hexagon (so all ∇t are equal), yet the sum of their projections along the TA is greater than the sum along the LA direction. The reason for this is that Ca "strikes" directly into the carbon orbital along the TA, but not in the perpendicular LA direction, resulting in

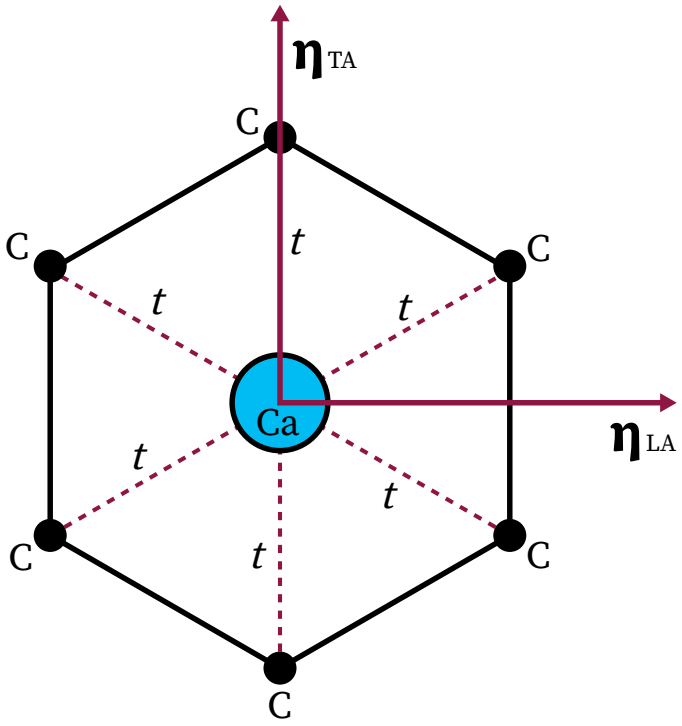

Figure 4.8: Illustration of te η_{LA} and η_{TA} polarisations inside the CaC_6 lattice. The calcium atom is illustrated as a blue circle, while the carbon atoms are located in a hexagonal lattice, each illustrated by a black circle and t is a Ca-C position-dependent TBA electron transfer integral.

$g_{TA} > g_{LA}$. The softer phonon mode between the two, ω_- (lower frequency, see Fig. 4.7 (b)), also corresponds to the TA mode with polarisation vector $\eta_{TA} \sim \eta_- \parallel \hat{\mathbf{y}}$, indicating the TA phonon responsible for the CDW. The displacement of atoms, or the distortion of the Ca lattice:

$$\mathbf{d}_{nm} = \eta_{TA} \cos\left[\mathbf{Q} \cdot \mathbf{R}_{nm}\right] \tag{4.86}$$

that corresponds to such polarisation and periodicity, is in a way that atoms along the CDW maxima (every 4th column along $\hat{\mathbf{y}}$-direction) are shifted by η_{TA} while all others are shifted by $-\frac{1}{2}\eta_{TA}$ (see Fig. 4.7 (c)) in terms of amplitude $d = |\eta_{TA}|$ proportional to the order parameter Δ. The amplitude of zero-point vibrations can be approximated using the mean value of a typical phonon displacement operator $a_0(b_{\mathbf{Q}} + b^{\dagger}_{-\mathbf{Q}})$:

$$d = 2\langle b_{\mathbf{Q}} \rangle a_0 = a_0 \Delta / g = a_0 \Delta \sqrt{\nu_0(\varepsilon_{F0})/(\hbar \omega_{\mathbf{Q}} \lambda)}. \tag{4.87}$$

Chapter 5

Discussion

To bring together the results of the aforementioned methods, we must place them in the context of a realistic material to the greatest extent possible. It is critical to emphasise that the onset of the CDW is due to electron band instability caused by the FS reconstruction, which opens the pseudo-gap and decreases band energy, as well as the accompanying softest phonon mode, which promotes this mechanism. As a result, the ability of a given system, with its specific geometry of the Brillouin zone, shape and size of the FS, and phonon modes reflecting the symmetry of the lattice, to be compatible with exactly such a self-consistent CDW wave vector that relates the FSs in the neighbouring Brillouin zones to touch or very slightly overlap is crucial. The CDW wave vector, which determines the overlap for a given FS, should not be too large or too short. In the first scenario, there is no overlap, therefore no FS reconstruction occurs, however in the second case, the overlap is so large that the upper energy band is filled. The CDW condensation energy vanishes in both scenarios. It is well known that a gap in a band, deep below the Fermi energy, has no effect on the ground state. The softened phonon mode must end up resulting in a static deformation of the crystal lattice that is geometrically and periodically compatible with the CDW. Furthermore, the electron-phonon coupling to that specific mode must be strong enough, larger than the critical value, which is rather high compared to weakly coupled Q1D materials [5, 73, 74, 75]. This is why most materials do not display the CDW ground state.

Ca intercalants chemically dope the carbon $\pi-$ band with 0.2 electrons per carbon atom, resulting in a Fermi surface with an average size of $2k_{F0} \approx 0.56\text{Å}^{-1}$. This is the characteristic scale of the CDW wave vector $\mathbf{Q}$, which is approximately equal to one third of the CaC_6 reciprocal unit vector $\mathbf{b}_1^*$, representing the phonon state on the $\Gamma - \text{M}$ line, close to the M-point of the CaC_6 Brillouin zone, as seen in Fig. 4.2. On the other hand, the Ca-intercalated lattice in CaC_6 appears to be particularly appropriate to promote the CDW instability for two reasons:

(1) The Ca lattice has a single phonon mode at the wave vector $\mathbf{Q}$ that is exactly compatible with the CDW geometry, minimising the "cost" in elastic deformation energy of the lattice (see Figs. 4.7 and 4.8). (2) While there are *ab initio* studies on electron-phonon coupling that consider intercalating atoms [76, 77, 78, 79, 80, 81, 82], few of them focus on momentum-resolved values. Unlike the well-studied problem of superconductivity in CaC_6, where the cumulative value or some momentum-averaged value of electron-phonon coupling is significant, the onset of the CDW instability requires sufficient coupling to the specific phonon mode at wave vector $\mathbf{Q}$. Among the above-mentioned studies, some recognise the role of *soft* Ca_{x-y} vibrations (~ 10 meV) compared to carbon vibrations (~ 100 meV) [81, 82] and some indicate the possibility of a significant value of the coupling constant between carbon band and Ca-lattice phonons [78].

The last-mentioned study shows that this electron-phonon coupling is very anisotropic and may attain large value at $\mathbf{Q}$ in proximity of the M-point of the CaC_6 Brillouin zone (see Fig. 4.7 (b)), presumably significantly larger than the required critical value of 0.54 predicted by this model. Any coupling greater than critical from one side directly adds to the rise of the CDW order parameter $\Delta \sim \lambda - \lambda_c$, but it also allows for fine-tuning of the CDW wave vector. Eq. (4.54) determines the optimal value of the CDW wave number Q_{opt} which is $2k_{F0}$ reduced by the quantity proportional to the order parameter. This value of Q_{opt} might not be commensurate to the reciprocal unit vectors of the lattice. This would result in incommensurability effects, which decrease the CDW order parameter, shorten the correlation length, produce domains, and otherwise inhibit CDW ordering. It is known to happen in high temperature superconducting cuprates by modifying the doping [83, 84, 85, 86] or in TMDs by pressure or intercalation [87, 88, 89]. With high electron-phonon coupling, it is not necessary to provide exactly $Q = Q_{opt}$, since the system may self-consistently fine-tune the CDW wave vector near to that value to minimise negative incommensurability effects. In the CaC_6 system, the (average) diameter of the FS is commensurate by factor 3 with the reciprocal unit vector $\mathbf{b}_1^*$ of the reciprocal lattice. The deviations from the circular form of the FS utilised in this model, assuming minimal in relation to the $\Delta/\hbar v_F$ scale, are not crucial for suppressing the CDW ordering (as it is in the "nesting" scenario). It explains the experimentally observed CDW wave vector $Q = b_1^*/3$. That phonon mode is "frozen" by the Kohn anomaly, resulting in static deformation of the Ca lattice, which stabilises the CDW. It is a transverse acoustic mode (TA) that displaces the Ca atoms in the direction η_{TA} parallel to the CDW peaks. The displacement is proportional to the order parameter, i.e. $d \sim \langle b_{\mathbf{Q}} \rangle \sim \Delta$. Fig. 5.1 displays the above-mentioned results, which are directly compared to the experimental findings [57]. The length of the CDW wave vector is determined by the electron band-driven CDW instability $Q = |\mathbf{b}_1^*|/3 \approx 2k_{F0}$ directed along direction of $\mathbf{b}_1^*$, which is one of the reciprocal unit vectors $(\mathbf{b}_1^*, \mathbf{b}_2^*)$ of the CaC_6 Brillouin zone that gets

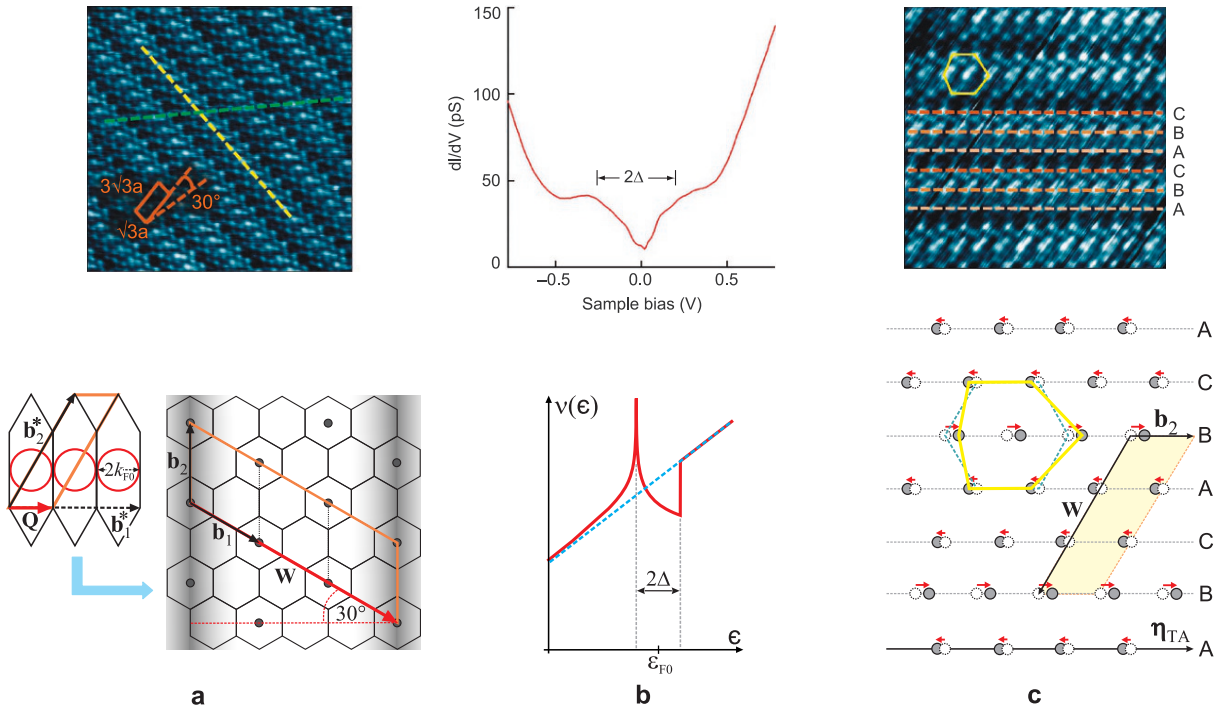

Figure 5.1: Comparison of experimental results (upper panel, from Ref. [57], Figs. 2d, 3a and 6a respectively, under Licence by courtesy of Springer Nature) with our theoretical results (lower panel).

shrunken three times (orange rhombus in Fig. 5.1) due to the onset of the CDW. In real space, this corresponds to the tripling of the CaC_6 unit cell, with unit vectors $(\mathbf{b}_1, \mathbf{b}_2)$, along the $\mathbf{b}_1$ direction (orange rhombus) in the CDW phase

$$\mathbf{W} = 3\mathbf{b}_1. \tag{5.1}$$

Charge stripes create peaks (shaded) along the $\mathbf{b}_2$ direction. Those peaks occur periodically at a distance of 4.5 graphene unit constants a along the zig-zag direction of the graphene lattice. In the STM experimental image (upper left panel), the stripe peak is along the yellow line, and the orange rhombus is the CDW-extended CaC_6 unit cell corresponding to the one in the lower panel where $b = \sqrt{3}a$.

The reconstruction of the Fermi surface opens a pseudo-gap of width 2Δ in the density of states $\nu(\varepsilon)$, around the Fermi energy $\varepsilon = \varepsilon_{F0}$ (Fig. 5.1 (b)), where Δ is the CDW order parameter. The full red and dashed blue curves represent $\nu(\varepsilon)$ after and before the FS reconstruction, respectively. The experiment (upper panel) of measuring the differential conductivity of the STM tunnelling current, which is proportional to LDOS, vs. the bias voltage with respect to the Fermi energy, reveals a pseudo-gap of width 2Δ.

The CDW causes static deformation of the initial Ca lattice (dashed circles and blue hexagon) through the "frozen" TA phonon mode (Fig. 5.1 (c)): Ca atomic displacements (red arrows) follow the polarisation direction $\eta_{TA} \parallel \mathbf{b}_2$, whereas the propagation direction is perpendicular to it. This phonon mode is the softest one at the wave vector $\mathbf{Q}$ (see Fig. 4.7), displacing the Ca atoms at $\mathbf{R}_{nm}$ by

$$\mathbf{d}_{nm} \sim \eta_{TA} \cos(\mathbf{Q} \cdot \mathbf{R}_{nm}) \tag{5.2}$$

in a way that chains B (CDW peaks) are shifted by $+d$, whereas A and C are displaced by $-d/2$ in the η_{TA} direction ($d \sim \Delta$). The Ca hexagon in the deformed lattice (full circles) is indicated by a yellow contour, which corresponds to the experimentally observed STM pattern indicating Ca atom positions (in the upper panel of Fig. 5.1 (c)).

Chapter 6

Magnetoconductivity under the conditions of coherent magnetic breakdown

In this chapter, we focus on the magnetotransport properties in the reconstructed geometry of the Fermi surface. The spacing between the open contours in the reciprocal space, reconstructed from closed ones to such due to the CDW, corresponds to the energy scale of the order of 10^2K. Therefore, in a strong magnetic field, the effects of magnetic breakdown are expected to be pronounced, profoundly affecting the properties of the electron spectrum and transport properties.

The phrase "Magnetic Breakdown" (MB) generally refers to a class of phenomena resulting from the quantum tunnelling transition between electron trajectories mainly belonging to different conduction bands of a metal in a magnetic field.

6.1 Semiclassical approximation and Magnetic Breakdown

The motion of conduction electrons in a 3D system can be described within the semiclassical approximation by the classical equations of motion [90, 91]:

$$\begin{aligned} \frac{\mathrm{d}\mathbf{p}}{\mathrm{d}t} &= -e\mathbf{v}_m \times \mathbf{B}, \\ \mathbf{v}_m &= \frac{\partial \varepsilon_m(\mathbf{p})}{\partial \mathbf{p}}, \\ \frac{\mathrm{d}\mathbf{r}}{\mathrm{d}t} &= \mathbf{v}_m(\mathbf{p}), \end{aligned} \tag{6.1}$$

where e is an absolute value of electron charge and $\mathbf{B}$ is an external magnetic field. Here, $\mathbf{p} = \hbar\mathbf{k}$ is the quasimomentum of an electron related to the wave vector $\mathbf{k}$, which is equivalent

to momentum in a classical description, $\mathbf{r}$ stands for the electron coordinate, $\varepsilon_m(\mathbf{p})$ represents the electron energy associated with the m-th band and $\mathbf{v}_m$ is the semiclassical group velocity of an electron. Equations (6.1) provide a classical trajectory of an electron in p-space, which has a distinct geometric meaning: it is the line that intersects a plane perpendicular to the magnetic field and a constant-energy (E) surface. It is determined from the condition

$$\begin{aligned} &\varepsilon_m(p_x, p_y, p_z) = E, \\ &p_z = p_{z_0}, \end{aligned} \tag{6.2}$$

where p_{z_0} is the conserved component of the electron momentum paralell to the magnetic field. As is customary, the z-axis runs parallel to the magnetic field. A small parameter guarantees the semiclassical character of motion,

$$\frac{\hbar\omega_c}{\varepsilon_0} \ll 1, \tag{6.3}$$

where

$$\omega_c = \frac{eB}{m} \tag{6.4}$$

is the electron cyclotron frequency, ε_0 is the typical electron energy, of the order of the Fermi energy ε_F [91]. Here, $m \equiv m(\varepsilon)$ is the electron cyclotron mass. Trajectories, determined by Eq. (6.2), can be closed or open [91]. In the case of closed trajectories, semiclassical quantization produces discrete energy levels E_n (for a fixed value of p_z), where the level number n has a physical meaning — it determines quantised section areas of constant-energy surfaces (Lifshitz-Onsager quantisation). In a semiclassical description, if an electron moves infinitely in a plane perpendicular to the magnetic field (open paths), the quantization of its motion can be ignored [91]. Thus, in the semiclassical theory, the periodicity and anisotropy of the dispersion law (6.2) cause all particular properties of the dynamics of conduction electrons in a magnetic field. Naturally, some properties of the electron dynamics in a magnetic field become more prominent when its characteristic Larmor radius $R_L = p_F/eB$ (radius of cyclotron motion of an electron) is significantly shorter than its free path $l_0 = v_F\tau_0$, v_F is a typical electron velocity i.e. the Fermi velocity, τ_0 is the relaxation time. The inequality

$$\frac{R_L}{l_0} \approx \frac{1}{\omega_c\tau_0} \ll 1 \tag{6.5}$$

which allows one to ignore details of dissipative processes in the electron gas, combined with the condition of semiclassical behaviour (6.3), allows one to calculate thermodynamic and kinetic characteristics and obtain relatively simple expressions. The inequalities (6.3) and (6.5) can be joined to obtain

$$\frac{1}{\tau_0} \ll \omega_c \ll \frac{\varepsilon_F}{\hbar}, \tag{6.6}$$

defining the physical conditions of validity of the presented model.

Trajectories of different band indices m approach in p-space regions where the interband energy gap $\Delta(\mathbf{p}) = \varepsilon_m(\mathbf{p}) - \varepsilon_{m'}(\mathbf{p})$ is significantly smaller than ε_F, particularly near the lines of degeneracy, where $\Delta(\mathbf{p}) = 0$. According to general quantum mechanical principles [92], such a line must exist for around half of the metals [90]. If these lines cross the Fermi surface, their existence is clearly evident in macroscopic features. This condition occurs quite frequently (Zn, Nb, C, and so on) [91] leading to magnetic breakdown. Magnetic breakdown always occurs with relatively large groups of electrons involved, hence it changes the qualitative picture of most electron events in the magnetic field.

Even though the interband tunnelling areas (MB regions) are small, they represent peculiar centres where substantial quantum scattering of electrons occurs. This MB-scattering contains two channels and is characterised by a second rank unitary S-matrix. The squared modulus of its non-diagonal elements represents the probability of an interband transition of an electron in a magnetic field - the MB probability, w [91].

Without doing consistent computations, the values of B at which the MB probability w becomes significant (tends to 1) can be estimated. The momenta p_x and p_y play the role of canonically conjugated quantities in a magnetic field directed along the z-axis, and their quantum uncertainty Δp_x and Δp_y meet the relation

$$\Delta p_x \Delta p_y \gtrsim \frac{e\hbar B}{2}. \tag{6.7}$$

Interband tunnelling becomes significant when the characteristic uncertainty Δp_x and Δp_y equal to $(e\hbar B)^{1/2} \sim p_F(\hbar\omega_c/\varepsilon_F)^{1/2}$ (Eq. 6.7), is comparable to the minimal distance between trajectories $\delta p \sim \Delta/v_F$. The characteristic scale of the breakdown field is $B_0 = (1/e\hbar)(\Delta^2/v_F^2)$. The value $B_0 \sim 1 - 10\text{T}$ corresponds to $\Delta \sim 10^{-2}\text{eV}$. For $B \to \infty$, the probability of MB approaches unity [91].

Outside of the MB zones, electron motion is semiclassical. However, under MB conditions, electron dynamics is quantum due to the interference from semiclassical waves. The interference of the MB-dynamics significantly affects electron characteristics in the system [91].

The semiclassical motion between MB areas implies large phases of conduction electron wave functions, which depend on energy, momentum projection on the magnetic field, and the magnetic field itself. There is no reason to think that phases and their derivatives (in terms of energy and momentum projection) should be commensurable across sections. Under MB circumstances, the electron energy spectrum becomes more complex and similar to that of disordered systems. The MB-spectrum has qualities that fall in between a strictly ordered (locally equidistant) spectrum in the semiclassical limit and a completely disordered system with quasirandom spectrum [91].

The MB-spectrum becomes semiclassical for both $w \to 0$ and $w \to 1$ when electrons migrate onto new classical orbits made up of parts of previous orbits. The motion appears to be quasi-classical in both weak and strong magnetic fields, which is unusual. This study of metal characteristics under MB circumstances focuses on the intermediate scenario of developed breakdown, when the probability w is not close to zero or unity, and quantum interference plays a substantial role. Under MB conditions, electron motion is primarily quantum in nature in the sense of pronounced interference effects, making it difficult to understand certain phenomena without a specialised mathematical approach. [91].

6.2 The Model

As shown in section 4.1, we model the CaC_6 system as a 2D graphene sheet, chemically doped by electrons from intercalating atoms to provide finite electron pockets at the Fermi energy, creating the Fermi surface in the center of the CaC_6 Brillouin zone (Γ point). The Fermi surface in the minimal model can be approximated with a 6-fold degenerate circle, while the details of the shape of the Fermi pockets can be addressed in the conductivity calculations as parameters appearing as effective carrier concentrations. The uniaxial CDW potential reduces the BZ and brings the Fermi pockets from neighbouring BZs to touching or slightly overlap, leading in turn to the reconstruction of the Fermi surface (see Fig. 6.1 (c)). The Fermi surface is topologically reconstructed: from the closed pockets, it is turned into set of open sheets. To study the magnetoconductivity, the system is put into an external homogeneous magnetic field **B**, perpendicular to the sample plane. The configuration of the real and reciprocal space is schematically shown in Fig. 6.1, following from considerations shown in Figs. 4.1 and 4.2. The size of the 6-fold degenerate unreconstructed Fermi pocket is $S_{F0} \approx 0.244 \mathring{A}^{-2}$ with an average Fermi wave number $k_{F0} \approx 0.28 \mathring{A}^{-1}$.

The CDW potential, with the wave vector $\mathbf{Q} \parallel \mathbf{b}_1^*$ of periodicity $Q = b^*/3 \approx 0.56 \text{Å}^{-1}$, folds

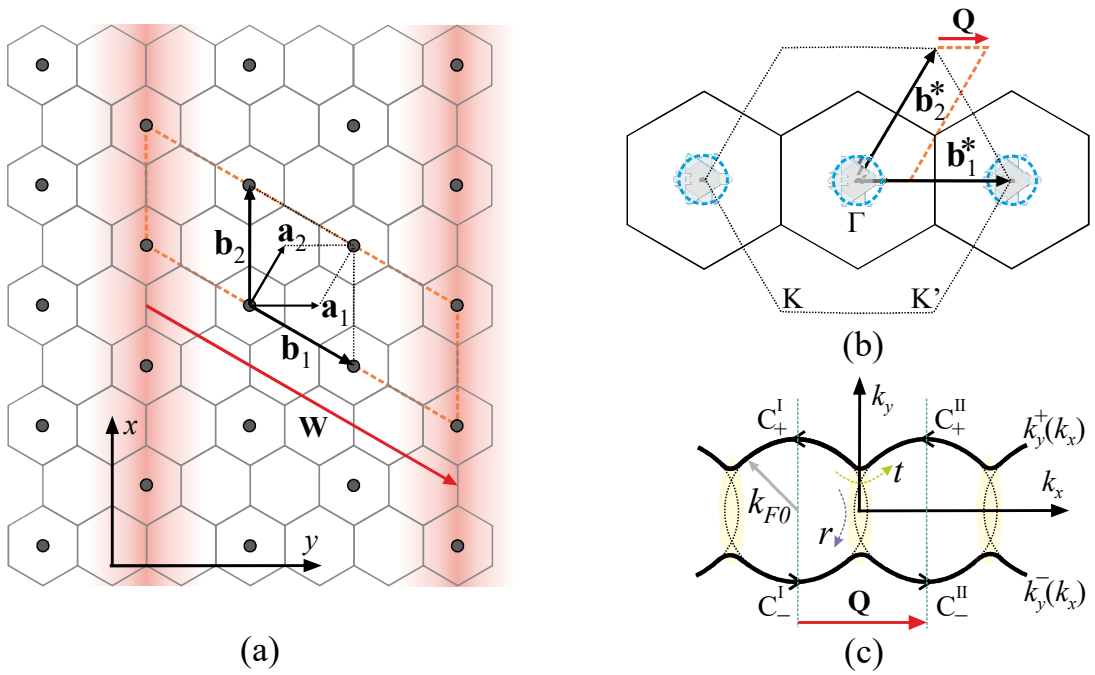

Figure 6.1: Schematic presentation of a 2D layer in CaC_6 in real and reciprocal space (see Figs. 4.1 and 4.2): (a) Real space, (b) Reciprocal space. (c) The Fermi surface reconstructed by the CDW potential in the semiclassical picture. Arrows show the direction of semiclassical motion of electrons in external magnetic field **B** perpendicular to the sample, t and r are probability amplitudes characterising magnetic breakdown transitions. Image from [93].

the CaC_6 BZ, bringing the FSs into touch, i.e. $Q \approx 2k_{F0}$. The corresponding unit cell in reciprocal space is marked by dashed orange rhombus in Fig. 6.1 (b).

The reconstructed Fermi surface consists of open sheets in k_x-direction (Fig. 6.1 (c)). The arrows show the direction of semiclassical motion of electrons in external magnetic field **B** perpendicular to the sample. Magnetic breakdown affects the semiclassical motion causing electrons to pass through the MB-junctions (shaded) with the probability amplitude $t(B)$, or get reflected from it with the probability amplitude $r(B)$, $C_{\pm}^{\mathrm{I,II}}$ are coefficients denoting the branches of the semiclassical wave functions corresponding to the trajectories $k_y^{\pm}(k_x;\varepsilon)$.

The zero-field electron spectrum in the CDW ground state attains the well known form Eq. (4.4). Here, the origin of the reciprocal space is conveniently chosen at the crossing point of the initial electron bands, the edge of the reconstructed BZ (see Fig. 6.1 (c)).

6.3 Electron spectrum and wave functions

To obtain the electron spectrum in an external magnetic field **B** perpendicular to the sample, under conditions of magnetic breakdown, we utilize a semiclassical technique based on the Lifshitz-Onsager Hamiltonian [94, 95] which describes semiclassical motion of electrons. The necessary assumption, required to formulate magnetic breakdown problem beyond the mere perturbative contribution of magnetic field, is that the field is strong enough to provide the Larmor radius of electron motion much smaller that the mean free path of scattering on impurities, Eq. (6.5). The further assumption is the absence of dislocation fields, required to provide conditions for so-called *coherent magnetic breakdown* [91] which is in the focus of this work. The limit of so-called *stohastic magnetic breakdown* [96] is not a subject of this work. Choosing the Landau gauge of the vector potential

$$\mathbf{A} = (0, Bx, 0), \tag{6.8}$$

the Lifshitz-Onsager Hamiltonian leads to the Schrödinger equation in the reciprocal space

$$\varepsilon_l \left(k_x, K_y - i\frac{b_B^2}{\hbar^2}\frac{\mathrm{d}}{\mathrm{d}k_x} \right) G_l(k_x, K_y) = \varepsilon G_l(k_x, K_y), \tag{6.9}$$

where $\varepsilon_l(k_x, k_y)$ is the initial electron dispersion shifted in the reciprocal space to the position corresponding to trajectories I, II with branches $\pm$ (see Fig 6.1 (c)), $b_B = \sqrt{e\hbar B}$ is the "magnetic length" for electron with charge $-e$, $\hbar K_y$ is the conserved generalized momentum of the semiclassical motion of electron in the used gauge, ε is the eigenvalue of energy. The semiclassical eigenfunctions are

$$G_\pm(k_x, K_y) = \frac{C_\pm}{\sqrt{|v_y^\pm|}} \exp\left[i\frac{\hbar^2}{b_B^2} \int^{k_x} \left(k_y^\pm(k_x'; \varepsilon_F) - K_y \right) \mathrm{d}k_x' \right] \tag{6.10}$$

analogous for both regions I, II (we omit writing indices for now), where $C_\pm$ are the corresponding coefficients, $v_y^\pm \equiv v_y(k_x; k_y^\pm(k_x, \varepsilon))$ are the group velocity components of $\mathbf{v} = \frac{1}{\hbar}\nabla_{\mathbf{k}}\varepsilon(\mathbf{k})$ along the semiclassical electron trajectories at energy ε. The coefficients $C_\pm$ are found by matching the wave functions (6.10) at the MB points. The integral in the exponent is the semiclassical phase (area enclosed by the trajectory in the reciprocal space, i.e. the semiclassical action) with the lower limit determined by the starting point of the trajectory along the $k_y^\pm(k_x; \varepsilon_F)$ at the

Fermi energy ε_F. Note that these trajectories in the presented procedure are found from the equation

$$\varepsilon_{\pm}(k_x, k_y) = \varepsilon_F, \tag{6.11}$$

i.e. from the initial electron dispersion with the gap parameter Δ neglected (dotted trajectories in Fig. 6.1 (c)), therefore the solutions are valid far from the MB-regions. In the considered case this dependence is simply

$$k_y^{\pm}(k_x;\varepsilon) = \pm\sqrt{(\varepsilon/\hbar v_F)^2 - k_x^2}. \tag{6.12}$$

The semiclassical solutions $G_{\pm}^{\mathrm{I,II}}$ in regions I and II (see Fig. 6.1 (c)), characterised by coefficients $C_{\pm}^{\mathrm{I,II}}$, are connected in the "MB-junction" by the MB-scattering matrix that relates pairs of incoming and outgoing electron waves

$$\begin{pmatrix} C_-^{\mathrm{I}} \\ C_+^{\mathrm{II}} \end{pmatrix} = \mathrm{e}^{i\theta} \begin{pmatrix} t & r \\ -r^* & t^* \end{pmatrix} \begin{pmatrix} C_-^{\mathrm{II}} \\ C_+^{\mathrm{I}} \end{pmatrix}. \tag{6.13}$$

Here $t(B)$ and $r(B)$, fulfilling the unitarity condition

$$|t|^2 + |r|^2 = 1, \tag{6.14}$$

are the complex probability amplitudes for electron to pass through the MB-region and to get reflected on it, respectively, while θ is the phase determined by the problem-specific boundary conditions. It has been shown [97, 98, 99, 100] that, in the configuration originating form the very slight overlap of semiclassical trajectories, the probability of passing through the MB-region is

$$|t(B)|^2 \approx 1 - \exp\left[-\frac{\Delta^2}{\hbar\omega_c\varepsilon_F}\sqrt[3]{\frac{\varepsilon_F}{\hbar\omega_c}}\right], \tag{6.15}$$

$\hbar\omega_c = \hbar eB/m$ is often called the "magnetic energy". The effective cyclotron mass m is a well-known quantity, i.e.

$$m(\varepsilon) = \frac{\hbar^2}{2\pi}\frac{\mathrm{d}S(\varepsilon)}{\mathrm{d}\varepsilon}, \tag{6.16}$$

where $S(\varepsilon)$ is the area enclosed by electron trajectory in the reciprocal space at energy ε, in the case of graphene and graphite being $m(\varepsilon) = \varepsilon/v_F^2$ for low enough energy. One can immediately notice that the exponent in Eq. (6.15) has an additional large factor, i.e. the third root of ratio of the Fermi energy and magnetic energy, compared with the standard Blount's result [101] obtained for an arbitrary large overlap of trajectories. It is the result of the peculiar band topology in the reconstruction region.

The periodic boundary conditions, imposed upon the semiclassical solutions by the CDW, i.e.

$$G_{\pm}(k_x, K_y) = G_{\pm}(k_x + Q, K_y), \tag{6.17}$$

yield two additional relations between four coefficients $C_{\pm}^{\mathrm{I,II}}$,

$$C_{\pm}^{\mathrm{I}} = C_{\pm}^{\mathrm{II}} \exp\left\{\left[-i\frac{\hbar^2}{b_B^2}\int_0^Q \left(k_y^{\pm}(k_x;\varepsilon_F) - K_y\right)\mathrm{d}k_x\right]\right\}, \tag{6.18}$$

constituting, together with (6.13), a homogeneous system of two algebraic equations for two unknowns C_+^{I} and C_-^{I}, i.e.

$$\begin{pmatrix} C_-^{\mathrm{I}} \\ C_+^{\mathrm{I}} \end{pmatrix} = \mathrm{e}^{i\theta} \begin{pmatrix} t & r \\ -r^* & t^* \end{pmatrix} \begin{pmatrix} C_-^{\mathrm{I}} \exp\left\{\left[-i\frac{\hbar^2}{b_B^2}\left(S_- + QK_y\right)\right]\right\} \\ C_+^{\mathrm{I}} \exp\left\{\left[-i\frac{\hbar^2}{b_B^2}\left(S_+ - QK_y\right)\right]\right\} \end{pmatrix}. \tag{6.19}$$

Here,

$$\begin{aligned} S_+(\varepsilon) &= \int_0^Q k_y^+(k_x;\varepsilon)\mathrm{d}k_x, \\ S_-(\varepsilon) &= \int_Q^0 k_y^-(k_x;\varepsilon)\mathrm{d}k_x \end{aligned} \tag{6.20}$$

are the semiclassical actions along the corresponding electron trajectories. The determinant of that system, taken at arbitrary energy ε, reads

$$D(\varepsilon, K_y) = \cos\left(\frac{\hbar^2 S_0(\varepsilon)}{2b_B^2} + \theta\right) - |t|\cos\left(\frac{\hbar^2 Q K_y}{b_B^2} + \mu\right), \tag{6.21}$$

where

$$S_0(\varepsilon) = S_+(\varepsilon) + S_-(\varepsilon) \tag{6.22}$$

is the area of the reciprocal space enclosed by the electron trajectory (dotted circle in Fig. 6.1 (c)). Phase μ, appearing from $t = |t|\exp(i\mu)$, is, along with the phase θ, determined by the boundary conditions of the problem, specific for the particular MB configuration depending on magnetic field, obtained by matching the semiclassical solution to the asymptotic form of exact quantum-mechanical solution within the MB region [97, 98]. The electron spectrum is determined from the dispersion equation

$$D(\varepsilon, K_y) = 0. \tag{6.23}$$

For example, in high enough fields to produce a very strong magnetic breakdown $|t(B)| \to 0$, $|r(B)| \to 1$, the dominant electron motion is along the closed orbits (dotted circles in Fig. 6.1 (c)) due the maximized over-gap tunnelling between open trajectories $k_y^+(k_x)$ and $k_y^-(k_x)$. The orbital effect of the magnetic field is then a mere Landau quantization of closed orbits. The dispersion law reduces to

$$\cos\left(\frac{\hbar^2 S_0(\varepsilon)}{2b_B^2} + \theta\right) = 0 \tag{6.24}$$

which, assuming the initial spectrum $\varepsilon = \hbar v_F |\mathbf{k}| b$ and $S_0 = \pi|\mathbf{k}|^2$, yields the Landau-quantized spectrum in magnetic field

$$\varepsilon_n = \pm v_F b_B \sqrt{2(n + 1/2 - \theta/\pi)} \qquad\qquad n = 0, 1, 2, \ldots \tag{6.25}$$

In contrast to the monolayer graphene, where the nontrivial geometric (Berry) phase $\phi_B = \pi$ appears leading to spectrum with Landau level $\varepsilon_{n=0}$ at zero energy, in graphite the geometric phase is trivial [102]. The $|t| = 0$ case in graphite yields $\theta = 0$ [97, 98], finally resulting in spectrum

$$\varepsilon_n = \pm v_F \sqrt{2e\hbar B(n + 1/2)}, \tag{6.26}$$

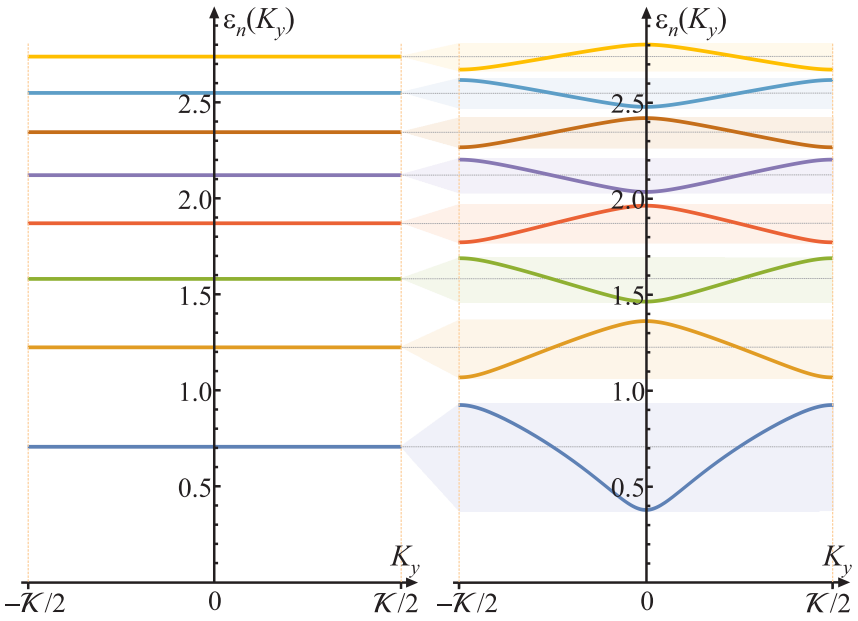

Figure 6.2: Spectrum (6.27) in the nondispersive $|t| \to 0$ limit, essentially consisting of Landau levels (left panel), and for $|t| = 0.9$ where magnetic bands are formed due to magnetic breakdown (right panel). Energy $\varepsilon_n(K_y)$, $n = 0, 1, ..., 7$ is scaled to $v_F\sqrt{2e\hbar B}$ and displayed along the "magnetic zone" of width $\mathcal{K} = 2\pi b_B^2/\hbar^2 Q = 2\pi eB/\hbar Q$. For the matter of presentation we set phases $\theta = \mu = 0$. Image from [93].

which we adopt in our consideration although in our model we use two-dimensional formalism. The spectrum for arbitrary $|t(B)|$ can be obtained in closed form, reading

$$\varepsilon_n(K_y) = \pm v_F\sqrt{2e\hbar B}\left[n + \frac{1}{2}\left(1-(-1)^n\right) - \frac{\theta}{\pi} + \frac{(-1)^n}{\pi}\arccos\left(|t|\cos\left(\frac{\hbar^2 Q K_y}{b_B^2} + \mu\right)\right)\right]^{\frac{1}{2}} \tag{6.27}$$

for $n = 0, 1, 2, ...$, shown in Fig. 6.2. Besides the dispersion law, the system (6.19) also determines relation between coefficients, i.e.

$$C_- = \frac{r\exp\{[i(\phi - \kappa_y + \theta)]\}}{1 - t\exp\{[i(\phi + \kappa_y + \theta)]\}} C_+, \tag{6.28}$$

where

$$\kappa_y \equiv \frac{\hbar^2 Q K_y}{b_B^2} \tag{6.29}$$

and

$$\phi \equiv S_+ = S_-. \tag{6.30}$$

The complete semiclassical wave function is

$$G_\eta(k_x) = \frac{C_+}{\sqrt{|v_y^+|}} \exp\left\{ \left[i\frac{\hbar^2}{b_B^2} \int_0^{k_x} \left(k_y^+(k_x') - K_y\right) \mathrm{d}k_x' \right] \right\} + \frac{C_-}{\sqrt{|v_y^-|}} \exp\left\{ \left[i\frac{\hbar^2}{b_B^2} \int_Q^{k_x} \left(k_y^-(k_x') - K_y\right) \mathrm{d}k_x' \right] \right\}. \tag{6.31}$$

Constants C_+ and C_- are also related by the normalisation condition of the wave function

$$\langle G_\eta(k_x) \mid G_\eta(k_x) \rangle = 1, \tag{6.32}$$

where

$$\eta = \{K_y, n\} \tag{6.33}$$

is a set of all good quantum numbers. Condition (6.32), after neglecting the fast-oscillating cross-terms, reduces to

$$|C_+|^2 + |C_-|^2 = \left(\frac{L_x}{2\pi} \int_0^Q \frac{\mathrm{d}k_x}{|v_y(k_x)|} \right)^{-1}, \tag{6.34}$$

where L_x is the length of the sample in x-direction [91]. Here we used the fact that due to symmetry of the $\pm$ trajectories, the velocity components are equal by absolute value, i.e. $|v_y| \equiv |v_y^+| = |v_y^-|$. For further procedures, it turns convenient to normalize the wave function to the period of the cyclotron motion around the semiclassical orbit. Assuming this motion to be governed by the Lorentz force, i.e.

$$\hbar \frac{\mathrm{d}\mathbf{k}}{\mathrm{d}t} = -e\mathbf{v} \times \mathbf{B}, \tag{6.35}$$

and from there substituting

$$\mathrm{d}k_x = -\frac{1}{\hbar} eB v_y \mathrm{d}t \tag{6.36}$$

into Eq. (6.34), we obtain

$$|C_+|^2 + |C_-|^2 = \left(\frac{L_x}{2\pi\hbar} eB \frac{T(\varepsilon)}{2} \right)^{-1}, \tag{6.37}$$

where $T(\varepsilon)$ is the period of electron motion around the circular semiclassical trajectory at energy ε, i.e. $T/2$ corresponds to the integral over k_x from 0 to Q in Eq. (6.34). T is related to the cyclotron frequency ω_c in the standard way, $T = 2\pi/\omega_c$. $|C_+|^2$ and $|C_-|^2$ are determined by the system of equations (6.28,6.37).

6.4 Magnetoconductivity

The magnetoconductivity tensor of a 2D system is obtained using the quantum density matrix formalism up to the linear correction to the equilibrium conditions (see Ref. [103] for the derivation details), with the general form of it reading

$$\sigma_{\alpha\beta} = -\frac{2e^2}{L_x L_y} \sum_{\eta,\eta'} \frac{\langle \eta | \hat{v}_\alpha | \eta' \rangle \langle \eta' | \hat{v}_\beta | \eta \rangle}{\frac{i}{\hbar}\left(\varepsilon_{\eta'} - \varepsilon_\eta\right) + \frac{1}{\tau_0}} \frac{\mathrm{d}f(\varepsilon)}{\mathrm{d}\varepsilon}\Big|_{\varepsilon=\varepsilon_\eta}, \tag{6.38}$$

where $\alpha, \beta \in \{x, y\}$ account for directions along the real space (see Fig. 6.1 (a)) containing a 2D sample of the size L_x by L_y and operators are noted with a "hat". The function

$$f(\varepsilon) = \left(\exp\left[(\varepsilon - \varepsilon_F)/k_B T\right] + 1\right)^{-1} \tag{6.39}$$

is a standard Fermi distribution at temperature T. In this expression, τ_0 is the relaxation time due to electron scattering on impurities, with all other channels of relaxation neglected in this approach at low enough temperatures. It needs to be emphasized that the results that are about to be presented are derived in the limit in which the impurity scattering rate is much smaller comparing to the cyclotron frequency, i.e. $\omega_c \gg \tau_0^{-1}$, in accordance with Eq. (6.6).

Within the coherent magnetic breakdown regime, the width of magnetic bands $W(B)$ versus the level broadening caused by impurity scattering is the next significant physical scale. The tunnelling probability amplitude $|t(B)|$ (6.15) through Eq. (6.27) effectively controls $W(B)$, which is dependent on magnetic field. The structure of magnetic bands and related interference effects vanish in the limit $W(B) \ll \hbar\tau_0^{-1}$, and physics is reduced to just the Landau level physics. The purpose of this study is to investigate the full-scale MB effects, which we predict to be prominent in the opposite limit

$$W(B) \gg \hbar\tau_0^{-1}. \tag{6.40}$$

The 2×2 magnetoconductivity is anisotropic. It contains:

1. a σ_{xx} component along the CDW peaks in real space and perpendicular to the open electron trajectories in the reciprocal space;
2. a σ_{yy} component along the CDW periodicity direction in real space and along the open electron trajectories in the reciprocal space;
3. $\sigma_{xy} = -\sigma_{yx}$ are the Hall conductivity components.

6.4.1 Diagonal magnetoconductivity σ_{xx}

The diagonal magnetoconductivity along x-direction has to be calculated directly from Eq. (6.38) by evaluating the matrix element

$$\langle \eta | \hat{v}_x | \eta' \rangle \tag{6.41}$$

due to vanishing semiclassical group velocity along that direction at the apex of the corresponding trajectory (see Fig. 6.1 (c), k_y-direction). Using the above-mentioned expression for the Lorentz force (6.35),

$$\hbar \dot{k}_y = e v_x B, \tag{6.42}$$

and equation of motion for the momentum operator

$$\dot{\hat{k}}_y = \frac{i}{\hbar} \left[\hat{\mathcal{H}}, \hat{k}_y \right], \tag{6.43}$$

we obtain

$$\hat{v}_x = \frac{i}{eB} \left[\hat{\mathcal{H}}, \hat{k}_y \right], \tag{6.44}$$

where $\hat{\mathcal{H}}$ is Hamiltonian of the system with eigenvectors $|\eta\rangle$ and corresponding eigenvalues ε_η [91, 104]. The sought for matrix element can be directly evaluated, i.e.

$$\langle \eta | \hat{v}_x | \eta' \rangle = \tfrac{i}{eB} (\varepsilon_\eta - \varepsilon'_\eta) \langle \eta | \hat{k}_y | \eta' \rangle. \tag{6.45}$$

Inserting this expression in Eq. (6.38) the $\eta = \eta'$ contributions in double summation vanish. For $\eta \neq \eta'$ we expand the fraction

$$\left(\frac{i}{\hbar}(\varepsilon_{\eta'} - \varepsilon_{\eta}) + \tau_0^{-1}\right)^{-1} \tag{6.46}$$

under assumption $|\varepsilon_{\eta} - \varepsilon_{\eta'}| \gg \hbar\tau_0^{-1}$ up to the first term in Taylor series. After performing one summation over the complete set $|\eta'\rangle$ and using

$$\langle\eta|\hat{k}_y|\eta\rangle = 0 \tag{6.47}$$

for a symmetric trajectory, Eq. (6.38) reduces to

$$\sigma_{xx} = -\frac{2e^2\hbar^4}{L_x L_y \tau_0 b_B^4} \sum_{\eta} \langle\eta|\hat{k}_y^2|\eta\rangle \left.\frac{\mathrm{d}f(\varepsilon)}{\mathrm{d}\varepsilon}\right|_{\varepsilon_\eta}. \tag{6.48}$$

To evaluate the matrix element $\langle\eta|\hat{k}_y^2|\eta\rangle$, we use the semiclassical wave functions (6.31), i.e. $|\eta\rangle = G_{n,K_y}(k_x)$ yielding

$$\langle\eta|\,\hat{k}_y^2\,|\eta\rangle = \frac{L_x}{2\pi}\int_0^Q \mathrm{d}k_x \frac{\left(k_y^+(k_x,\varepsilon_n(K_y))\right)^2}{|v_y(k_x,\varepsilon_n(K_y))|}\left(|C_+(K_y,\varepsilon_n(K_y))|^2 + |C_-(K_y,\varepsilon_n(K_y))|^2\right). \tag{6.49}$$

The fraction in Eq. (6.49) can be further simplified using the relations

$$\varepsilon(k_x,k_y) = \hbar v_F\sqrt{k_x^2+k_y^2} \tag{6.50}$$

and $\hbar v_y = \frac{\partial\varepsilon(\mathbf{k})}{\partial k_y}$ i.e.

$$\frac{k_y^2}{|v_y|} = \frac{m(\varepsilon)k_y}{\hbar}, \tag{6.51}$$

where $m(\varepsilon) \equiv \varepsilon / v_F^2$. Inserting Eq. (6.49) into Eq. (6.48) and changing the variable $\varepsilon_n \to \varepsilon$ by inserting the integral over delta function $\int d\varepsilon\, \delta(\varepsilon - \varepsilon_n)$ we obtain

$$\begin{aligned}\sigma_{xx} = &- \frac{2e^2\hbar^4}{L_x L_y \tau_0 b_B^4} \int_{-\infty}^{\infty} d\varepsilon \sum_n \delta(\varepsilon - \varepsilon_n) \frac{m(\varepsilon)}{\hbar} \frac{df(\varepsilon)}{d\varepsilon} \\ &\times \frac{L_x}{2\pi} \int_0^{\mathcal{Q}} dk_x k_y^+(k_x, \varepsilon) \\ &\times \frac{L_y}{2\pi} \int_0^{K_y^m} dK_y \left(|C_+(K_y, \varepsilon)|^2 + |C_-(K_y, \varepsilon)|^2 \right). \end{aligned} \tag{6.52}$$

By taking the square of Eq. (6.27), splitting the sum into partial sums over even and odd n to guarantee argument smoothness, and using the standard definition of the cyclotron frequency (6.4) to find

$$dn = \frac{\varepsilon}{b_B^2 v_F^2} d\varepsilon = \frac{d\varepsilon}{\hbar \omega_c}, \tag{6.53}$$

the summation over n can be converted into an integral. The result of the summation is :

$$\sum_n \delta(\varepsilon - \varepsilon_n) = \int dn\, \delta(\varepsilon - \varepsilon_n) = \frac{1}{\hbar \omega_c}. \tag{6.54}$$

Since there are no fast oscillations in expression (6.52), the derivative of the Fermi function can be approximated using

$$\frac{df(\varepsilon)}{d\varepsilon} \approx -\delta(\varepsilon - \varepsilon_F), \tag{6.55}$$

maintaining accuracy of the result up to correction of the order of $(k_B T / \varepsilon_F)^2$, which essentially reflects the $T \to 0$ limit, and sets all energy dependences in the expression to $\varepsilon = \varepsilon_F$ after integration over ε. The integral in the second row of Eq. (6.52) is then simply

$$\int_0^{\mathcal{Q}} k_y^+(k_x) dk_x \approx \frac{S_0(\varepsilon_F)}{2}, \tag{6.56}$$

i.e. it gives the size of the Fermi surface which determines the number of carriers per spin projection. The integral in the third row of Eq. (6.52) is easily calculated taking into account the normalisation condition (6.37) and the standard condition in the Landau gauge that the electron wave package centred at x_0 lies within the sample, i.e. $0 < x_0 < L_x$, which determines

$$K_y^m = \frac{1}{\hbar} e B L_x. \tag{6.57}$$

The integral is then:

$$\int_0^{K_y^m} \mathrm{d}K_y(|C_+|^2+|C_-|^2) = 2\omega_c. \tag{6.58}$$

Taking it all together, we finally obtain the result

$$\sigma_{xx} = \frac{m n_0}{\tau_0}\frac{1}{B^2}, \tag{6.59}$$

where m is an effective cyclotron mass and $n_0 = 2S_0(\varepsilon_F)/(2\pi)^2$ is surface concentration of carries (electrons of both spin projections) taken at the Fermi energy. The magnetoconductivity has $\sim B^{-2}$ dependence and it does not contain the MB tunnelling amplitude $t(B)$. It is essentially equal to the classical result for closed orbits.

6.4.2 Diagonal magnetoconductivity σ_{yy}

The diagonal magnetoconductivity along y-direction (along the open trajectories in reciprocal space, see Fig. 6.1 (c), k_x-direction) is determined by the nonvanishing group velocity v_y. Therefore, Eq. (6.38) can be expressed in the form

$$\sigma_{yy} = -\frac{2e^2\tau_0}{L_x L_y}\sum_n \frac{L_y}{2\pi}\int \mathrm{d}K_y v_y^2(K_y,\varepsilon_n(K_y))\left.\frac{\mathrm{d}f(\varepsilon)}{\mathrm{d}\varepsilon}\right|_{\varepsilon_n(K_y)} \tag{6.60}$$

in which we express the velocity in terms of the dispersion law $D(\varepsilon,K_y)$, i.e., by following the method developed by Kaganov and Slutskin in Ref. [91]

$$v_y = \frac{1}{\hbar}\frac{\partial\varepsilon_n(K_y)}{\partial K_y} = -\frac{1}{\hbar}\frac{\frac{\partial D(\varepsilon,K_y)}{\partial K_y}}{\frac{\partial D(\varepsilon,K_y)}{\partial\varepsilon}}. \tag{6.61}$$

Using the same procedure to change the variable $\varepsilon_n \to \varepsilon$ as in the previous subsection as well as well-known decomposition of delta function over zero-points of its argument,

$$\delta(g(x)) = \sum_l \frac{\delta(x-x_l)}{|g'(x_l)|}, \tag{6.62}$$

Eq. (6.60) can be expressed as

$$\sigma_{yy} = -\frac{e^2\tau_0}{\pi\hbar^2 L_x}\int dK_y \int d\varepsilon \frac{df(\varepsilon)}{d\varepsilon}\frac{\left(\left.\frac{\partial D}{\partial K_y}\right|_\varepsilon\right)^2}{\left|\left.\frac{\partial D}{\partial \varepsilon}\right|_{K_y}\right|}\delta(D(\varepsilon,K_y)). \tag{6.63}$$

Taking the partial derivatives in the expression above using Eq. (6.21),

$$\begin{aligned}\left.\frac{\partial D}{\partial K_y}\right|_\varepsilon &= |t|\frac{\hbar^2 Q}{b_B^2}\sin\left(\frac{\hbar^2 Q K_y}{b_B^2}+\mu\right),\\ \left.\frac{\partial D}{\partial \varepsilon}\right|_{K_y} &= -\frac{\pi\varepsilon}{v_F^2 b_B^2}\sin\left(\frac{\pi\varepsilon^2}{2v_F^2 b_B^2}+\theta\right),\end{aligned} \tag{6.64}$$

following a lengthy yet rather straightforward computation, we get

$$\begin{aligned}\sigma_{yy} = &-\frac{e^2\tau_0 Q v_F^2}{\pi^2 L_x}\int_{-\infty}^{\infty} d\varepsilon \frac{df(\varepsilon)}{d\varepsilon}\frac{\sqrt{|t|^2-\cos^2\left(\frac{\pi\varepsilon^2}{2v_F^2 b_B^2}+\theta\right)}}{|\varepsilon|\left|\sin\left(\frac{\pi\varepsilon^2}{2v_F^2 b_B^2}+\theta\right)\right|}\\ &\times\Theta\left[|t|^2-\cos^2\left(\frac{\pi\varepsilon^2}{2v_F^2 b_B^2}+\theta\right)\right],\end{aligned} \tag{6.65}$$

where $\Theta(...)$ is the Heaviside theta function. In the general case (for arbitrary $t(B)$), this magnetoconductivity includes fast quantum oscillations (see Fig. 6.3). The $T=0$ result in the absence of the MB-induced over-gap electron tunnelling ($|t|=1$) reduces to a constant,

$$\sigma_{yy} = \frac{e^2\tau_0 Q v_F^2}{\pi^2\varepsilon_F L_x}, \tag{6.66}$$

independent of magnetic field, which coincides with the classical result along open trajectories as expected. We see that Eq. (6.66) is the same constant in front of the integral in Eq. (6.65) divided by the energy scale from within the integral which reduces to it in the absence of the MB effects. The MB effects in Eq. (6.65) appear not as a correction to the constant term (6.66), but rather as inherent to the main contribution in σ_{yy}. The opposite limiting case of the maximal magnetic breakdown effect ($|t|=0$, $|r|=1$), on the other hand, should be equal to the result (6.59) for closed trajectories, i.e. $\sigma_{yy}=\sigma_{xx}$.

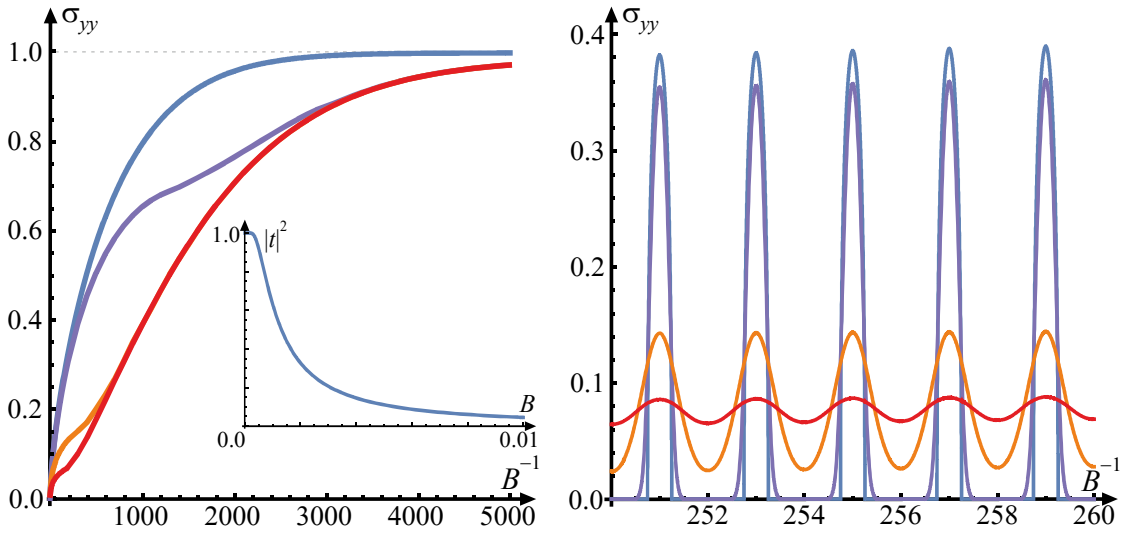

Figure 6.3: Diagonal conductivity σ_{yy} (scaled with $e^2\tau_0 Q v_F^2/\pi^2\varepsilon_F L_x$, see Eq. (6.66)) vs. inverse magnetic field B^{-1} (scaled with $m\varepsilon_F/e\hbar$). Left panel: The upper envelope of fast-oscillating σ_{yy} for different temperatures. The inset shows the MB parameter $|t(B)|^2$ according to Eq. (6.15), where B is scaled to $e\hbar/m\varepsilon_F$. Right panel: Oscillations of σ_{yy} vs. B^{-1} at different temperatures, with period determined by the area of electron trajectory $S_0(\varepsilon_F)$. The temperatures (scaled to k_B/ε_F) in both figures are: 0 (blue), 0.0001 (purple), 0.0005 (orange), 0.001 (red). The gap parameter is everywhere $\Delta/\varepsilon_F = 0.01$. Image from [93].

6.4.3 Hall magnetoconductivity σ_{xy}

As in the case of σ_{xx}, due to the vanishing group velocity v_x, the corresponding contribution must be accounted through the matrix element $\langle\eta|\,\hat{v}_x\,|\eta'\rangle$ which is expressed in terms of the Lorentz force operator proportional to $\hat{\dot{k}}_y$. The expression (6.38) in the case of Hall conductivity reduces to

$$\sigma_{yx} = -\frac{2e}{L_x L_y B}\sum_{\eta}\left(\hbar\langle\eta|\hat{k}_y\hat{v}_y|\eta\rangle - \langle\eta|\hat{k}_y|\eta\rangle\frac{\partial\varepsilon_n(K_y)}{\partial K_y}\right)\frac{\mathrm{d}f(\varepsilon)}{\mathrm{d}\varepsilon}\Big|_{\varepsilon_\eta}, \tag{6.67}$$

where $|\eta\rangle = |n, K_y\rangle$. The two matrix elements, $\langle\eta|\hat{k}_y\hat{v}_y|\eta\rangle$ and $\langle\eta|\hat{k}_y|\eta\rangle$ are evaluated as follows. The first one reads

$$\langle\eta|\,\hat{k}_y\hat{v}_y\,|\eta\rangle = \frac{L_x}{2\pi}\int_0^Q \mathrm{d}k_x\left(\frac{|C_+|^2 k_y^+ v_y^+}{|v_y^+|} + \frac{|C_-|^2 k_y^- v_y^-}{|v_y^-|}\right). \tag{6.68}$$

Since $k_y^- = -k_y^+$ and $|v_y^+| = |v_y^-|$, it reduces to:

$$\begin{aligned}\langle\eta|\,\hat{k}_y\hat{v}_y\,|\eta\rangle =& \frac{L_x}{2\pi}\int_0^Q \mathrm{d}k_x k_y^+ \left(|C_+|^2 + |C_-|^2\right) \\ =& \frac{L_x}{2\pi}\frac{S(\varepsilon(K_y))}{2}\left(|C_+(K_y)|^2 + |C_-(K_y)|^2\right).\end{aligned} \tag{6.69}$$

Similarly, the second term reads:

$$\begin{aligned}\langle\eta|\,\hat{k}_y\,|\eta\rangle =& \frac{L_x}{2\pi}\int_0^Q \mathrm{d}k_x \left(\frac{|C_+|^2 k_y^+}{|v_y^+|} + \frac{|C_-|^2 k_y^-}{|v_y^-|}\right) \\ =& \frac{L_x}{2\pi}\int \mathrm{d}k_x \frac{k_y^+}{v_y^+}\left(|C_+|^2 - |C_-|^2\right).\end{aligned} \tag{6.70}$$

Using $v_y = \hbar\frac{\partial\varepsilon}{\partial k_y} = \frac{v_F^2}{\varepsilon}\hbar k_y$, and $\frac{k_y^+}{v_y^+} = \frac{\varepsilon}{\hbar v_F^2}$, we obtain:

$$\langle\eta|\,\hat{k}_y\,|\eta\rangle = \frac{L_x}{2\pi}\int_0^Q \mathrm{d}k_x \frac{\varepsilon}{\hbar v_F^2}\left(|C_+|^2 - |C_-|^2\right), \tag{6.71}$$

where the negative sign in front of $|C_-|^2$ appears due to $k_y^- = -k_y^+$, finally leading to

$$\langle\eta|\,\hat{k}_y\,|\eta\rangle = \frac{L_x Q}{2\pi}\frac{\varepsilon_n}{\hbar v_F^2}\left(|C_+(K_y)|^2 - |C_-(K_y)|^2\right). \tag{6.72}$$

Similarly to expression (6.37) for $|C_+|^2 + |C_-|^2$, using Eqs. (6.28) and (6.37) one can obtain an expression for $|C_+|^2 - |C_-|^2$, i.e.

$$|C_+|^2 - |C_-|^2 = \frac{2\hbar\omega_c t}{eBL_x}\frac{t - \cos(\phi_1+\phi_2)}{1 - t\cos(\phi_1+\phi_2)}, \tag{6.73}$$

where $\phi_1 = \frac{\pi\varepsilon^2}{2v_F^2 b_B^2} + \theta$ and $\phi_2 = \frac{QK_y\hbar^2}{b_B^2} + \mu$.

Now we can evaluate σ_{yx}. The first term corresponding to (6.69), using (6.58) and inserting (6.54) as well as the $T \to 0$ limit (6.55), evaluates to

$$\sigma_{yx}^{\mathrm{I}} = \frac{2eS_0(\varepsilon_F)}{B(2\pi)^2}. \tag{6.74}$$

The second term corresponding to (6.72) contains

$$-\frac{\partial \varepsilon}{\partial K_y}\langle \eta | k_y | \eta \rangle = \frac{\varepsilon Q}{\hbar v_F^2}\frac{\partial D}{\partial K_y}\left(|C_+|^2 - |C_-|^2\right)\delta(D), \tag{6.75}$$

where D is defined in (6.21). The above expression is a fast oscillating function containing

$$f(\phi_1,\phi_2) = \frac{t-\cos(\phi_1+\phi_2)}{1-t\cos(\phi_1+\phi_2)}\sin\phi_2, \tag{6.76}$$

which is periodic with 2π in ϕ_1 and ϕ_2. We expand (6.76) in a Fourier expansion and keep just the constant term, as the function is fast oscillating, i.e.

$$\bar{f} = \frac{1}{(2\pi)^2}\int_{-\pi}^{\pi} d\phi_1 \int_{-\pi}^{\pi} d\phi_2 \frac{t-\cos\phi_1\cos\phi_2+\sin\phi_1\sin\phi_2}{1-t(\cos\phi_1\cos\phi_2-\sin\phi_1\sin\phi_2)}\frac{\sin\phi_2}{\sqrt{1-t^2\cos{\phi_2}^2}}\delta(\cos\phi_1 - t\cos\phi_2). \tag{6.77}$$

The δ-function inside the integral in (6.77) is evaluated as a sum of δ-functions over all zeroes in the domain of integration. After summing the results for both of the zeroes, $\bar{f}$ turns out to be

$$\bar{f} = 0. \tag{6.78}$$

Therefore, the second contribution in the Hall conductivity evaluates to

$$\sigma_{yx}^{\mathrm{II}} = 0, \tag{6.79}$$

with the fast oscillating part neglected. Summing up the above contributions I and II we finally obtain the Hall magnetoconductivity

$$\sigma_{xy} = -\sigma_{yx} = -\frac{en_0}{B} \tag{6.80}$$

written in terms of the total 2D electron concentration $n_0 = 2S_0(\varepsilon_F)/(2\pi)^2$. This result corresponds to the classical one. In this result, we neglected the fast oscillating *correction*.

6.4.4 Overview

In this chapter, the magnetoconductivity tensor was computed starting from the quantum density matrix, within the semiclassical approximation, using the magnetic breakdown technique. The diagonal magnetoconductivity component along the CDW apex is $\sigma_{xx} \sim B^{-2}$, in accordance to the classical result.

The diagonal component σ_{yy}, perpendicular to the CDW apex is constant in the case of negligible magnetic breakdown. In the case of extremely strong magnetic breakdown σ_{yy} is proportional to $\sim B^{-2}$ in the same way as σ_{xx}. Both regimes correspond to the classical results. In the regime of intermediate magnetic breakdown σ_{yy} develops strong quantum oscillations periodic in inverse magnetic field. Those oscillations are not just a mere correction to the constant classical term, they are an inherent part of it, showing the strong quantum mechanical interference effect of large semiclassical phases.

The Hall conductivity $\sigma_{xy} \sim B^{-1}$ corresponds to the standard classical result neglecting eventual quantum oscillating corrections.

Chapter 7

Thesis summary

Charge density waves are self-consistent modulations of electronic density commonly occurring in tandem with periodic distortion of the crystal lattice of materials. We provided a historical overview from the early mentions of charge density waves in the 1950s, their description through the Peierls instability, to initial experimental discoveries. This gives an insight into how explaining the phenomenon of charge density waves is tightly linked to the concept of Fermi surface nesting to the extent that such an explanation has practically become a paradigm, a successful theory that worked for decades in a significant number of real materials within the class of quasi-one-dimensional systems with a highly anisotropic open Fermi surface.

We presented the basic characteristics of the material this thesis is about, and elaborated how the motivation for this work presented itself. Charge density waves are experimentally observed in materials with Fermi surfaces that have no nesting properties, a class of layered quasi-two-dimensional systems with a rather isotropic closed Fermi surface requiring a new theoretical mechanism.

The aim of this work is to develop a minimal model which explains the phenomenon of charge density wave formation in the intercalated graphite CaC_6. We initially describe the problem of a system of coupled electrons and phonons using a two-dimensional Fröhlich Hamiltonian. We treat it within the mean-field approximation introducing an order parameter proportional to the mean value of the phonon displacement operator describing the lattice deformation. To obtain the shape of topologically reconstructed electronic bands, we employ a specially developed method for expanding subintegral functions to derive an analytical result for the condensation energy of the system, obtaining it self-consistently by optimisation with respect to the wave vector of the CDW ordering and its order parameter. Furthermore, we single out the in-plane TA phonon mode of the of the calcium superlattice as the "softest" one and the most strongly coupled to the carbon electrons, therefore, being responsible for the CDW instability.

This theoretical work is inspired by experimental observations which we compared with our results. The theoretical explanations presented show an exceptionally good agreement with key experimentally observed facts: (1) the occurrence, period, and orientation of the charge density wave with respect to the graphene lattice; (2) the appearance of a pseudo-gap in the electronic spectrum; (3) the static deformation of the calcium superlattice corresponding to the theoretically predicted phonon TA mode. The onset of the CDW in the intercalated graphite CaC_6 appears as a quantum phase transition due to the topological reconstruction of the Fermi surface of electrons coupled to aforementioned phonon modes if the coupling is stronger than critical.

Furthermore, we calculated the tensor of magnetoconductivity for the intercalated graphite CaC_6 in the CDW ground state, under conditions of magnetic breakdown within the semiclassical approximation which provided the electronic spectrum and wave functions. We provided a description of the phenomenon of coherent magnetic breakdown appearing in a strong external magnetic field B in the regime in which the characteristic Larmor radius is much smaller than the mean free path due to impunity scattering. The consideration is developed for low enough temperatures so that other relaxation channels can be neglected. The tensor of magnetoconductivity for a two-dimensional system is calculated within the formalism of the quantum density matrix. Due to the uniaxial CDW, this tensor is anisotropic and contains a component along the CDW crests, which is perpendicular to the open electronic trajectories in reciprocal space, a component along the direction of the periodicity of the CDW, which is along the open electronic trajectories in reciprocal space, and the Hall components of magnetoconductivity. The diagonal magnetoconductivity component along the CDW apex is $\sigma_{xx} \sim B^{-2}$, in accordance to the classical result. The diagonal component σ_{yy}, perpendicular to the CDW apex is constant in the case of negligible magnetic breakdown. In the case of extremely strong magnetic breakdown σ_{yy} is proportional to $\sim B^{-2}$ in the same way as σ_{xx}. Both regimes correspond to the classical results. In the regime of intermediate magnetic breakdown σ_{yy} develops strong quantum oscillations periodic in inverse magnetic field. Those oscillations are not just a mere correction to the constant classical term, they are an inherent part of it, showing the strong quantum mechanical interference effect of large semiclassical phases. The Hall conductivity $\sigma_{xy} \sim B^{-1}$ corresponds to the standard classical result neglecting eventual quantum oscillating corrections.

The significance of the research presented in this dissertation, within the field of charge orderings in materials, is multiple. Real materials, whose charge orderings were explained by the nesting mechanism, are mainly chain-like organic conductors (Bechgaard salts, Fabre salts, blue bronzes, etc.), which, besides their great importance for fundamental physics, generally had no technological significance due to small available quantities, difficult synthesis, poor mechanical

properties, and low critical temperatures (of the order of 1 - 10 K) of charge and superconducting phases due to very weak interactions responsible for them. Later, a new class of materials was discovered in which charge arrangements occur, so-called quasi two-dimensional systems with rather isotropic properties in the crystal planes and low dispersion perpendicular to them. Examples of such materials include high-temperature superconducting cuprates, intercalated graphite compounds, transition metal dichalcogenides, and so on. Besides being important for fundamental physics, they are also characterized by important technological properties. Charge orderings coexist in phase diagrams with high-temperature superconductivity for which we still lack a theoretical explanation, and understanding them might crucially depend on understanding the mechanisms of charge orderings which appear to be incompatible with the nesting paradigm. Recently, within our research group, a mechanism based on a quantum phase transition to a more stable state of charge ordering has been proposed, which occurs through topological reconstruction of the Fermi surface of the electronic condensate if the coupling to the phonon subsystem of the crystal lattice exceeds a critical value (A. M. Kadigrobov, A. Bjeliš and D. Radić, Phys. Rev. B **97**, 235439 (2018)). In that publication, the mechanism was presented very generally, as a fundamental mechanism without any specificities related to a particular material. The research presented in this work and published in the paper P. Grozić, B. Keran, A. M. Kadigrobov and D. Radić, "Charge stripes in the graphene-based materials," Scientific Reports **13**, 18931 (2023), for the first time implemented the proposed mechanism, taking into account all the specificities of the system, calcium-intercalated graphite CaC_6. As mentioned, charge orderings share the phase diagram with the superconducting (and high-temperature superconducting) phase, the pseudo-gap phase, and in some cases, the antiferromagnetic phase, so their understanding, to which the results presented in this dissertation significantly contribute, can notably improve the understanding of the phase diagram of these materials, many of which also having important technological applications.

Supervisor information

Danko Radić holds the position of associate professor at the Department of Physics, University of Zagreb Faculty of Science. He published more than 40 scientific papers indexed in WoSCC/Scopus, within the field of theoretical condensed matter physics, cited more than 300 times according to Google Scholar. The main research fields of his interest are: (1) systems of anomalous dimensionality (quasi-1D, quasi-2D) with ground states of broken symmetry such as charge or spin density wave with and without external magnetic field; (2) nonlinear nanoelectromechanical systems with emphasised role of nanomechanics in magnetomotive instabilities as well as superconducting nanomechanical Josephson junctions used for quantum information processing. He defended his doctoral thesis in 2006 after which he spent three years as a postdoc at the University of Gothenburg and Calmers University of Technology, Göteborg, Sweden. He maintains a constant scienfic collaboration with the Institute for Basic Science, Daejeon, Republic of Korea. He worked as a PI and an associate on more than 10 national and international research projects, supervised more than 10 diploma theses and currently supervises 2 PhD students. He teaches the courses in condensed matter and nonlinear physics at the master and doctoral studies of physics at the University of Zagreb Faculty of Science. The institutional duty he currently holds is the head of the Condensed matter division at the Department of Physics, University of Zagreb Faculty of Science.

Curriculum vitae

Petra Grozić was born in 1993 in Milan, Italy, where she spent the first six years of her life. She completed elementary school in Samobor and high school in Zagreb. During her high school education, she also attended a music school where she studied singing. She graduated with a degree in physics education from the Department of Physics, Faculty of Science, University of Zagreb in 2018. Under the mentorship of Associate Professor Dr. Danko Radić, she worked on the thesis titled "Pseudomagnetic Fields in Graphene." Throughout her studies, she engaged in science popularisation activities by participating in the University Fair in Zagreb, volunteering at the event "Day and Night at the Faculty of Science," and conducting workshops at the same event. Since April 2019, she has been working as a teaching assistant at the Department of Physics, Faculty of Science, University of Zagreb, while pursuing a doctoral degree in theoretical condensed matter physics. She enhances her teaching skills by conducting exercises for courses such as Statistical Physics, Selected Topics in Solid State Physics, and Laboratory Practice in Experimental Physics.

Petra's scientific interest is focused on the study of quasi-two-dimensional systems where the phenomenon of charge density wave (CDW) is observed, as well as the investigation of the conductivity and magnetoresistance of such systems under magnetic breakthrough conditions. She has published two scientific articles in international peer-reviewed journals listed in the ISI Web of Science (one as the main author). Particularly noteworthy is her work in the journal Nature Scientific Reports ("Charge stripes in the graphene-based materials," Scientific Reports 13, 18931, (2023)), where she is the lead author.

She has participated in a total of nine international scientific conferences, where she delivered three oral presentations and presented three posters. She also gave an invited lecture-workshop at a professional conference for physics teachers on the topic "The Role of Sources in Electrical Circuits."

She actively contributes to the popularisation of physics and science in general through volunteering and conducting lectures and workshops such as "The Purpose of Physics Today" (Technical Museum in Zagreb, 2023) and "Discoveries That Changed the World" (Day and

Night at the Faculty of Science, 2023). Additionally, she is involved in organising the event "Day and Night at the Faculty of Science" for the year 2024. Besides her scientific pursuits, Petra competes in weightlifting and has won numerous medals in national competitions, currently holding a bronze medal in the category for women up to 59 kilogrammes.

References

[1] D. E. Laughlin and K. Hono. *Physical Metallurgy*. Newnes, 2014.

[2] R. E. Peierls. *Quantum theory of solids*. Oxford University Press, 1955.

[3] H. Fröhlich. On the theory of superconductivity: the one-dimensional case. *Proceedings of the Royal Society of London. Series A. Mathematical and Physical Sciences*, 223 (1154):296–305, 1954.

[4] G. Gruner. *Density waves in solids*. CRC press, 2018.

[5] G. Grüner. The dynamics of charge-density waves. *Reviews of Modern Physics*, 60(4): 1129, 1988.

[6] J. T. Devreese, R. P. Evrard, and V.E. Doren. Highly conducting one-dimensional solids.

[7] W. Fogle and J. H. Perlstein. Semiconductor-to-metal transition in the blue potassium molybdenum bronze, $K_{0.30}$ MoO_3; example of a possible excitonic insulator. *Physical Review B*, 6(4):1402, 1972.

[8] P. Monceau, N.P. Ong, A. Portis, A. Meerschaut, and J. Rouxel. Electric field breakdown of charge-density-wave-induced anomalies in Nb Se_3. *Physical Review Letters*, 37(10): 602, 1976.

[9] M.J. Rice and S. Strässler. Theory of the soft phonon mode and dielectric constant below the Peierls transition temperature. *Solid State Communications*, 13(12):1931–1933, 1973.

[10] C.G. Kuper. On the thermal properties of Fröhlich's one-dimensional superconductor. *Proceedings of the Royal Society of London. Series A, Mathematical and Physical Sciences*, pages 214–228, 1955.

[11] J. Sólyom. The Fermi gas model of one-dimensional conductors. *Advances in Physics*, 28(2):201–303, 1979.

[12] W.A. Little. Possibility of synthesizing an organic superconductor. *Physical Review*, 134 (6A):A1416, 1964.

[13] J. M. Ziman. *Principles of the Theory of Solids*. Cambridge University Press, 1972.

[14] K. S. Novoselov, A. K. Geim, S. V. Morozov, D. Jiang, Y. Zhang, S. V. Dubonos, I. V. Grigorieva, and A. A. Firsov. Electric field effect in atomically thin carbon films. *Science*, 306(5696):666–669, 2004.

[15] C. Lee, X. Wei, J. W. Kysar, and J. Hone. Measurement of the elastic properties and intrinsic strength of monolayer graphene. *Science*, 321(5887):385–388, 2008.

[16] A. A. Balandin, S. Ghosh, W. Bao, I. Calizo, D. Teweldebrhan, F. Miao, and C. N. Lau. Superior thermal conductivity of single-layer graphene. *Nano Letters*, 8(3):902–907, 2008.

[17] V. Berry. Impermeability of graphene and its applications. *Carbon*, 62:1–10, 2013.

[18] G. Yang, L. Li, W. B. Lee, and M. C. Ng. Structure of graphene and its disorders: a review. *Science and Technology of Advanced Materials*, 19(1):613–648, 2018.

[19] E. McCann. Electronic properties of monolayer and bilayer graphene. In *Graphene Nanoelectronics: Metrology, Synthesis, Properties and Applications*, pages 237–275. Springer, 2012.

[20] P. R. Wallace. The band theory of graphite. *Physical Review*, 71(9):622, 1947.

[21] S. Reich, J. Maultzsch, C. Thomsen, and P. Ordejon. Tight-binding description of graphene. *Physical Review B*, 66(3):035412, 2002.

[22] G. Dresselhaus, M. S. Dresselhaus, and R. Saito. *Physical properties of carbon nanotubes*. World scientific, 1998.

[23] J.C. Slonczewski and P.R. Weiss. Band structure of graphite. *Physical Review*, 109(2): 272, 1958.

[24] G. W. Semenoff. Condensed-matter simulation of a three-dimensional anomaly. *Physical Review Letters*, 53(26):2449, 1984.

[25] F. Haldane and M. Duncan. Model for a quantum Hall effect without landau levels: Condensed-matter realization of the" parity anomaly". *Physical Review Letters*, 61(18): 2015, 1988.

[26] K. F. Mak, C. H. Lui, J. Shan, and T. F. Heinz. Observation of an electric-field-induced band gap in bilayer graphene by infrared spectroscopy. *Physical Review Letters*, 102(25): 256405, 2009.

[27] K. Tang, R. Qin, J. Zhou, H. Qu, J. Zheng, R. Fei, H. Li, Q. Zheng, Z. Gao, and J. Lu. Electric-field-induced energy gap in few-layer graphene. *The Journal of Physical Chemistry C*, 115(19):9458–9464, 2011.

[28] S. D. Dalosto and Z. H. Levine. Controlling the band gap in zigzag graphene nanoribbons

with an electric field induced by a polar molecule. *The Journal of Physical Chemistry C*, 112(22):8196–8199, 2008.

[29] H. Yuan, S. Chang, I. Bargatin, N. C. Wang, D. C. Riley, H. Wang, J. W. Schwede, J. Provine, E. Pop, Z. Shen, et al. Engineering ultra-low work function of graphene. *Nano Letters*, 15(10):6475–6480, 2015.

[30] M. Gmitra, Se. Konschuh, Christian Ertler, C. Ambrosch-Draxl, and J. Fabian. Band-structure topologies of graphene: Spin-orbit coupling effects from first principles. *Physical Review B*, 80(23):235431, 2009.

[31] Y. Y. Wang, Z. H. Ni, T. Yu, Z. X. Shen, H. M. Wang, Y. H. Wu, W. Chen, and Andrew T. Shen W. Raman studies of monolayer graphene: the substrate effect. *The Journal of Physical Chemistry C*, 112(29):10637–10640, 2008.

[32] Q. H. Wang, Z. Jin, K. K. Kim, A. J. Hilmer, G. L.C. Paulus, C. Shih, M. Ham, J. D. Sanchez-Yamagishi, K. Watanabe, T. Taniguchi, et al. Understanding and controlling the substrate effect on graphene electron-transfer chemistry via reactivity imprint lithography. *Nature Chemistry*, 4(9):724–732, 2012.

[33] G. Gui, J. Li, and J. Zhong. Band structure engineering of graphene by strain: First-principles calculations. *Physical Review B*, 78(7):075435, 2008.

[34] C. Si, Z. Sun, and F. Liu. Strain engineering of graphene: a review. *Nanoscale*, 8(6): 3207–3217, 2016.

[35] K. S. Novoselov, D. Jiang, F. Schedin, T.J. Booth, V.V. Khotkevich, S. V. Morozov, and A. K. Geim. Two-dimensional atomic crystals. *Proceedings of the National Academy of Sciences*, 102(30):10451–10453, 2005.

[36] L. Liang, J. Wang, W. Lin, B. G. Sumpter, V. Meunier, and M. Pan. Electronic bandgap and edge reconstruction in phosphorene materials. *Nano Letters*, 14(11):6400–6406, 2014.

[37] N. Kumar, R. Salehiyan, V. Chauke, O. J. Botlhoko, K. Setshedi, M. Scriba, M. Masukume, and S. S. Ray. Top-down synthesis of graphene: A comprehensive review. *FlatChem*, 27:100224, 2021.

[38] Q. Abbas, P. A. Shinde, M. A. Abdelkareem, A. H. Alami, M. Mirzaeian, A. Yadav, and A. G. Olabi. Graphene synthesis techniques and environmental applications. *Materials*, 15(21):7804, 2022.

[39] K. A. Madurani, S. Suprapto, N. Machrita, S. L. Bahar, W. Illiya, and F. Kurniawan. Progress in graphene synthesis and its application: history, challenge and the future out-

look for research and industry. *ECS Journal of Solid State Science and Technology*, 9(9): 093013, 2020.

[40] X. Cai, Z. Jiang, X. Zhang, and X. Zhang. Effects of tip sonication parameters on liquid phase exfoliation of graphite into graphene nanoplatelets. *Nanoscale Research Letters*, 13:1–10, 2018.

[41] J. Shah, J. Lopez-Mercado, M. G. Carreon, A. Lopez-Miranda, and M. L. Carreon. Plasma synthesis of graphene from mango peel. *ACS Omega*, 3(1):455–463, 2018.

[42] J. R. Prekodravac, D. P. Kepić, J. C. Colmenares, D. A. Giannakoudakis, and S. P. Jovanović. A comprehensive review on selected graphene synthesis methods: From electrochemical exfoliation through rapid thermal annealing towards biomass pyrolysis. *Journal of Materials Chemistry C*, 9(21):6722–6748, 2021.

[43] R. Torres-Mendieta, D. Ventura-Espinosa, S. Sabater, J. Lancis, G. Mínguez-Vega, and J. A. Mata. In situ decoration of graphene sheets with gold nanoparticles synthetized by pulsed laser ablation in liquids. *Scientific reports*, 6(1):30478, 2016.

[44] G. Moreno-Fernández, N. Boulanger, A. Nordenström, A. Iakunkov, A. Talyzin, D. Carriazo, and R. Mysyk. Ball-milling-enhanced capacitive charge storage of activated graphene in aqueous, organic and ionic liquid electrolytes. *Electrochimica Acta*, 370: 137738, 2021.

[45] M. K. Rabchinskii, S. A. Ryzhkov, D. A. Kirilenko, N. V. Ulin, M. V. Baidakova, V. V. Shnitov, S. I. Pavlov, R. G. Chumakov, D. Y. Stolyarova, N. A. Besedina, et al. From graphene oxide towards aminated graphene: Facile synthesis, its structure and electronic properties. *Scientific reports*, 10(1):6902, 2020.

[46] K. Yoon and G. Dong. Liquid-phase bottom-up synthesis of graphene nanoribbons. *Materials Chemistry Frontiers*, 4(1):29–45, 2020.

[47] L. Sun, G. Yuan, L. Gao, J. Yang, M. Chhowalla, M. H. Gharahcheshmeh, K. K. Gleason, Y. S. Choi, B. H. Hong, and Z. Liu. Chemical vapour deposition. *Nature Reviews Methods Primers*, 1(1):5, 2021.

[48] W. Shang, T. Cai, Y. Zhang, D. Liu, and S. Liu. Facile one pot pyrolysis synthesis of carbon quantum dots and graphene oxide nanomaterials: All carbon hybrids as eco-environmental lubricants for low friction and remarkable wear-resistance. *Tribology International*, 118:373–380, 2018.

[49] Z. Gao, S. Wang, J. Berry, Q. Zhang, J. Gebhardt, W. M. Parkin, J. Avila, H. Yi, C. Chen, S. Hurtado-Parra, et al. Large-area epitaxial growth of curvature-stabilized ABC trilayer graphene. *Nature Communications*, 11(1):546, 2020.

[50] N. Emery, C. Hérold, J.-F. Marêché, and P. Lagrange. Synthesis and superconducting properties of CaC_6. *Science and Technology of Advanced Materials*, 2009.

[51] D. Guérard, M. Chaabouni, P. Lagrange, M. El Makrini, and A. Hérold. Insertion of alkaline earth metals into graphite. *Carbon*, 18(4):257–264, 1980.

[52] C. Pruvost, S.and Hérold, A. Hérold, and P. Lagrange. Structural study of novel graphite-lithium- calcium intercalation compounds. *European Journal of Inorganic Chemistry*, 2004(8):1661–1667, 2004.

[53] N. Emery, S. Pruvost, C. Hérold, and P. Lagrange. New kinetical and thermodynamical data concerning the intercalation of lithium and calcium into graphite. *Journal of Physics and Chemistry of Solids*, 67(5-6):1137–1140, 2006.

[54] N. Emery, C. Hérold, and P. Lagrange. Structural study and crystal chemistry of the first stage calcium graphite intercalation compound. *Journal of Solid State Chemistry*, 178 (9):2947–2952, 2005.

[55] S. Pruvost, P. Berger, C. Hérold, and P. Lagrange. Nuclear microanalysis: An efficient tool to study intercalation compounds containing lithium. *Carbon*, 42(10):2049–2056, 2004.

[56] P. Berger, S. Pruvost, C. Hérold, and P. Lagrange. Proton enhanced scattering and nuclear reaction analysis microcharacterization of ternary graphite–lithium–calcium intercalation compounds. *Nuclear Instruments and Methods in Physics Research Section B: Beam Interactions with Materials and Atoms*, 219:1005–1009, 2004.

[57] K.C. Rahnejat, C.A. Howard, N.E. Shuttleworth, S.R. Schofield, K. Iwaya, C.F. Hirjibehedin, Ch. Renner, G. Aeppli, and M. Ellerby. Charge density waves in the graphene sheets of the superconductor CaC_6. *Nature Communications*, 2(1):558, 2011.

[58] R. Shimizu, K. Sugawara, K. Kanetani, K. Iwaya, T. Sato, T. Takahashi, and T. Hitosugi. Charge-density wave in Ca-intercalated bilayer graphene induced by commensurate lattice matching. *Physical Review Letters*, 114(14):146103, 2015.

[59] I.I. Mazin and A.V. Balatsky. Superconductivity in Ca-intercalated bilayer graphene. *Philosophical Magazine Letters*, 90(10):731–738, 2010.

[60] R.A. Jishi, D.M. Guzman, and H.M. Alyahyaei. Theoretical investigation of two-dimensional superconductivity in intercalated graphene layers. *arXiv preprint arXiv:1107.1845*, 2011.

[61] Yuanbo Zhang, Victor W Brar, Feng Wang, Caglar Girit, Yossi Yayon, Melissa Panlasigui, Alex Zettl, and Michael F Crommie. Giant phonon-induced conductance in

scanning tunnelling spectroscopy of gate-tunable graphene. *Nature Physics*, 4(8):627–630, 2008.

[62] M-H Whangbo, W Liang, J Ren, SN Magonov, and A Wawkuschewski. Structural and electronic properties of graphite and graphite intercalation compounds mc8 (m= k, rb, cs) governing their scanning tunneling microscopy images. *The Journal of Physical Chemistry*, 98(31):7602–7607, 1994.

[63] Dario Anselmetti, V Geiser, G Overney, R Wiesendanger, and H-J Güntherodt. Local symmetry breaking in stage-1 alkali-metal–graphite intercalation compounds studied by scanning tunneling microscopy. *Physical Review B*, 42(3):1848, 1990.

[64] T. Valla, J. Camacho, Z.-H. Pan, A.V. Fedorov, A.C. Walters, C.A. Howard, and M. Ellerby. Anisotropic electron-phonon coupling and dynamical nesting on the graphene sheets in superconducting CaC_6 using angle-resolved photoemission spectroscopy. *Physical Review Letters*, 102(10):107007, 2009.

[65] H. Fröhlich, H. Pelzer, and S. Zienau. XX. properties of slow electrons in polar materials. *The London, Edinburgh, and Dublin Philosophical Magazine and Journal of Science*, 41 (314):221–242, 1950.

[66] H. Fröhlich. Electrons in lattice fields. *Advances in Physics*, 3(11):325–361, 1954.

[67] P. Grozić, B. Keran, A. M. Kadigrobov, and D. Radić. Charge stripes in the graphene-based materials. *Scientific Reports*, 13(1):18931, 2023.

[68] J. Sólyom. *Fundamentals of the Physics of Solids: Volume 3-Normal, Broken-Symmetry, and Correlated Systems*, volume 3. Springer Science & Business Media, 2010.

[69] H. Fröhlich. Superconductivity and the many body problem. *Perspectives in Modern Physics*, page 539, 1966.

[70] T.K. Mitra. The rigid-ion method in the wannier representation. *Journal of Physics C: Solid State Physics*, 2(7):1357, 1969.

[71] S. Barišić. Rigid-atom electron-phonon coupling in the tight-binding approximation. i. *Physical Review B*, 5(3):932, 1972.

[72] R.A. Deegan. Electron-phonon interaction in the tight-binding approximation: Validity of the bloch formulation. *Physical Review B*, 5(3):1183, 1972.

[73] J. P. Pouget. Structural instabilities. In *Semiconductors and Semimetals*, volume 27, pages 87–214. Elsevier, 1988.

[74] J.-P. Pouget. Structural aspects of the bechgaard and fabre salts: An update. *Crystals*, 2 (2):466–520, 2012.

[75] R. E. Thorne. Charge-density-wave conductors. *Physics Today*, 49(5):42–47, 1996.

[76] I.I. Mazin. Intercalant-driven superconductivity in YbC_6 and CaC_6. *Physical Review Letters*, 95(22):227001, 2005.

[77] M. Calandra and F. Mauri. Theoretical explanation of superconductivity in C_6Ca. *Physical Review Letters*, 95(23):237002, 2005.

[78] M. Calandra and F. Mauri. Electronic structure of heavily doped graphene: The role of foreign atom states. *Physical Review B*, 76(16):161406, 2007.

[79] G. Profeta, M. Calandra, and F. Mauri. Phonon-mediated superconductivity in graphene by lithium deposition. *Nature Physics*, 8(2):131–134, 2012.

[80] A.V. Fedorov, N.I. Verbitskiy, D. Haberer, C. Struzzi, L. Petaccia, D. Usachov, O.Y. Vilkov, D.V. Vyalikh, J. Fink, M. Knupfer, et al. Observation of a universal donor-dependent vibrational mode in graphene. *Nature Communications*, 5(1):3257, 2014.

[81] E.R. Margine, H. Lambert, and F. Giustino. Electron-phonon interaction and pairing mechanism in superconducting Ca-intercalated bilayer graphene. *Scientific Reports*, 6 (1):21414, 2016.

[82] D. Novko. Dopant-induced plasmon decay in graphene. *Nano Letters*, 17(11):6991–6996, 2017.

[83] E. Fradkin and S. A. Kivelson. Ineluctable complexity. *Nature Physics*, 8(12):864–866, 2012.

[84] M. Eremin, I. Eremin, G. Seibold, and S. Varlamov. Influence of incommensurability on SDW and CDW amplitudes in underdoped cuprates. *Physica C: Superconductivity*, 341: 937–938, 2000.

[85] H. Miao, R. Fumagalli, M. Rossi, J. Lorenzana, G. Seibold, F. Yakhou-Harris, K. Kummer, N. B. Brookes, G.D. Gu, L. Braicovich, et al. Formation of incommensurate charge density waves in cuprates. *Physical Review X*, 9(3):031042, 2019.

[86] S.n Lee, E. W. Huang, T. A. Johnson, X. Guo, A. A. Husain, M. Mitrano, K. Lu, A. V. Zakrzewski, G. A. de la Peña, Y. Peng, et al. Generic character of charge and spin density waves in superconducting cuprates. *Proceedings of the National Academy of Sciences*, 119(15):e2119429119, 2022.

[87] Y. I. Joe, X.M. Chen, P. Ghaemi, K.D. Finkelstein, G.A. de La Peña, J.C.T. Gan, Y .and Lee, S. Yuan, J. Geck, G.J. MacDougall, et al. Emergence of charge density wave domain walls above the superconducting dome in 1 T-$TiSe_2$. *Nature Physics*, 10(6): 421–425, 2014.

[88] A. Kogar, G. A. de La Pena, S. Lee, Y. Fang, S.X.-L. Sun, D. B. Lioi, G. Karapetrov, K. D. Finkelstein, J. P.C. Ruff, P. Abbamonte, et al. Observation of a charge density

wave incommensuration near the superconducting dome in Cu_xTiSe_2. *Physical Review Letters*, 118(2):027002, 2017.

[89] S. Yan, D. Iaia, E. Morosan, E. Fradkin, P. Abbamonte, and V. Madhavan. Influence of domain walls in the incommensurate charge density wave state of Cu intercalated 1 T-$TiSe_2$. *Physical Review Letters*, 118(10):106405, 2017.

[90] I. M. Lifshits, M. J. Azbel, and M. I. Kaganov. *Electron theory of metals*, volume 1. Springer, 1973.

[91] M. I. Kaganov and A.A. Slutskin. Coherent magnetic breakdown. *Physics Reports*, 98 (4):189–271, 1983.

[92] L. D. Landau and E. M. Lifshitz. *Quantum mechanics: non-relativistic theory*, volume 3. Elsevier, 2013.

[93] P. Grozić, A.K. Kadigrobov, Z. Rukelj, I. Kupčić, and D. Radić. Magneotoconductivity of intercalated graphite CaC_6 with the Fermi surface reconstructed by the uniaxial charge density wave-maruscript in preparation.

[94] L. Onsager. Interpretation of the de Haas-van Alphen effect. *The London, Edinburgh, and Dublin Philosophical Magazine and Journal of Science*, 43(344):1006–1008, 1952.

[95] I.M. Lifshitz and Am. M. Kosevich. Theory of magnetic susceptibility in metals at low temperature. *Zh. eksp. teor. Fiz*, 29:730–742, 1955.

[96] L.M. Falicov and H. Stachowiak. Theory of the de Haas-van Alphen effect in a system of coupled orbits. application to magnesium. *Physical Review*, 147(2):505, 1966.

[97] A.M. Kadigrobov, A. Bjeliš, and D. Radić. Peierls-type structural phase transition in a crystal induced by magnetic breakdown. *The European Physical Journal B*, 86:1–11, 2013.

[98] A.M. Kadigrobov, D. Radić, and A. Bjeliš. Magnetic breakdown in an array of overlapping fermi surfaces. *Physica B: Condensed Matter*, 460:248–252, 2015.

[99] A.M. Kadigrobov, A.A. Slutskin, and S.A. Vorontsov. Interband tunneling of the electrons near the phase transition of the 212 order. *Journal of Physics and Chemistry of Solids*, 53(3):387–393, 1992.

[100] J.-Y. Fortin and A. Audouard. Transmission and tunneling probability in two-band metals: influence of magnetic breakdown on the Onsager phase of quantum oscillations. *Low Temperature Physics*, 43(2):173–185, 2017.

[101] E.I. Blount. Bloch electrons in a magnetic field. *Physical Review*, 126(5):1636, 1962.

[102] G.P. Mikitik and Y. V. Sharlai. The berry phase in graphene and graphite multilayers. *Low Temperature Physics*, 34(10):794–800, 2008.

[103] A.M. Kadigrobov, B. Keran, and D. Radić. Magnetoconductivity of a metal with a closed fermi surface reconstructed by a biaxial density wave. *Physical Review B*, 104 (15):155143, 2021.

[104] M. I. Kaganov and V. G. Peschansky. Galvano-magnetic phenomena today and forty years ago. *Physics Reports*, 372(6):445–487, 2002.

“I dijete!”